VILNIUS UNIVERSITY
CENTRE FOR PHYSICAL SCIENCES AND TECHNOLOGY

KAROLIS GULBINAS

PHOTOELECTRICAL AND OPTICAL PROPERTIES OF INDIRECT BANDGAP SEMICONDUCTORS $TlGaSe_2$ AND SiC

Doctoral dissertation
Technological Sciences, Materials Science (08T)

Vilnius, 2015

The dissertation was prepared at the Institute of Applied Research, Vilnius University in 2010-2014.

Scientific supervisor:
Dr. Vytautas Grivickas (Vilnius University, Technological Sciences, Materials Science – 08T).

VILNIAUS UNIVERSITETAS
FIZINIŲ IR TECHNOLOGIJOS MOKSLŲ CENTRAS

KAROLIS GULBINAS

NETIESIATARPIŲ PUSLAIDININKIŲ $TlGaSe_2$ IR SiC FOTOELEKTRINIŲ IR OPTINIŲ SAVYBIŲ TYRIMAS

Daktaro disertacija
Technologijos mokslai, medžiagų inžinerija (08T)

Vilnius, 2015

Disertacija rengta Vilniaus universitete Taikomųjų mokslų institute 2010 – 2014 metais.

Mokslinis vadovas – dr. Vytautas Grivickas (Vilniaus universitetas, technologijos mokslai, medžiagų inžinerija 08T).

Reziumė

Naujų medžiagų poreikis elektronikai ir optoelektronikai nuolatos auga, nes jos atveria naujas taikymo galimybes ir padeda spręsti technines problemas Dviejų dimensijų sluoksniuotas $TlGaSe_2$ ir SiC politipai 6H, 4H ir 3C yra sintetinės plačiatarpių puslaidininkių medžiagos, pasižyminčios ilga krūvininkų gyvavimo trukme, stipria elektron-fononine sąveika ir santykinai maža liuminescencija. $TlGaSe_2$ yra gerai žinomas kaip izoliuojantis sluoksniuotas fotolaidininkas, kuris žemų temperatūrų srityje turi fazinius virsmus. Jo savybės, atkaitinant žemoje temperatūroje, jautriai priklauso nuo vidinio elektrinio lauko, sužadinimo ir išorinės aplinkos. 3C- 4C- ir 6H-SiC politipų sluoksniai yra auginami komerciškai bei naudojami aukštų temperatūrų ir didelės galios optoelektronikoje. Kiekvienas politipas pasižymi specifiniais privalumais bei problemomis.

Šiame darbe buvo siekta kompleksiniais būdais (technologijomis ar specialiomis eksperimento sąlygomis) išgauti naujų žinių apie dominuojančius krūvininkų generacijos, pernašos ir rekombinacijos mechanizmus bei atrasti kelius, kuriais būtų galima tobulinti ir modifikuoti minėtas medžiagas įvairiems pritaikymams.

Buvo atrastas naujas būdas kaip ištirti $TlGaSe_2$ optinio krašto sugertį, panaudojant fotoakustinį reiškinį. Gretinant šį metodą su laisvųjų krūvininkų pasiskirstymu į gylį buvo ištirtas sugerties kraštas $TlGaSe_2$ sluoksnio augimo ašies ir taip pat sluoksnio plokštumos atžvilgiu. Buvo eksperimentiškai aptikti optinės anizotropijos reiškiniai, susiję su struktūrinėmis fazėmis. Buvo išnagrinėta krūvininkų difuzijos šuolių tarp sluoksnių įtaka krūvininkų gyvavimo trukmei ir nustatyti didelių elektronų gaudyklių parametrai. Pirmą kartą $TlGaSe_2$ buvo aptikta tarpjuostinė fotoliuminescencija kambario temperatūroje ir nustatytos jos spindulinio aktyvumo priežastys. Nustatytas PL ryšys su silpno osciliatoriaus Γ tiesiatarpiu poliarizuotu eksitonu. Ištirtas priemaišinių Fe sugerties juostų atsiradimas, bei jų poveikis nuosavos sugerties optiniam kraštui.

Išnagrinėti optiniai ir rekombinaciniai procesai aukštos kokybės 6H-SiC, kuris stipriai legiruojamas N-donorais ir B-akceptoriais bei pasižymi 7 % fluorescencine ištrūka kambario temperatūroje. Nustatytas labai mažas nepagrindinių krūvininkų difuzijos koeficientas ir silpna paviršinė rekombinacija esant vidutiniam bei mažam sužadinimui. Milisekundinės krūvininkų gyvavimo trukmės šioje medžiagoje yra įtakojamos dviejų tipų boro atomų prilipimo lygmenų. Nustatyta, kad liuminescencijos spektras yra sudarytas iš persiklojančių plačių komponenčių. Viena jų yra sąlygota optinių šuolių tarp donor-akceptorinių lygmenų, kita – tarp laidumo juostos į akceptorinį lygmenį.

Ištirti skirtingais oksidais pasyvuoti ploni 4H-SiC sluoksniai lauko tranzistorių taikymams. Nustatyta, kad Al_2O_3 pasyvavimas labiau sumažina paviršinę rekombinaciją ir yra atsparesnis radiacinėje aplinkoje, nei įprastas SiO_2 pasyvavimas.

Ištirta nusluoksniuoto 3C-SiC epitaksinio sluoksnio, užauginto ant banguoto Si padėklo, liekamųjų įtempimų įtaka krūvininkų gyvavimo trukmei ir bandinio sugerties krašto kokybei.

Acknowledgements

First of all, I would like to thank my scientific supervisor dr. Vytautas Grivickas for leading through the PhD studies, endless energy and care.

My special thanks goes to prof. Jan Linnros for hosting my internships at Royal Institute of Technology and absolute freedom in the lab.

Separately, I would like to thank co-authors of my publications for collaboration and team work during the research and publication preparation process.

Finally, I would like to thank my family for tolerance and support.

This work has been supported in part by Lithuanian State Study Foundation, the Research Council of Lithuania and Swedish Institute scholarship.

Table of Contents

List of abbreviations **10**

Introduction **11**

1. Overview of $TlGaSe_2$ and SiC properties **20**

1.1. Properties of $TlGaSe_2$ layered semiconductor 20

1.2. Properties of SiC 28

1.2.1. Fluorescent 6H-SiC application 31

1.2.2. 4H-SiC 33

1.2.3. 3C-SiC 35

2. Carrier dynamics and optical techniques **37**

2.1. Free carrier absorption (FCA) 37

2.2. Carrier lifetime 39

2.3. Absorption processes 42

2.4. Photoacoustic wave (PA) generation by laser pulse 44

2.4.1. General mechanisms 45

2.4.2. PAR generation at unconstrained free surfaces 45

2.4.3. Stress confinement, deformation and thermoelastic mechanisms 46

2.4.4. Acoustic wave equation 49

2.4.5. Photoacoustic wave detection by probe beam deflection 50

3. Experimental setup **55**

3.1. Pump-probe technique 55

3.2. Photoacoustic response (PAR) by probe beam deflection 60

3.3. Other techniques 62

3.4. FCA reconstruction to absorption coefficient 64

4. $TlGaSe_2$ results and discussion **66**

4.1. Samples 66

4.2. Photoacoustic response of $TlGaSe_2$ 67

4.3. Absorption anisotropy 72

4.4. Photoluminescence and enhanced band edge absorption 78

4.5. $TlGaSe_2$ doped with Fe 84

4.6. Carrier trapping and recombination 88

4.7. Summary 94

5. Fluorescing 6H-SiC **97**

5.1. Experimental approach 97
5.2. Photoluminescence vs carrier lifetime 99
5.3. Absorption depth distribution 100
5.4. Carrier decay analysis 102
5.5. High injection level photoluminescence 109
5.6. Recombination scheme 112
5.7. Summary 113
6. 4H-SiC thin epilayers 115
6.1. Experimental approach 115
6.2. Carrier lifetime and surface recombination 117
6.3. Summary 124
7. 3C-SiC free standing wafers 125
7.1. Experimental approach 125
7.2. Absorption edge 126
7.3. Stressed regions influence to carrier lifetime 127
7.4. Summary 129
Concluding summary 131
Future outlook 134
References 135

List of abbreviations

ALD	Atomic Layer Deposition
CB	Conduction Band
CP	Critical Point
CV	Capacitance – Voltage
CVD	Chemical Vapor Deposition
cw	Continuous Wave
DAP	Donor-Acceptor Pair
dB	Deep Boron
DP	Deformation Potential
DPB	Double Position Boundary
EPR	Electron Parametric Resonance
FCA	Free Carrier Absorption
FSGP	Fast Sublimation Growth Process
FWHM	Full Width Half Maximum
IQE	Internal Quantum Efficiency
LED	Light Emitting Diode
OPO	Optical Parametrical Oscillator
PA	Photoacoustic
PAR	Photoacoustic Response
PL	Photoluminescence
RT	Room Temperature
SF	Stacking Fault
sB	Shallow Boron
SEM	Scanning Electron Microscope
SHG	Second Harmonic Generation
SIMS	Secondary Ion Mass Spectrometry
SRH	Shockley–Read–Hall
SRV	Surface Recombination Velocity
TE	Thermoelastic
TEM	Transmittance Electron Microscope
TG	Transient Grating
THG	Third Harmonic Generations
TMA	Trimethyl Aluminum
UV	Ultraviolet

Introduction

Growing interest and needs of modern semiconductor engineering require development of new materials offering new prospects. Electronics in the future should rely on wide bandgap semiconductors due to their fundamentally better properties than conventional semiconductor materials. In this study we investigate two dimensional (2D) layered $TlGaSe_2$ and three polytypes of SiC, namely, 6H, 4H and 3C. All of them are synthetically grown wide indirect bandgap semiconductors possessing long carrier lifetime, high electron-phonon coupling and relatively low luminescence yield.

$TlGaSe_2$ is a transparent semiconductor with promising optical and electrical properties, especially for applications in electronics and optoelectronics. Due to the high mass density, thallium-containing chalcogenides are promising sources of materials for the detection of hard radiation. By combining layered chalcogenides, the band gap can be tuned in a wide energy range (0.6 – 2.4 eV) and the crystal can be prepared in complex stoichiometries and crystal structures that can be used in photovoltaics. $TlGaSe_2$ is particularly known as insulating *p*-type photo conductor that at low temperature experiences para-to-ferro-electric phase transition. Its optical properties can be modified by annealing, by modifying excitation conditions as well as an external electric field within the phase transition range. Some properties are controversial and not well established. Investigation of $TlGaSe_2$ contributes to better understanding of the carrier transport, recombination and optical structure. Novel photoacoustic response technique is applicable for $TlGaSe_2$ showing material potential for optical switching.

Meanwhile, SiC is recognized as an attractive material for applications in high voltage, high power, high temperature devices and in radiation-rich environment. It exhibits large band gap, high breakdown field, high thermal conductivity and hardness. Every polytype of SiC has its own advantages and is aimed for the particular application.

Donor-and-acceptor doped 6H-SiC is a promising candidate for a light converting layer in a novel white LED application. The SiC epilayer can be

excited by nitride-based ultraviolet LED, which can be monolithically grown on the SiC substrate. Since the efficient luminescence conditions and growth parameters are not well established, N-B co-doped 6H-SiC layers are investigated to achieve proper conditions of high luminescence.

Homoepitaxial growth proves a solution to control 4H-SiC layer thickness and doping but in thin devices surface and interface quality may emerge as devise lifetime limiting factor. The 4H-SiC thin epilayers are investigated with passivated surface by SiO_2 and Al_2O_3 dielectrics to evaluate better technique and resistance to harsh radiation environment.

Although 3C-SiC is expected to have superior properties to those of the hexagonal polytypes, the sufficient layer quality is not achieved yet. Various growth methods are applied. Growth on Si substrates enables thick epilayer growth. In this study 3C-SiC free standing wafers are investigated on undulant Si in order to characterize its quality for further improvement of material growth technology.

Main goals

The thesis is aimed to obtain new knowledge about optical properties, structure and charge transport mechanisms in the indirect bang gap semiconductor materials of $TlGaSe_2$ and of some SiC polytypes, namely 6H, 4H and 3C.

Main objectives:

1. To examine $TlGaSe_2$ layered semiconductor crystals by optical techniques in order to explain optical, photoelectrical, electronic properties and its plausible optical anisotropy.
2. To determine doping conditions in highly co-doped with nitrogen and boron 6H-SiC layers grown by sublimation epitaxy for the efficient radiative light emission by examining carrier dynamics and recombination mechanisms.

3. To investigate the influence of 4H-SiC thin epilayers surface passivation by SiO_2 and Al_2O_3 dielectrics and to establish passivation to withstand harsh high radiation environment conditions.
4. To evaluate 3C-SiC free-standing epitaxial layer properties grown on undulant Si substrate for residual subsurface strain and its influence to carrier lifetime and material band gap.

Scientific novelty and importance

Photoacoustic response (PAR) using orthogonal pump–probe optical geometry was applied for bandgap absorption study in $TlGaSe_2$. The method, in the $TlGaSe_2$ at $E \perp c$ under stress confinement condition, was a sensitive tool to absorption study due to high refractive-index/pressure conversion factor and can be applied in other layered semiconductors.

Bandgap photoluminescence (PL) at room temperature in $TlGaSe_2$ and $TlInS_2$ was detected, which was not accounted before at RT. Using confocal spectroscopy it was shown that PL exhibits anisotropic behavior related to modified absorption properties. Band edge change was distinguished in the near surface region by in-depth free carrier absorption (FCA) measurements. At low temperature in ferroelectric phase bandgap absorption anisotropy in the layer plane was detected. Also a comprehensive study of carrier lifetime exaggerating the influence of stacking-fault traps and in crystals doped with Fe was provided.

In fluorescing 6H-SiC heavily co-doped with N and B layer wide optical and photoelectrical studies were performed to understand carrier transport and recombination mechanisms dependent on doping conditions.

In thin 4H-SiC epilayers surface passivation influence to epilayer carrier lifetime was investigated to determine the best passivation conditions using Al_2O_3 and SiO_2 oxides and its resistivity to radiation.

In free standing 3C-SiC epilayer detached from undulant Si substrate, the in-depth analysis was performed for the residual stress effects on carrier lifetime and bandgap absorption.

Statements to defend

1. Photoacoustic response (PAR) is shown as a sensitive technique to obtain absorption spectra in $TlGaSe_2$ due to high refractive index dependence on pressure and low absorption coefficients. PAR magnitude and its linearity in a visible range can be utilized for optical pulse switching.
2. Band-to-band photoluminescence is observed for the first time at room temperature in $TlGaSe_2$. Photoluminescence emission and absorption polarization dependencies suggest directionally localized weak exciton recombination across the layers.
3. In ferroelectric phase the anisotropy of absorption spectra is observed which shows theoretically predicted interlayer Tl^+ ions rearrangement.
4. In highly N-B co-doped fluorescent 6H-SiC high boron concentration reduces diffusion and enhances nonradiative carrier recombination time which is the base to improve luminescence performance at room temperature. The PL spectrum is composed of two overlapping peak bands caused by recombination from conduction band to deep boron (CB-to-dB) and from nitrogen to deep boron (N-to-dB).
5. After nuclear scattering damage at the interfaces of SiO_2/4H-SiC and Al_2O_3/4H-SiC the passivation with Al_2O_3 oxide is more resistant to this type of radiation damage.
6. In free standing 3C-SiC epilayer on undulated Si substrate the residual stress distribution along growth direction is observed. In the middle of the layer the unstrained region remains with long carrier lifetime and intrinsic bandgap absorption behavior.

Author's contribution

Author performed all experiments on free carrier absorption (FCA), carrier lifetime and photoacoustic response (PAR). Most of the experiments were performed utilizing nanosecond setup in Royal Institute of Technology (RIT), Stockholm.

The author processed and analyzed most of the data obtained by FCA, carrier lifetime, PAR, photoluminescence and other techniques. The interpretation of the results was discussed with scientific supervisor V. Grivickas and with other co-authors. The author prepared the drafts for publications [A3, A4, A5, B1, B6] and presented results at scientific conferences [K1, K4, K8, K9].

Coauthors' contribution

$TlGaSe_2$ photoluminescence was produced in BSU, Minsk; the photoinduced current measured in ITA, Vitebsk; theoretical modeling of photoluminescence and impurity absorption spectra was performed by V. Gavriušinas (VU). Some characterization on 6H-SiC was done by partners from Sweden, Japan and Denmark. In 6H-SiC time integrated photoluminescence was performed by M. Karaliūnas and M. Stasiūnas (VU); lifetime and diffusion coefficient measured utilizing transient grating technique by P. Ščajev (VU) and FCA temperature measurements performed by G. Manolis (VU). 4H-SiC CV measurements were performed by coauthors in Stockholm. 3C-SiC sample polishing was done by G. Manolis.

Layout of thesis

In chapter 1 an overview is provided of structural and physical properties of $TlGaSe_2$ and SiC polytypes along with particular polytype challenges to its specific application. Chapter 2 gives an overview on carrier dynamics and principles of FCA and PAR techniques. In chapter 3 main experimental setups for FCA and PAR are described with short description of other techniques. In Chapter 4 the results of $TlGaSe_2$ are described obtained by PAR, absorption, photoluminescence measurements (in undoped and doped with Fe samples) and its analysis provided. Chapter 5 presents broad investigation in fluorescing 6H-SiC while in chapter 6, the 4H-SiC epilayer passivation quality investigated and finally, in chapter 7, the 3C-SiC absorption edge measurements and lifetime study is provided. The thesis is finalized with a concluding summary and future outlook.

List of publications related to thesis

Publications related to $TlGaSe_2$

[A1] V. Grivickas, V. Gavryushin, P. Grivickas, A. Galeckas,V. Bikbajevas and **K. Gulbinas**, *Optical absorption related to Fe impurities in $TlGaSe_2$*, Physica Status Solidi A **208,** 2186 (2011).

[A2] V. Grivickas, A. Odrinski, V. Bikbajevas and **K. Gulbinas**, *Carrier trapping and recombination in $TlGaSe_2$ layered crystals*, Physica Status Solidi B **250**, 160 (2013).

[A3] V. Grivickas, **K. Gulbinas**, V. Gavryushin, V. Bikbajevas, O. V. Korolik, A. V. Mazanik and A. K. Fedotov, *Room-temperature photoluminescence in quasi-2D $TlGaSe_2$ and $TlInS_2$ semiconductors*, Physica Status Solidi (RRL) - Rapid Research Letters **8**, 639 (2014).

[A4] **K. Gulbinas**, V. Grivickas and P. Grivickas, J. Linnros, *Conversion of Laser Pulse Optical Energy to Photo-acoustic Wave in nm-Scale Layered $TlGaSe_2$ Crystals",* IOP Conf. Ser.: Materials Science and Engineering, **68**, 012004 (2014).

[A5] **K. Gulbinas**, V. Grivickas and V. Gavryushin, *Anisotropy of band gap absorption of $TlGaSe_2$ semiconductor by ferroelectric phase transformation*, Applied Physics Letters **105**, 242107 (2014).

Publications related to SiC

[B1] **K. Gulbinas**, V. Grivickas, H. P. Mahabadi, M. Usman, A Hallén, *Surface Recombination Investigation in Thin 4H-SiC Layers,* Materials Science (Medžiagotyra) **17**, 119 (2011).

[B2] M. Usman, A. Hallén, **K. Gulbinas** and V. Grivickas, *Effect of Nuclear Scattering Damage at SiO_2/SiC and Al_2O_3/SiC Interfaces – A Radiation Hardness Study of Dielectrics*, Materials Science Forum **717-720**, 805 (2012).

[B3] M. Syväjärvi, J. Müller, J. W. Sun, Y. Ou, V. Jokubavicius, M. Kaisr, K. Ariyawong, V. Grivickas, **K. Gulbinas**, P. Hens, R. Liljedahl, M. Linnarsson, S. Kamiyama, P. Wellmann, E. Spiecker and H. Ou,

Fluorescent SiC as a new material for white LEDs, Physica Scripta, **T148**, 014002 (2012).

[B4] V. Gavryushin, **K. Gulbinas**, V. Grivickas, M. Karaliūnas, M. Stasiūnas, V. Jokubavičius, J. W. Sun and M. Syväjärvi ,*Examination of Photoluminescence Temperature Dependencies in N-B Co-doped 6H-SiC*, Materials Science and Engineering, **56**, 012003 (2014).

[B5] V. Grivickas, **K. Gulbinas**, V. Jokubavičius, J. W. Sun, M. Karaliūnas, S. Kamiyama, M. Linnarsson, M. Kaiser, P. Wellmann, and M. Syväjärvi, *Carrier Lifetimes and Influence of In-Grown Defects in N-B Co-Doped 6H-SiC*, Materials Science and Engineering, **56**, 012004 (2014).

[B6] **K. Gulbinas**, P. Ščajev, V. Bikbajavas, V. Grivickas, O. V. Korolik, A. V. Mazanik, A. K. Fedotov, V. Jokubavičius, M. K. Linnarsson, M. Syväjärvi and S. Kamiyama, *Raman Scattering and Carrier Diffusion Study in Heavily Co-Doped 6H-SiC Layers*, Materials Science and Engineering, **56**, 012005 (2014).

[B7] G. Manolis, **K. Gulbinas**, V. Grivickas, V. Jokubavičius, M. K. Linnarsson, and M. Syväjärvi, *Temperature Dependencies of Free-Carrier-Absorption Lifetime in Fluorescent 6H-SiC Layers*, Materials Science and Engineering, **56**, 012006 (2014).

[B8] V. Grivickas, **K. Gulbinas**, G. Manolis, M. Kato and J. Linnros, *InternaI Stress in Freestanding 3C-SiC Grown on Si and Relation to Carrier Lifetime,* AIP Conference Proceedings, **1292**, 91 (2010).

[B9] V. Grivickas, **K. Gulbinas**, P. Grivickas, G. Manolis and J. Linnros, *Fundamental Band Edge Absorption in 3C-SiC: Phonon Absorption Assisted Transitions*, Materials Science Forum, **645–648**, 231 (2010).

Publications not included

[C1] S.S. Suvanam, M. Usman, **K Gulbinas**, V. Grivickas and A. Hallén, *A Comparison of Free Carrier Absorption and Capacitance Voltage Methods for Interface Trap Measurements,* Materials Science Forum, **780**, 465 (2013).

[C2] V. Grivickas, G. Manolis, K. Gulbinas, K. Jarašiūnas, and M. Kato, *Excess carrier recombination lifetime of bulk n-type 3C-SiC,* Applied Physics Letters, **95**, 242110 (2009).

[C3] V. Grivickas, V. Bikbajevas, K. Gulbinas, V. Gavryushin, and J. Linnros, *Strong photoacoustic oscillations in layered $TlGaSe_2$ semiconductor,* Physica Status Solidi B, **244**, 4624 (2007).

List of conference presentations

[K1] **K. Gulbinas**, V. Grivickas, G. Manolis, K. Jarašiūnas, M. Kato, *Excess carrier recombination lifetime of bulk n-type 3C-SiC,* 11-th International Conference-School Advanced Materials and Technologies, Palanga, August 27-31, 2009 (poster session).

[K2] V. Grivickas, **K. Gulbinas**, T. Malinauskas, V. Jokubavičius, M. Syväjärvi, J. W. Sun, Y. Ou, H. Ou, M. Linnardson, S. Kamiyama *Carrier Lifetimes in Fluorescent 6H-SiC for LEDs Application,* 39-oji Lietuvos nacionalinė fizikos 2011 konferencija, Vilnius, Lithuania, October 6-8, 2011, 2-1 (oral session).

[K3] M. Usman, A. Hallén, **K. Gulbinas**, V. Grivickas, *Radiation Hard Dielectrics for 4H-SiC*, International Conference on Silicon Carbide & Related Materials, Cleveland, Ohio, USA, September 11-16, 2011 (poster session).

[K4] **K. Gulbinas**, *Mechanics of photoacoustic effect in $TlGaSe_2$ semiconductor,* ADOPT Winter Conference-School, Romme, Sweden, March 22-25, 2012 (oral session).

[K5] V. Grivickas, **K. Gulbinas**, and P. Grivickas, *Photo-acoustic Pressure Effects in GaAs and $TlGaSe_2$*, High Pressure in Semiconductor Physics, (15-HPSP), Montpellier, France, July 25-27, 2012 (poster session).

[K6] V. Grivickas, **K. Gulbinas**, V. Jokubavičius, J.W. Sun, M. Karaliūnas, S. Kamiyama, M. Linnarsson, and M. Syväjärvi, *Carrier Lifetimes and Influence of In-grown Defects in N-B Co-doped 6H-SiC,* European

Conference on Silicon Carbide & Related Materials (9-ECSCRM) St. Peterburg, Rusia, September 2-6, 2012 (poster session).

[K7] S. S. Saveda, M. Usman, **K. Gulbinas**, V. Grivickas, A. Hallén, *A comparison of free carrier absorption and capacitance voltage methods for interface trap measurements,* European Conference on Silicon Carbide & Related Materials (9-ECSCRM) St. Peterburg, Rusia, September 2-6, 2012 (poster session).

[K8] **K. Gulbinas**, V. Grivickas, V. Gavriušinas, V. Bikbajevas, O. V. Karolik, A. V. Mazanik, A. K. Fedotov, J. Linnros, *Optinių savybių anizotropija kvazi-2D sluoksniuotuose* $TlGaSe_2$ *ir* $TlInS_2$ *puslaidininkiuose,* 40-oji Lietuvos nacionalinė fizikos konferencija, LNKF, Vilnius, Lithuania, June 10-12, 2013 2-1 (poster session).

[K9] **K. Gulbinas**, V. Grivickas, P. Grivickas, J. Linnros, *Conversion of Laser Pulse Optical Energy to Photo-acoustic Wave in nm-Scale Layered* $TlGaSe_2$ *Crystals,* European Material Research Society, EMRS, Lille, France, May 27-29, 2014 (poster session).

1. Overview of $TlGaSe_2$ and SiC properties

1.1. Properties of $TlGaSe_2$ layered semiconductor

For many decades, the $TlGaSe_2$ semiconductor compound is of interest due to the negative differential resistance regions in the I–V characteristics, optical second harmonic generation and giant photoacoustic pulse generation. It is promising material for X-ray and γ–ray detection due to wide bandgap, high mass density which is appealing to applications in biomedical imaging, spectroscopic instruments, security applications and higher resolution scintillation.

Since 1983, after discovering low temperature ferroelectricity, it was found a number of extraordinary and very uncommon properties that occur around the incommensurate *I*-phase between 107 - 120 K. *I*-phase fills the gap between the high temperature paraelectric (*P*-) and low temperature ferroelectric (*F*-) phases. Among these properties should be mentioned the negative crystal compressibility, the drop of dielectric susceptibility, changes in optical properties, tremendous sensitivity of the crystal to the external electrical field and the external illumination and the prehistory of crystal within the *I*-phase. Although $TlGaSe_2$ crystals exhibit transition into *F*-phase below 105 K, the particular structural changes at low temperatures are also not understood unambiguously.

The $TlMX_2$ (M = Ga, In; X = Se, S, Te) family of layered compounds is known as 2D semiconductors possessing layered or chained structure. Current review on obtained crystal structure, electronic properties and phase transitions could be found in Ref. [1]. The mostly investigated compounds are $TlGaSe_2$, $TlGaS_2$, $TlInS_2$ and their mixed alloys. Here we shall concentrate manly on the $TlGaSe_2$ keeping in mind that other ternary layered semiconductors are isostructural and share similar properties and structure. Some crystals under investigation are shown in Fig. 1.1.

$TlGaSe_2$ crystals of high quality were typically synthesized by modified Bridgman method from stoichiometric compositions of a melt [2]. Materials

used for growth were of 6N purity. The quartz tube with reagents is inserted into a thin quartz tube, evacuated and sealed. The tube is introduced into horizontal two zone furnace and temperature is increased in careful controlled manner up to melting temperature of 900º C. Temperature gradient is about 30 K/cm and hot zone is maintained at 980º C. Melt homogenized for 4 - 6 hours in the furnace and then translation initiated at a speed of 2 cm/day. When solidification is complete the top and bottom ends of the slab are removed to dispose segregated impurities. Our samples were selected from the most pure regions of bulk crystals and were obtained from different vendors. Obtained crystals were dark brown-red color and had cleavage normal to the c-axis. Additionally, metal chalcogenides as shown below exhibit some diversity in semiconducting properties but can be grown similarly in mixed complex stoichiometries.

Fig. 1.1 (left) $TlGaSe_2$ slab and a sliced thinner sheet of d = 200 μm in comparison to 5 cm long match; (right) three layered semiconductors $TlGaSe_2$ (same as in the left), $TlInS_2$, and $TlGaS_2$ with a characteristic absorption band of 2.14 eV, 2.34 eV and 2.64 eV, respectively. The band edge energy determines the color of the subband transmitted light.

The $TlGaSe_2$ crystals crystallize in monoclinic system which at room-temperature belongs to symmetry group $C2/c - C_{2h}^6$with unit cell parameter of a =10.771 Å, b = 10.772 Å, c = 15.64 Å. Crystallographic c^*-axis is slightly tilted from the normal to the layer plane c-axis and forms the monoclinic angle β = 100.06º. The crystal lattice contains 16 atoms on two adjacent layers [1, 3-5].

The stacking sequence in layers is shown in Fig. 1.2. Smaller units of $GaSe_4$ form tetrahedron with Ga atoms placed in the center and Se atoms

placed in the corners. These four tetrahedral units form larger ademantinelike polyhedron Ga_4Se_{10} which is linked by common chalcogene atoms at the corners connected with the next one. Four neighboring polyhedra are forming a layer plane (001).

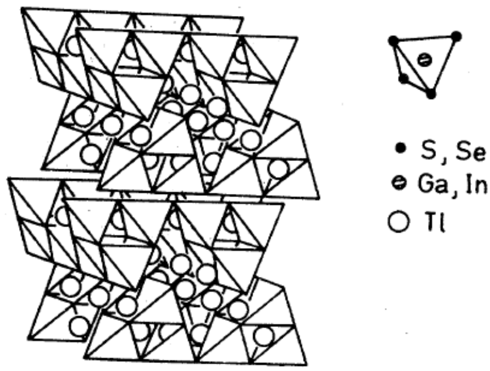

Fig. 1.2 $TlGaSe_2$ layered atomic structure: stacking of anionic layers and Tl^+ cations between them [3].

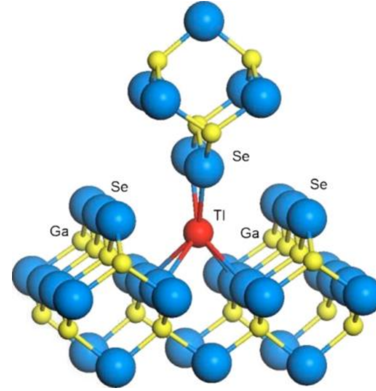

Fig. 1.3 The central part of crystalline structure of $TlGaSe_2$. Interlayer interaction depends mainly on the skew Tl-Se bonding Ref. [6].

In each successive case two anionic layers are stacked along the [001] (c^* direction) with Tl^+ ions placed between them. Structurally every succeeding layer is twisted by 90° to each other and forming trigonal prismatic cavities where Tl atoms lay in straight lines a[110] and $b[1\bar{1}0]$ that are parallel to the edges of the Ga_4Se_{10} groups. Tl-Tl distance length in the channel is ~3.90 Å while between the channels ~4.38 Å. In the layer plane the strong covalent forces prevail (Ga-Se ~ 2.37 Å), while a weak force prevails between the skew bond of Tl and six Se atoms ~ 3.45 Å (assumed mainly of covalent type) [4, 6, 7]. In the Fig. 1.3 the central part of crystalline structure is shown with the bonding between Tl-Se-Ga atoms.

Due to close proximity of the direct and the indirect bandgaps the crystal is often referred as a mixed direct/indirect bandgap semiconductor. It was found experimentally that direct bandgap optical transitions are allowed slightly due to low oscillator strength constant [8]. Theoretical calculations of the $TlGaSe_2$ band structure have shown that the top of the valence bands is

composed of Se:4p and Tl:6s wave functions, while the bottom of the conduction bands is composed of Tl:6p, Ga:4s and Se:4s states which showed the slight separation of indirect bandgap [9-12]. The valence band maximum lies in the Γ-point in the Brillouin zone diagram while the positions of the indirect conduction band valleys have shown controversy. Indirect minima of the conduction band was found theoretically in various directions between (Γ–Y) or (L–Z) lines depending on the calculation approach. According to Johnsen et al. [9], the indirect and direct bandgaps are separated energetically only by 90 meV (Γ–Y); Abdullaeva et al. [10] estimated a value 100 meV (Γ–Y) separation; Orudzhev et al. [11] – 50 meV (Γ–Y) and Kashida et al. [12] found only 10 meV (L–Z) separation. Only in the method of Ref. [9] the spin orbit coupling was included in the analysis. Nevertheless, (Γ–Y) and (L–Z) indirect conduction valleys are energetically close to one another as shown in Fig. 1.4. It is well known that theoretical calculations estimate smaller bandgap value E_g comparing to experimental results. Theoretical mismatch with experiment is of about 200 – 300 meV.

From the electrical measurements it was obtained that $TlGaSe_2$ always remains as high-resistivity self-compensating semiconductor of *p*-type

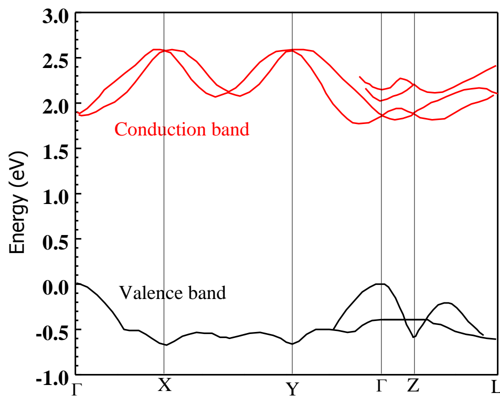

Fig. 1.4 Band structure of $TlGaSe_2$ obtained by Johnsen et al. [9]. Only the closest branches to the bandgap are shown.

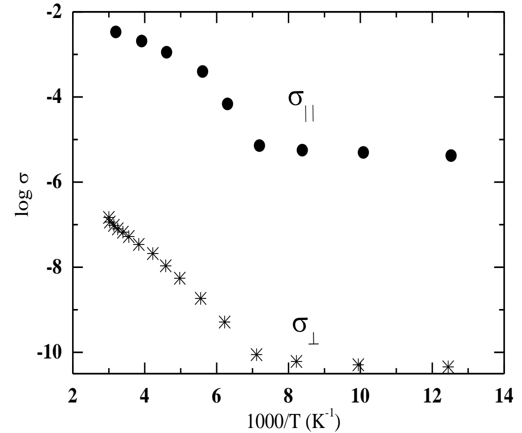

Fig. 1.5 Conductivity dependence on temperature in $TlGaSe_2$ [13]. Circles and stars denote conductivity parallel and perpendicularly to the layers, respectively.

conductivity regardless the doping. Conductivity increases exponentially above 150 K (see Fig. 1.5) [1, 13, 14]. Reported ratios of $\sigma_{||}^{0}/\sigma_{\perp}^{0}$ were nearly temperature independent but in different reports, were in the range from 10^3 to 10^8. This disagreement is presumably owing to the presence of stacking disorder [15] (see below) which density can be different [1, 13].

Majority carrier mobility (hole mobility) at RT in $TlGaSe_2$ is 65 $cm^{2/}Vs$ at RT [16]. Formation of defects in the bandgap due to other chemical elements in $TlGaSe_2$ is investigated extensively but, in fact, remains rather unclear because all impurities can be intercalated within layers or segregate in the clusters. However, many authors believe, that intrinsic stacking faults form deep defects acting as carrier trapping states within the bandgap.

Stacking faults are most common defects and the schematic view is shown in Fig. 1.6. It was estimated roughly that stacking fault can occur every fourth layer [14]. High stacking fault density may be a reason of the easy cleavage of the layers. Although one single layer consists of four atoms and cannot be observed even by scanning electron microscope (SEM), but the larger layered structures can be observed on a broken surface as shown in Fig. 1.7 [17]. Step like terraces obey structure openings where precipitates may fall or other defects prevail.

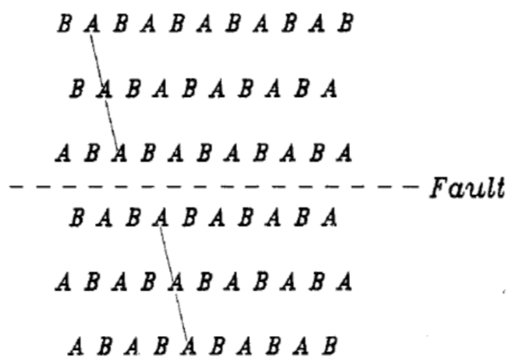

Fig. 1.6 Schematic diagram showing a stacking fault occurrence in $TlGaSe_2$ [14].

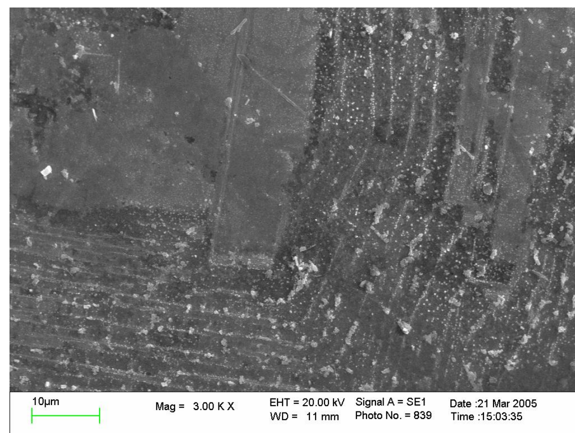

Fig. 1.7 SEM images of the defective $TlGaSe_2$ areas normal to the layer plane. Step like terraces open after cracking where precipitate may segregate [17].

Many optical spectroscopy studies have been performed under normal light direction perpendicularly to the layer plane. It was revealed predominant enhancement of optical transitions above the indirect bandgap edge. Different simplified approaches were used to extract the bandgap values where direct bandgap varied $E_g^d = 2.08 - 2.23\ eV$ and indirect bandgap varied $E_g^i = 1.83 - 2.13\ eV$ [9, 13, 18-20]. Variation in the bandgap energy was attributed to the existence of different polytypes of $TlGaSe_2$ [21-23]. However, more likely, it has to do something with involvement of disorder parameter or with simplified band gap extraction approach in a narrow energy range. Perhaps the annealing history in the crystal (as discussed below) can be also important. More sophisticated indirect absorption formula including assisted phonons was used for bandgap extraction under parallel illumination to the layers in Refs. [8, 24]. In these measurements at T = 15 K multiple phonon absorption fringes were observed and it was shown that indirect exciton edge is situated below the direct exciton by ~40 meV. No resonance of refraction index was indicated at the lowest indirect and direct bandgaps but it was observed at 3.0 eV [25].

$TlGaSe_2$ crystals reveal pronounced photoconductivity in a wide temperature range. In the majority cases the photoconductivity was induced by above bandgap photo excitation [18, 26]. However, in some instances a strong impurity related photoconductivity was also reported and negative temperature photoconduction dependence was measured in two temperature intervals between 120 – 250 K [18, 27, A1]. The shallow acceptor trap centers for majority holes were detected by thermally stimulated current [28] and low temperature donor-acceptor pair (DAP) photoluminescence [29]. The activation energy ranging between 12 – 130 meV above the valence band with concentration above 10^{14} cm^{-3} were found.

The most comprehensive studies were done regarding Fe impurities in $TlGaSe_2$. X-ray diffraction revealed that up to few percent of Fe impurities have little effect on the crystalline structure and orientation [30]. Dielectric spectroscopy showed contrary that minor amounts of Fe atoms decrease the complex permittivity of the *I*-phase and blur its peculiarities in phase transition

region [31]. Electron paramagnetic resonance (EPR) revealed electron transitions between the spin multiplets (S = 5/2, L = 0) of the Fe^{+3} ion [30, 32] and identified the four structurally equivalent Fe^{+3} states similar to ones observed in $TlInS_2$ [33]. However, little is still known about the Fe impurity effects on the optical spectra. The only indication that Fe atoms slightly reduce the fundamental excitonic peaks was obtained in Ref. [34].

Very little is known about actual majority carrier recombination lifetime, carrier trapping and variation with excitation level. At an early stage of $TlGaSe_2$ investigation, Guseinov et al. [26] reported two values of free carriers' lifetime equal to 20 ms and 5 ms at 77 K obtained by photoconductivity decay after pulsed excitation with an additional background illumination. These values of lifetime were assigned to the recombination process involving a fast and a slow deep recombination center in the forbidden gap.

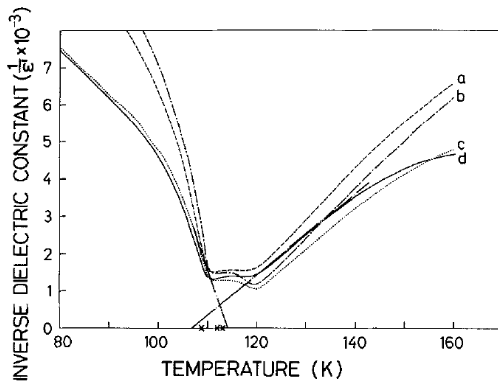

Fig. 1.8 Inverse of the dielectric constant $1/\varepsilon'$ versus temperature of $T1GaSe_2$ [36].

$TlGaSe_2$ undergoes several phase transitions with decreasing temperature as first reported by Volkov et al. [35] by dielectric spectroscopy and also by high pressure/temperature Raman studies [3]. The real part of the dielectric constant and heat capacity measurements versus temperature revealed anomalies at 110 – 120 K temperature range. Anomalies approximated well by Currie-Weiss behavior. The inverse dielectric constant dependence on temperature revealed phase transition at 110 K (Fig. 1.8) [36]. Later these phase transitions draw a lot of attention for this semiconductor and many authors studied it using various techniques, see review in Ref. [1].

Strong anisotropy of linear expansion coefficient was observed perpendicular to the layer plane around *I*-phase only in $TlGaSe_2$ (not observed in $TlGaS_2$ and $TlInS_2$) around T = 120 K [6, 37]. Measurements of sound

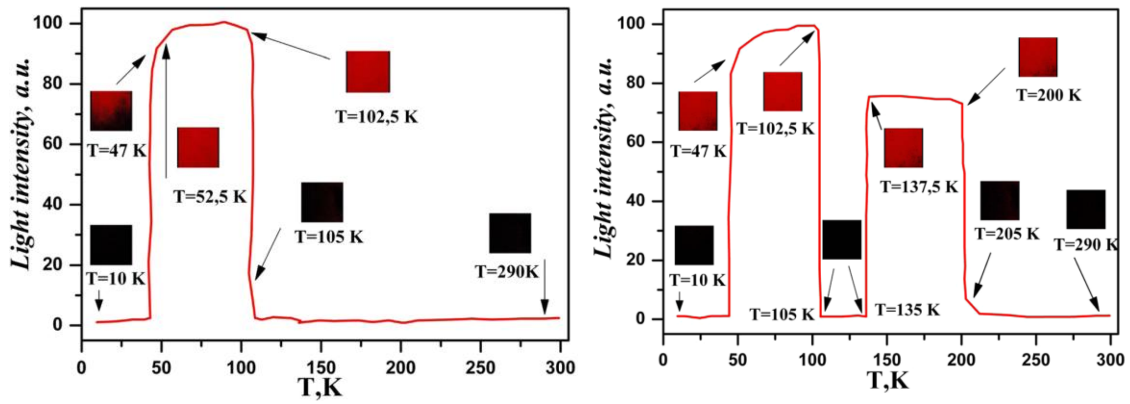

Fig. 1.9 Transmittance optical images detected at cross-polarized He-Ne light (dark field at 20 K) at different temperatures for $TlGaSe_2$. (left) Before annealing in *I*-phase and (right) after annealing at T = 113 K for 5h [42].

velocity versus temperature also yield positive peak jump as well as jump in heat capacity [36, 38].

Memory effects on thermal expansion coefficient were observed, after annealing at *I*-phase and under applied electric field, causing and the lattice expansion coefficient to change sign. Memory effect showed tremendous sensitivity to external electrical field and light illumination [39-41]. Moreover, annealing at *I*-phase substantially modified optical and electrical properties of the crystal. Polarized transmittance in the dark field over temperature was changing as shown in Fig. 1.9 [42]. It was explained by impurity subsystems modification over temperature at impurity excitation wavelength.

Annealing at *I*-phase showed influence on the Urbach tail which was detected below the so-called "intersection point" (Fig. 1.10) [43]. The intersection point and the Urbach energy parameter can be modified by

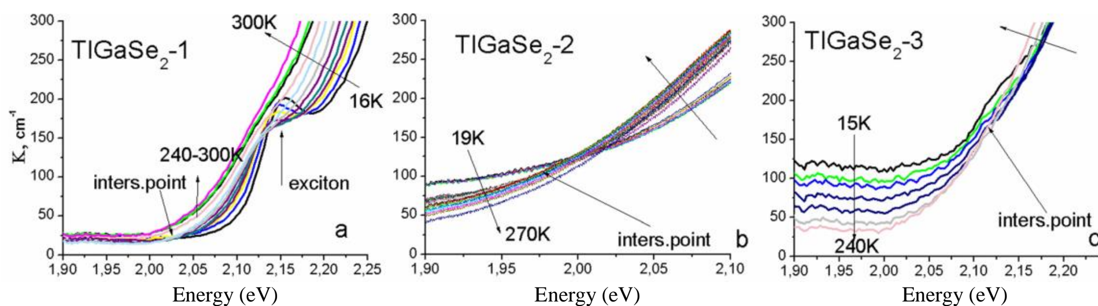

Fig. 1.10 Absorption spectra in $TlGaSe_2$ crystal types show different intersection point energy versus temperature [43].

annealing in *I*-phase. The results presented in Fig. 1.10 showed that several types of $TlGaSe_2$ bandgap shapes exist due to different growth condition. Some samples do not show excitonic behavior as in (b) and (c). In our experiments we investigated only the (a) type of crystals.

In literature, the intrinsic bandgap photoluminescence obtained by conventional technique was observed at low temperatures: in $TlGaSe_2$ at T < 2.2 K [44] which was attributed to donor-acceptor pair (DAP) emission up to 30 K [29] and in isostructural $TlInS_2$ at T < 100 K [45] when both materials reside in the *F*-phase. Higher range of PL in $TlInS_2$ is related to stronger direct bandgap exciton feature with the absorption value about $1.3 \cdot 10^3$ cm^{-1} at RT and $3 \cdot 10^3$ cm^{-1} at 77 K. Only rather recently the PL at RT in $TlGaSe_2$ was detected at 630 nm (1.97 eV) and attributed to the DAP emission [46]. The RT exciton emission was also discovered by confocal spectroscopy and reported in a conference abstract [47]. An inserted figure was for $TlInS_2$ and in the text of the abstract a similar result for $TlGaSe_2$ was noted. However, no explicit article was further published and no discussion of these results was provided.

1.2. Properties of SiC

Silicon Carbide (SiC) at atmospheric pressure is stable material for equal amounts of Si and C. The lattice building element is tetrahedron defined by strong coupling of sp^3 orbitals. Therefore, SiC can obtain different crystalline structures called as “polytypes”. Each polytype has identical atom arrangement in two dimensions while in the third dimension it is different. More than 200 polytypes of SiC have been distinguished experimentally. A few are generally used for technological studies and practical applications, namely, 3C-, 4H-, 6H-polytypes.

Superior physical properties make SiC a promising material for high temperature, high frequency and high power electronics. In general the bandgap and carrier transport parameters varies on polytype (see Fig. 1.11 and Table I). Polytype growth has unsolved problems with in-grown point defects,

micropipe, and dislocation density. For technological reason and for different application purpose each polytype must be studied separately.

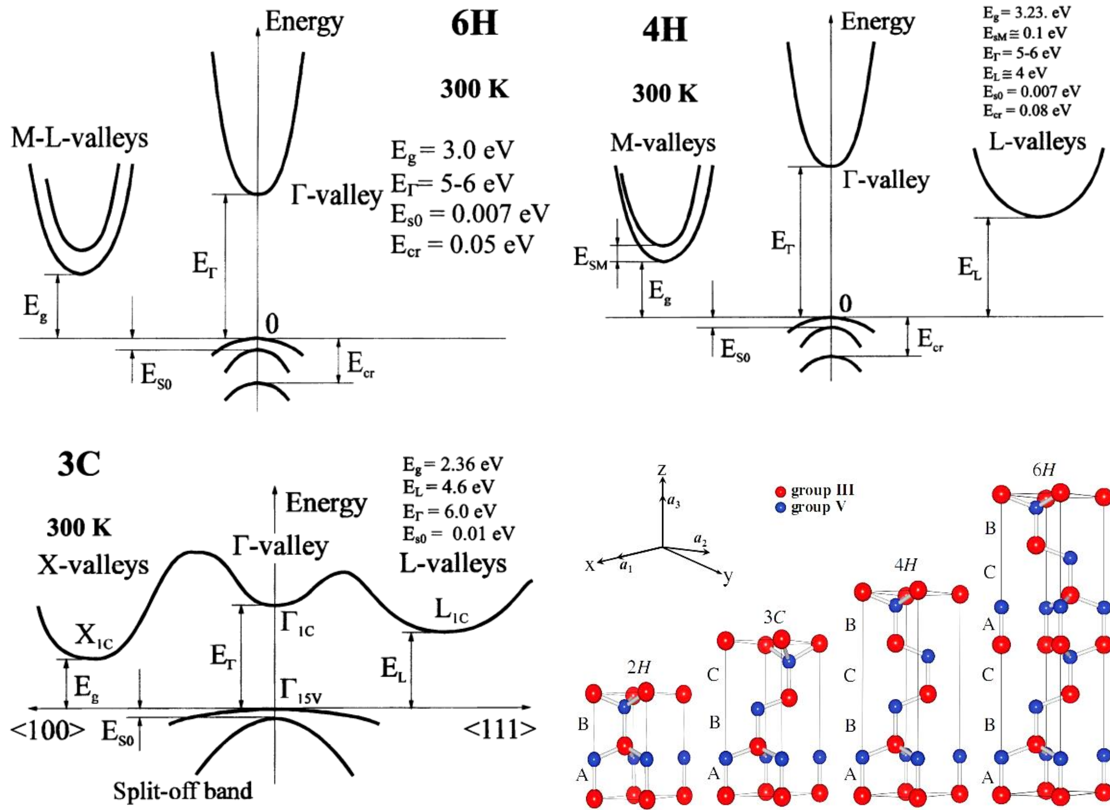

Fig. 1.11 Band structures of three SiC polytypes – 6H, 4H and 3C [48]. Stick-and-ball models are used according to Ref. [49]. Cations: red spheres; anions: blue spheres. The stacking sequence of the cation-anion bilayers are indicated by the symbols A, B or C. The primitive basis vectors a_1, a_2, a_3 are shown. The cubic (c) or hexagonal (h) character of a bilayer is defined by the nonparallel bond in this plane.

To describe atoms arrangement, the Ramsdell notation is used where the number indicates the number of bilayers in a unit cell and the letter denotes the crystal symmetry: H – hexagonal, C – cubic, R– rhombohedral. In Fig. 1.11 the four simplest SiC polytype stacking is shown.

All SiC polytypes have indirect bandgap structures which at room temperature parameters are shown in Fig. 1.11. The preference of SiC versus other conventional semiconductors (Si, GaAs) is clear from the Table I. SiC is superior due to its wide bandgap, high breakdown field, high saturation drift velocity and high thermal conductivity. Higher melting point allows using SiC

in high temperature environment which combined with low intrinsic carrier concentration due to the wide bandgap leads to low leakage current. The dopants at high temperature do not diffuse as easily as, for example, in Si. SiC is more resistive to chemicals and external radiation. Such properties are desirable in aircraft-spacecraft, automotive, defense and power electronics systems. Because of high breakdown field, the thinner SiC base can be used which results in smaller size of devices and faster recovery. The switching devices efficiency can be improved in DC/AC inverters for solar and wind power supplies, electric/hybrid vehicles and air conditioners. High thermal conductivity is desirable property helping to dissipate heat during device operation.

Table I . Properties of conventional and wide bandgap semiconductors at 300 K [48, 50].

Property	Si	GaAs	3C-SiC	4H-SiC	6H-SiC
Bandgap (eV)	1.12	1.4	2.36	3.26	3.02
Breakdown field (MV/cm)	0.25	0.4	1.2	2.2	2.5
Saturation drift velocity (10^7 cm/s)	1	2	1.2	2	2.5
Max. operating temperature (˚C)	350	460	1200	1200	1200
Melting point (˚C)	1410	1411	2830	2830	2830
Electron mobility ($cm^2/V\cdot s$)	1350	8500	900	1000	400
Hole mobility ($cm^2/V\cdot s$)	480	400	90	1200	100
Static dielectric constant	11.8	12.8	9.7	10	10
Lattice constants (Å)	5.43	5.65	4.36	a = 3.08 c = 10.08	a = 3.08 c = 15.12
Density (g/cm^3)	2.3	5.3	3.2	3.2	3.2
Mohs hardness	7	4-5	≥9	9.2.-9.3	≥9
Heat capacity	0.71	0.327	0.69	0.69	0.69
Thermal Conductivity (W/cm·K)	1.5	0.5	3.6	3.7	4.9
Thermal diffusivity (cm^2/s)	0.9	0.3	1.6	1.7	2.2

1.2.1. Fluorescent 6H-SiC application

Recently 6H-SiC has been emerging as a promising material for light emitting diodes (LEDs). In 2006 it was realized that after heavily co-doping with nitrogen (N) and boron (B) 6H-SiC can have very high donor-acceptor pair (DAP) emission efficiency at room temperature [51]. Traditionally, white light LEDs are made by mixing of blue and yellow color light. Blue light is generated from GaN LED which is partly converted to yellow light by a YAG:Ce phosphor. The phosphor degrades over time faster than GaN LED and the white light is turning blue over time. Moreover, the phosphor contains rare earth elements which may become scarce and expensive for huge market in the future.

New type of white LED light source based on fluorescent SiC (f-SiC) is formed on a basis of donor-acceptor pair (DAP) luminescence, for light conversion from near-ultraviolet (UV) using gallium nitride (GaN) based LED excitation (385 nm) source [51-54]. By stacking two layers of f-SiC, where one layer is doped with N and B and the other is doped with N and Al, the entire visible spectral range can be covered since the N-B and N-Al emits yellow (~590 nm) and blue (~480 nm) wide bands (Fig. 1.12). The color mixing in chromaticity coordinate plot is shown in Fig. 1.13. Tentative device with N-B f-SiC layer is demonstrated in Fig. 1.14 [53].

Few challenges arise for further improving f-SiC growth and to its

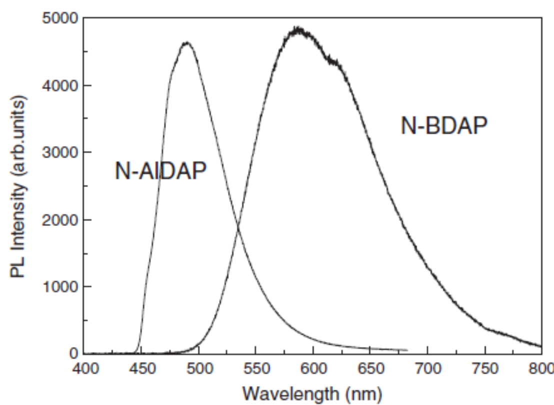

Fig. 1.12 Photoluminescence spectra of N- and B-doped and N- and Al-doped f-SiCs [53].

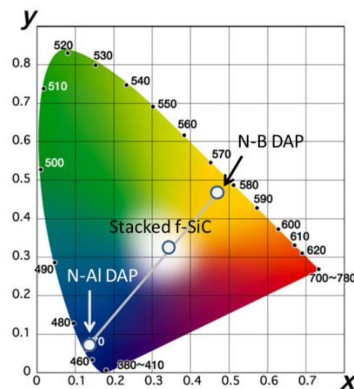

Fig. 1.13 CIE chromaticity coordinate plot of stacked f-SiC device [52].

practical application. First, voluminous layers are needed for efficient luminescence, thus high growth rates with heavily co-doping is desirable. CVD growth method provides 10 μm/h growth rate maintaining a reasonable morphology. Therefore, the natural habit of SiC sublimation was exploited and fast sublimation growth process (FSGP) invented [54]. Polycrystalline wafers grown in a special way highly co-doped with N and B are used as a source for f-SiC growth. The FSGP provides 50-300 μm/h growth rate which is controlled by an ambient pressure and in temperature range 1750 – 1900 ºC.

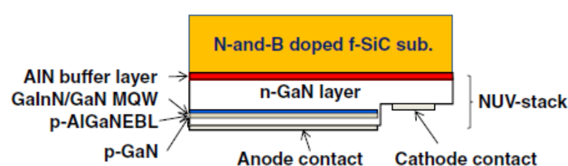

Fig. 1.14 Schematic diagram of white LED comprising f-SiC and nitride-based NUV stack [53].

Second challenge arises due to growth of GaN on the SiC wafer. Although hexagonal SiC is well established substrate for GaN growth because of low lattice mismatch, the nitride growth is performed typically on on-axis substrates, while 6H-SiC homoepitaxial growth is performed on off-orientation 3.5° substrates. 6H-SiC on-axis growth leads to 3C-SiC polytype formation issue. Therefore, growth conditions on the lower off-axis (1.4°) substrates started to be investigated.

New type of white LED light source based on fluorescent SiC (f-SiC) can offer a number of advantages: (i) high efficiency with high color rendering index (CRI), (ii) longer device lifetime due to monolithic GaN-SiC structure since GaN LED can be grown on SiC, (iii) simpler thermal management because of high thermal SiC conductivity; (iv) no need of rare-earth elements.

It was established that efficiency of the DAP emission increases dramatically by introducing large quantities of donors and acceptors in f-6H-SiC [51]. However no particular ratio or density for optimal behavior was established. It is desirable to maintain uniform doping distribution through the thickness of the hundred micron thick epilayer. The most simple emission mechanism exists in the Al-N co-doped 6H layer, since Al is on Si site with 0.25 eV energy above the valence band. The main challenge remains to

optimize the B-N co-doped f-6H-SiC layer. It seems like only a deep B center perhaps on the C site is involved in the DAP process but not a shallow B which is on the Si site [55, 56]. The B ratio of these centers and particular distribution nature is not established yet.

Theoretically, it was calculated that DAP light by B-N conversion with efficiency of 50 % could be enough with an appropriate CRI for high luminous intensity is better than in phosphor-based LEDs [51]. A single report provides luminescence efficiency of 35% but several other reports have shown 5-10% efficiency only. The high light conversion ratio means that radiative carrier lifetime should be of the same order as nonradiative lifetime. Millisecond lifetimes in DAP have been measured, while the nonradiative carrier lifetime of undoped 6H is of nanosecond scale or shorter [57]. Thus, basically it is unclear, how the DAP process can be complete with high conversion in the heavily co-doped B-N material. In this study the set of experiments was performed by different methods for physical carrier transport investigation in f-6H-SiC with high N-B co-doping. The aim was to estimate basic properties of emission, nonradiative recombination and carrier transport. Also to understand optimal conditions for improving next step in technology of N-B co-doping incorporation in such layers.

1.2.2.4H-SiC

The issue with 4H-SiC power devices is the reliability of the dielectric and SiC interface passivation since the bulk carrier lifetime in this polytype is substantially longer than in 6H-SiC. Considering the fact that surface and interface of thin epilayer is separated within a carrier diffusion length, the surface recombination losses compared to those in the bulk may emerge as a prevalent device lifetime-limiting factor [58].

The quality and resistivity properties of the oxide strongly influence the device performance exposed to high electric fields [59]. One specific area is related to 4H-SiC bipolar junction transistor (BJT), where the emitter-base interface degrades due to surface recombination. Surfaces states possibly are

related to the remaining carbon atoms or clusters at these interfaces which diminish the performance of the 4H-BJTs [60, 61].

Nowadays, the most widely used passivation for 4H-SiC is its native oxide SiO_2. This dielectric, besides many advantages, is characterized by low dielectric constant of 3.9, which is a disadvantage considering the high breakdown field and 2.5 times higher dielectric constant of SiC. A good quality SiO_2 is formed at high temperatures as one of the initial fabrication steps, while passivation should be done preferably at the end of the process sequence, when high temperature treatment brings a risk of degrading the device performance [62].

Alternatively, Al_2O_3 is a very promising oxide for SiC passivation due to the reasonably high dielectric constant 9.1 comparable to the 9.8 in SiC, high breakdown field (8 MV/cm) and relatively high conduction band off-set (1.7 eV). It is also interesting due to content of negative charge in dielectric beneficial for devices based on a low doped *n*-type voltage absorbing base layer since, it leads to the expansion of the space charge region at the periphery of the junction leading to a reduction of the electric field and increase in the blocking capability [62].

4H-SiC is also promising for applications in radiation rich environments. It is therefore important for devices, intended for high radiation exposure, to survive in such kind of environments and provide maximum resistance. Typical defects that arise after radiation exposure are surface defects at the interface of dielectric layers and 4H-SiC, which can play an important role for device reliability. These defects can affect the carrier mobility in MOSFETs and also lead to leakage currents and early breakdown of devices. Therefore the effect of ion irradiation at the interface of dielectric has been studied by employing specific ions in an energy range where elastic (nuclear) scattering dominates. SiO_2 has been studied in comparison to a potential alternative of Al_2O_3 to test the reliability of the interface after severe damage of energetic ions.

1.2.3.3C-SiC

Cubic 3C-SiC lattice is spatially isotropic and is not a subject to problem of micropipe formation which is a common problem in hexagonal SiC polytypes. Micropipes cause device degradation during high power operation. Moreover, interfaces between 3C-SiC and thermally grown oxides shows good characteristics compared with other SiC polytypes (i.e., interface SiO_2/SiC states are located inside the conduction band due to its lower bandgap) [63]. Combined with small donor ionization energy and high electron mobility it makes 3C-SiC polytype appealing candidate for optoelectronic applications and should lead to superior inversion channel mobility in MOSFETs.

Unfortunately, quality of grown 3C-SiC wafers and epilayers is a challenging task. Up to now 3C-epilayers were produced on other SiC polytypes with high point defect density: substitution of Si or C atom, impurity atoms in intermediate matrix (Si or C vacancies, anti-site defects),extended defects - dislocations, stacking faults, grain boundaries, double position boundaries, inversion domain boundaries, and inclusions. The most common defects are inclusions of other polytypes, twined domains and stacking faults [64].

During recent years the quality of 3C epilayers was improved by growth on (001) on-axis undulant Si substrates. Nevertheless, there are still many defects compared to 4H and 6H polytypes and the carrier lifetime still does not exceed hundreds of nanoseconds [C2].

Availability of Si substrates for epitaxial growth enables the creation of large-diameter 3C-SiC wafers which reduces device fabrication cost. However, heteroepitaxial growth on Si substrates introduces defects and strain (wafer warpage) in the resulting 3C-SiC layers due to large lattice mismatch (~20%) and different thermal expansion (~8%) coefficients. Wafer warpage is determined by the residual stress occurring in the hetero-structure system. The residual stress is generally divided into two parts, thermal stress induced by system cooling and intrinsic stress induced by deposition. Defects deteriorate

device performance, while strain introduces wafer warpage, which causes difficulty in photolithography [65].

To reduce defects and strain the growth on undulant Si substrates (Fig. 1.15) was applied. It reduces defect densities in the thick 3C layer due to stacking faults collision (Fig. 1.16) within the first ~50 μm. Therefore thick epilayers must be grown. For thick samples the microstructure change and intrinsic stress distribution may occur along the growth direction. Recently it was shown that after removal of Si substrate the 3C-SiC wafer appears to be saddle-shape, i.e., concave to the ridge of undulation and convex in the perpendicular direction [65]. Therefore, current research is focused on the defects and strain, which cause wafer warpage, influence on the electrical properties of 3C-SiC.

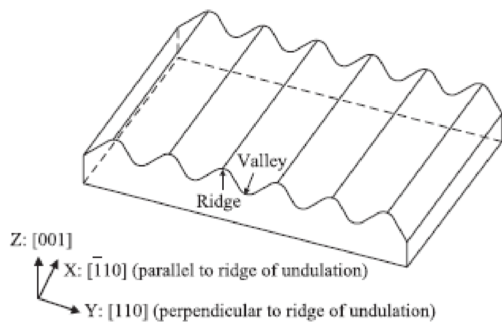

Fig. 1.15. Schematic structure of the undulant-Si substrate [65].

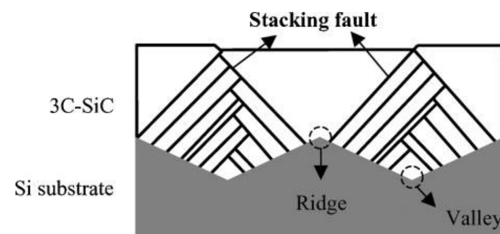

Fig. 1.16 The illustration of stacking fault collision during growth [65].

2. Carrier dynamics and optical techniques

2.1. Free carrier absorption (FCA)

Free carrier absorption (FCA) is an intraband absorption process involving occupied and unoccupied states in a conduction (valence) band. In this process, a carrier is exited into empty states by relatively low energy photons. Alternatively it can be viewed as the acceleration process of electrons (holes) by the high-frequency electrical field of the incident light, while carrier motion is restricted by the interaction of the carrier with lattice vibrations. By Drude model the FCA can be described in terms of harmonic oscillation ω which is inversely proportional to carrier relaxation time τ (the mean time between scattering events). Theory gives the following expressions for FCA coefficient:

$$\alpha_{FCA} = \frac{4\pi N e^2}{n_0 c m^*}\left[\frac{\tau}{1+\omega^2\tau^2}\right], \tag{2.1}$$

where N is electron-hole concentration, e is the electron charge, n_0 is the real part of refractive index, c is the velocity of light, m^* is the electron-hole pair reduced mass, ω is the electromagnetic frequency of the light wave.

Free carriers in bands can exist through several processes: (i) via band-to-band generation; (ii) via excitation from deep impurity levels present in bandgap with lower photon energy beams; (iii) via thermal excitation from shallow impurities.

The principle of induced free carrier absorption via pump-probe is shown in Fig. 2.1. Generated carriers are excited within conduction band by lower energy probe beam. Then the probe beam intensity obeys exponential relaxation back to equilibrium within the sample due to absorption of addition free carriers according to:

$$I(t) = I_0 exp\left[-\alpha_{probe}(t)\cdot d\right], \tag{2.2}$$

where α_{probe} is:

$$\alpha_{probe}(t) = \alpha_0 + \Delta\alpha_{FCA}(t). \tag{2.3}$$

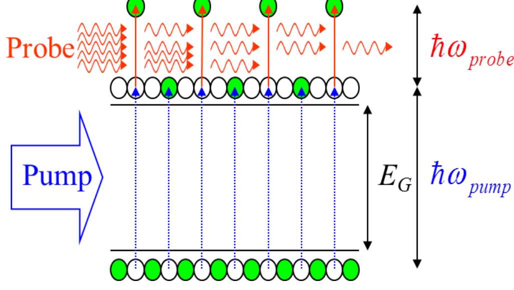

Fig. 2.1 Principle of free carrier absorption. Electrons are excited to the conduction band by a pump pulse where they can be absorbed by a probe beam and excited within the band [66].

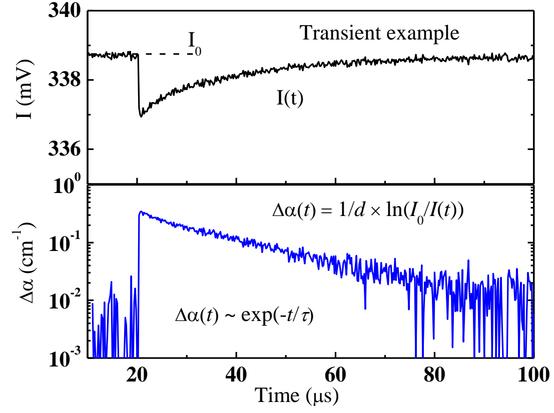

Fig. 2.2 (top) Probe beam transmittance $I(t)$ decay after pump pulse arrival at 20 μs and (bottom) recalculated $I(t)$ signal to free carrier absorption $\Delta\alpha(t)$ decay in semi-log scale revealing decay constant τ as obtained at RT in $TlGaSe_2$.

Here, d is the probing length (sample width) and α_0 is a constant absorption coefficient related to, for example, dopant induced free carriers, $\Delta\alpha_{FCA}(t)$ is induced FCA coefficient. Expressing α_{probe} from Eq. (2.2) at $\alpha_0 = 0$ we obtain $\Delta\alpha_{FCA}(t)$:

$$\Delta\alpha_{FCA}(t) = \Delta\alpha(t) = \frac{1}{d}\ln(\frac{I_0}{I(t)}). \tag{2.4}$$

An example of transmitted intensity $I(t)$ changes is show in Fig. 2.2 (top panel) with an input constant intensity of the probe beam I_0. After laser pulse arrival at t = 20 μs we observe transmittance intensity decrease and reverts back to equilibrium. By recalculating according to Eq. (2.4) we obtain FCA decay in Fig. 2.2 (bottom). The $\Delta\alpha(t)$ is related to the density of free excess carriers within the sample. If the damping constant 1/τ is intensity independent and does not involve impurity recharging, usually, a linear dependence is assumed:

$$\Delta\alpha(t) = \sigma_e\Delta n(t) + \sigma_p\Delta p(t) = \sigma_{FCA}\,\Delta n(t), \tag{2.5}$$

where σ_e, σ_p, σ_{FCA} constants are electron, hole and FCA cross sections, respectively; $\Delta n(t)$ and $\Delta p(t)$ are the excess electron and hole time dependent

concentrations. From FCA decay the carrier lifetime can be extracted numerically [67].

2.2. Carrier lifetime

The characteristic time for the system to revert to equilibrium is called the recombination lifetime. This is an important parameter in characterizing semiconductors because it determines the performance of devices and is a sensitive measure of material cleanliness and quality. Carrier lifetime may impact device performance by affecting turn-off speed (of a diode or thyristor) operating in high injections, the leakage current at *p-n* junctions, and excess carrier collection efficiency in solar cells. In many cases high lifetime is desirable. The low lifetime have application in a high-speed operation, generation of short terahertz pulses etc. For optically active devices nonradiative recombination must be suppressed to enhance internal quantum efficiency. Thus, lifetime measurements are important for verifying material quality as well as for monitoring contamination during subsequent clean room processes. Method is able to detect impurities down to a level of 10^{10} cm^{-3} [67, 68].

It is important to note that carrier lifetime usually is a function of the injected carrier density. In different excitation ranges, various recombination mechanisms are dominating. At very high injections and in heavily doped material Auger recombination is prevalent, while at lower injections recombination is impurity or defect dominated which is typically described by the Shockley–Read–Hall (SRH) theory [69]. In the SRH regime the low-injection carrier lifetime and the high-injection lifetimes are distinguished occurring at carrier densities below and above the doping density, respectively. In addition, other recombination mechanisms may be considered, such as trap-assisted Auger recombination and radiative recombination.

For the case of an excess carrier concentration, Δn, carrier lifetime (or recombination time) can be defined as:

$$\tau = \frac{\Delta n}{R} = -\frac{\Delta n}{\frac{d\Delta n}{dt}}, \tag{2.6}$$

where R is recombination rate of excess electron hole pairs. All recombination processes add up, thus resulting lifetime as inverse numbers:

$$\frac{1}{\tau} = \frac{1}{\tau_{SRH}} + \frac{1}{\tau_{RAD}} + \frac{1}{\tau_{Auger}}. \tag{2.7}$$

First term is multiphonon or SRH recombination; second, radiative recombination and, third, Auger recombination.

In the SRH recombination, electrons and holes recombine via deep trap levels. SRH recombination is most efficient for trap levels close to the middle of the bandgap. The recombination lifetime is given by:

$$\tau_{SRH} = \frac{\tau_p\left(\Delta n + n_0 + n_i e^{(E_T - E_i)/kT}\right) + \tau_n\left(\Delta n + p_0 + n_i e^{(E_T - E_i)/kT}\right)}{p_0 + n_0 + \Delta n}, \tag{2.8}$$

where n_0 and p_0 are the equilibrium carrier concentrations of electrons and holes, E_T and E_i the trap and Fermi energy levels for intrinsic material, respectively, Δn = Δp the excess/induced carrier density and τ_n and τ_p defined as:

$$\tau_n = \frac{1}{\sigma_n v_{th} N_T}; \quad \tau_p = \frac{1}{\sigma_p v_{th} N_T}, \tag{2.9}$$

where v_{th}, N_T, σ_p and σ_n are thermal velocity, trap density and cross sections for hole and electron capture cross section, respectively.

In radiative recombination electrons and holes recombine directly by emission of a photon. A third particle (phonon) must be involved for momentum conservation for semiconductors having indirect bandgap, thus, the radiative coefficient B is low:

$$\tau_{RAD} = \frac{1}{B(p_0 + n_0 + \Delta n)}. \tag{2.10}$$

Auger recombination predominantly occurs at very high injections since three particles are involved and the associated lifetime may be written as:

$$\tau_{Auger} = \frac{1}{(C_p + C_n) \cdot \Delta n^2} = \frac{1}{\gamma \cdot \Delta n^2}, \tag{2.11}$$

where C_p, C_n and γ are the Auger coefficient for *p-p-e*, *e-e-p* and sum of both processes, respectively.

Processes in Eq. (2.7) describe recombination in the bulk of semiconductor. Local processes can be affected also by carrier gradients. For thin epilayers surface recombination must be taken into account because it can reduce lifetime substantially. This is the result of quick carrier diffusion towards the surfaces where the high recombination rate (low lifetime) is dominated by surface recombination. The measured lifetime through thin epilayer is integrated via all thickness and is called effective (or epilayer) lifetime which can be divided in two components, bulk (as in Eq. (2.7)) and surface related:

$$\frac{1}{\tau_{eff}} = \frac{1}{\tau_{surf}} + \frac{1}{\tau_{Bulk}}. \tag{2.12}$$

Using this equation the τ_{surf} may be extracted if τ_{bulk} for thick slab is known. Moreover, surface lifetime comprises of two parts: the recombination due to surfaces defects and diffusion:

$$\tau_{surf} \approx \frac{\mathrm{d}}{S_1} + \frac{\mathrm{d}}{S_2} + \frac{4d^2}{D\pi^2}. \tag{2.13}$$

Here d is sample thickness or epilayer thickness, D – diffusions coefficient and S_1, S_2 – front and back surface recombination velocities (SRV), respectively. A direct model that involves analytical solutions of the fundamental mode of the excess carrier lifetime in a thin epitaxial slab by using the simple one-dimensional equation [70-72]:

$$\frac{\Delta n(x,t)}{\partial t} = D\frac{\partial^2 \Delta n(x,t)}{\Delta x^2} - \frac{\Delta n(x,t)}{\tau_b}, \tag{2.14}$$

with two boundary conditions $S = S_2$, $x = 0$ and $S = S_1$, $x = d$:

$$\Delta n(t)|_{x=0,d} = \frac{D}{S}\frac{\Delta n(x,t)}{\partial x}, \tag{2.15}$$

and the generation function of the form:

$$\Delta n(x,t) = \Delta n_0 \exp(-\alpha x)\delta(t), \tag{2.16}$$

where $\delta(t)$ is the unit impulse function of generated carriers. To obtain value of τ_{surf} for given τ_{bulk}, d, D, S_1 and S_2 Eqs. (2.14) - (2.16) must be solved numerically. However, numerical calculation is not convenient if parameters are not known precisely, or if they obey slight variation with injection level and needs to be varied. Alternatively, approximate analytical solutions for two limiting cases for $S_1 = S_2 = S$ and for $S_1 \gg S_2$ were established in ref. [73]:

$$\tau_{surf} \cong \frac{d}{2S} + \frac{d^2}{D\pi^2};\ when\ S_1 = S_2 = S. \tag{2.17}$$

The right hand side of this formula is composed of two terms which give the exact analytical surface lifetime solutions for $Sd/D \gg 1$ and $Sd/D \ll 1$. The first term ($d/2S$) can be interpreted as an effective time for recombination events at the surfaces if the diffusion component is fast enough [74]. The second term (d^2/Dπ^2) can be interpreted physically as the time duration for excess carriers needed to travel the distance from the middle of the slab to the surface plane. Another approximation for limiting conditions is when S_2 (equivalently as S_1) mathematically is set to zero or much smaller:

$$\tau_{surf} \cong \frac{d}{S_1} + \frac{4d^2}{D\pi^2};\ when\ S_1 \gg S_2. \tag{2.18}$$

Therefore, when $S_1 \gg S_2$ excess carriers recombine mainly at the S_1 surface with a higher SRV value. The main difference of Eq. (2.18) from Eq. (2.17) occurs because of doubling the effective slab thickness for the carrier diffusion term. Note, that an approximations of Eqs. (2.17) and (2.18) gives a small 4-5% error for the ratio $S_1 d/D \cong 1$ in respect to the exact numerical resultant solution [73].

2.3. Absorption processes

The number of carriers generated as a function of depth z within the sample is proportional to [67]:

$$g(z,t) = g_0(t)\frac{\alpha_{exc}(1-R)^2\exp(-\alpha_{exc}\cdot z)}{1-R^2\cdot\exp(-2\alpha_{exc}\cdot z)}, \tag{2.19}$$

where $g_0(t)$ is the incident areal density of photons, R - the reflection coefficient on front and back surfaces, and α_{exc} - the absorption coefficient for the excitation beam, z – penetration depth. Simplified approach can be applied for determining initial ($t = 0$) carrier concentration at the depth z of strong absorption:

$$\Delta n(z,0) = \Delta p(z,0) = \frac{\alpha_{exc}(1-R)\cdot E\cdot \exp(-\alpha_{exc}z)}{hv\cdot e\cdot S_{area}}, \tag{2.20}$$

where $\Delta n = \Delta p$ corresponds to the averaged excess carrier density in the epilayer; E – the pulse energy; hv – the quantum energy; e – electron charge; S_{area} – excited spot area (2.21). If $z = 0$, then we obtain excitation condition at the surface.

The intrinsic band-to-band absorption in the indirect gap semiconductor can be approximated including multiple phonon absorption process [75]:

$$\alpha_{bb} = \frac{n_B + \frac{1}{2} \pm \frac{1}{2}}{hv} \sum_p C^p \begin{pmatrix} A_1\left[hv - \left(E_{gx}^i \pm E_{ph}^p\right)^{1/2}\right] + \\ A_2\left[hv - \left(E_{gx}^i \pm E_{ph}^p + E_{ex}^i\right)^2\right] \end{pmatrix}. \tag{2.21}$$

Here, the upper "+" and lower "-" signs correspond to phonon absorption and emission, respectively. The first term represents optical transition to exciton bound levels, the second - to the band continuum levels. The $n_B = \left(\exp(E_{ph}/k_bT) - 1\right)^{-1}$ is the Bose-Einstein phonon population factor; the index p denotes the acting phonon with energy E_{ph}^p. Also here E_{gx}^i – indirect exciton bandgap; E_{ex}^i – exciton binding energy; A_1 and A_2 - absorption strength matrix elements; C^p – phonon strength element.

Analytical expression of direct allowed exciton absorption with phonon coupling was provided in Ref. [76]:

$$\alpha(h'\omega) = \begin{matrix} \frac{C_0 R^{\frac{1}{2}}}{h'\omega}\left[\sum_{n=1}^{\infty} \frac{2R}{m^3} \frac{\Gamma_m}{(h'\omega - E_m)^2 + \Gamma_m^2} + \frac{1}{2}\left[\frac{\pi}{2} - \arctan\left(\frac{h'\omega - E_0}{\Gamma_c}\right)\right]\right. \\ \left. - \sum_{m=1}^{\infty} \frac{R}{m^3} \frac{\Gamma_c}{(h'\omega - E_m)^2 + \Gamma_c^2} + \frac{\pi}{2} \frac{\sinh(2u^+)}{\cos h(2u^+) - \cos(2u^+)}\right] \end{matrix} \tag{2.22}$$

Here first term represents excitonic contribution and the remaining terms represent exciton continuum to the absorption coefficient, where $u^{\pm}$ is:

$$u^{\pm} = \pi(R/2)^{\frac{1}{2}} \left[\frac{[(h'\omega - E_0)^2 + \Gamma_c^2]^{1/2} \pm (h'\omega - E_0)}{(h'\omega - E_0)^2 + \Gamma_c^2} \right]^{1/2} \qquad (2.22)$$

Here mth -exciton (m = 1, 2, 3…) energy E_m and absorption strength C_0 parameters are:

$$E_m = E_0 - \frac{R}{m^2}; \; C_0 = \frac{4\pi(2\mu)^{3/2}e^2|M_R|^2}{nch'^2{m_0}^2} \; (5) \qquad (2.23)$$

Here E_0 is the bandgap energy, R – Rydberg energy (exciton binding energy), μ – exciton reduced mass, e – electron charge, M_R - matrix element for electron-photon interaction, c – speed of light, h' – reduced Planck constant. Empirical relation for mth exciton Γ_m line width is:

$$\Gamma_m = \Gamma_c - (\Gamma_c - \Gamma_1)/m^2$$

Γ_1 is first exciton line width and $\Gamma_c -$ is exciton continuum line width. Exciton fit according to this calculation was performed in layered GaSe [77].

According to Thomas et al. [78], the energy of donor acceptor pair (DAP) recombination is given in a first approximation by the equation:

$$E(r) = E_g - (E_a + E_d) + \frac{e^2}{\varepsilon r}, \qquad (2.24)$$

where E_g is the bandgap energy; E_a and E_d are the ionization energies of acceptors and donors; ε - dielectric constant; r - distance. For infinite distant pairs last term vanishes.

2.4. Photoacoustic wave (PA) generation by laser pulse

In this chapter we discuss photo acoustic (PA) wave generation mechanisms and its detection by probe deflection technique. We shall concentrate on longitudinal plain acoustic wave which is generated in the parallelepiped sample near the exited surface at $z = 0$ and travels along the z direction. PA wave may experience multiple reflections from back and front surfaces due to density difference of surrounded media. The pressure in the acoustic wave induces the change in the material refractive index which is traveling in z direction and then it acts upon a perpendicular probe beam. Beam deflection can be detected by a fast photoreceiver. In such geometry the

signal represents the time derivative of a bipolar acoustic pulse shape. The recorded transient is called photoacoustic response (PAR). The generated acoustic wave pressure is in few bar region in semiconductors. Pressure is induced by deformation potential (DP) mechanism. A small contribution from thermoelastic (TE) mechanism can also take place.

2.4.1.General mechanisms

There are a number of light-to-mater physical interactions which generate acoustic waves. High conversion efficiency from external energy to acoustic energy can be reached in case of dielectric breakdown, vaporization or material ablation. All of them occur in a destructive manner in the media under high densities of the optical field. In contrary, a weak interaction is always present: radiation pressure and electrostriction which occurs by polarization of molecules in a weakly absorbing media such as liquids and dielectrics (mechanism efficiency ~ 10^{-8}-10^{-12}). The inverse piezoelectric effect works for non centrosymmetric symmetry semiconductor crystals [79]. In the rest of the cases, when a short ns laser pulse excites semiconductor, the two mechanisms should be considered seriously: the thermoelastic energy deposition which produces thermal expansion by the temperature gradient and so-called the deformation mechanism based on electronic volume effect, which is associated with generation of nonequilibrium free electron-hole pairs [80-83].

2.4.2.PAR generation at unconstrained free surfaces

The temporal form of PAR depends on conditions of the crystal surface. There are the two limiting cases: rigid and free surface [80]. If surface is free to react on the expansion then excited surface atoms can move freely. In other words, the boundary stress at the surface plane is always zero. Therefore the bipolar PAR shape occurs on free surface. The opposite case is a rigid (completely constrained) surface, for example, by sample glued with another solid media like a transparent glass. In this case the acoustic energy is partly transmitted and/or partly reflected from the surface depending on the acoustic matching of the two substrates which is dependent on the density difference in

the materials. In all our experiments we have used samples with unbounded free surfaces; therefore, only temporal PAR form as generated on free surfaces is going to be discussed.

2.4.3.Stress confinement, deformation and thermoelastic mechanisms

Stress confinement is a condition which shows if the optical energy is deposited before the energy can propagate acoustically. The property depends on the actual absorption depth (inverse value of the absorption coefficient α); heat rising time (generation speed) related to the duration of the laser pulse τ_L and on the acoustical sound velocity, v_{ac} [80, 83]. The transfer function in conversion layer is determined by the multiplication of parameters $\alpha v_{ac}\tau_L$. If $\alpha v_{ac}\tau_L < 1$ the stress confinement condition is fulfilled strictly and the absorption generates amplitude of acoustic pressure to absorption coefficient of the media. This means that the spectrum of the generated PAR corresponds to an absorption spectrum distribution for the constant number of incoming photons. If $\alpha v_{ac}\tau_L > 1$ then the strong absorption condition is reached and the absorption depth becomes smaller than the area element which can propagate acoustically. Thus, the PAR magnitude saturates and the PAR starts to decrease with increasing absorption inversely proportional to absorption coefficient [80].

The example in Fig. 2.3 (a) corresponds to a band structure of a semiconductor at equilibrium (solid line) and perturbed state after electron-hole pair fast formation. In (b) the "molecular view" of the deformation potential is shown

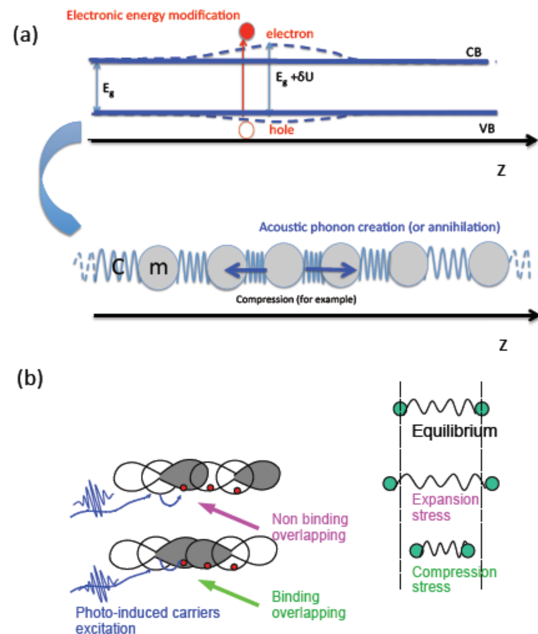

Fig. 2.3 Schematic representation of deformation potential according to (a) band structure and (b) “molecular view” [79].

where the different colors of orbitals correspond to different sign of the electronic wave functions. It depends on the nature of the orbitals if binding or non-binding orbitals overlapping occur which leads to either decrease or increase of interatomic distances, i.e., compression or expansion stress is generated, respectively. So, DP mechanism is a reaction of material due to electron-hole-phonon coupling [79]. In other words, the strain appears which means that nonequilibrium lattice phonons are created or annihilated.

The acoustic stress (σ) coming from the DP mechanism in a general formulation:

$$\sigma_{DP} = \sum_k \delta n_e(k) E_k \gamma_k = \sum_k \delta n_e(k) \frac{\partial E_k}{\partial \eta}. \tag{2.25}$$

Here $\delta n_e(k)$ is the change of electron concentration at the level k, E – energy and γ – mode Gruneisen coefficient, η is the strain. If we consider the limiting case for a photon energy equal to the bandgap (E_g), then the relevant variation of electronic energy level will concern that of the bandgap. As a consequence, the (2.25) can be simplified as:

$$\sigma_{DP} = \sum_k \delta n_e(k) \frac{\partial E_k}{\partial \eta} = N \frac{\partial E_g}{\partial \eta} = -NB \frac{\partial E_g}{\partial P} = -d_{eh} N, \tag{2.26}$$

where B is bulk modulus and $N(z,t)$ is photoexcited carriers concentration. This expression assumes an isotropic solid. In Eq. (2.26) the combination $B \frac{\partial E_g}{\partial P}$ provides the average of electron-hole action - deformation potential d_{eh} (eV). It can be separated into the coupling of electrons and holes:

$$\sigma_{DP} = -d_e n_e - d_h n_h = -d_{eh} N\,, \tag{2.27}$$

where n_e and n_h are the concentration at the bottom and top of the conduction and valence bands, respectively [79].

The deformation mechanism induces compression or expansion of the lattice determined by the sign of the deformation potential ($d_{eh} = dE_g/dp$). Negative d_{eh} sign (like in Si) denotes compression wave and positive d_{eh} (like observed in GaAs, Ge, GaSb) - the expansion wave. Lattice compression can

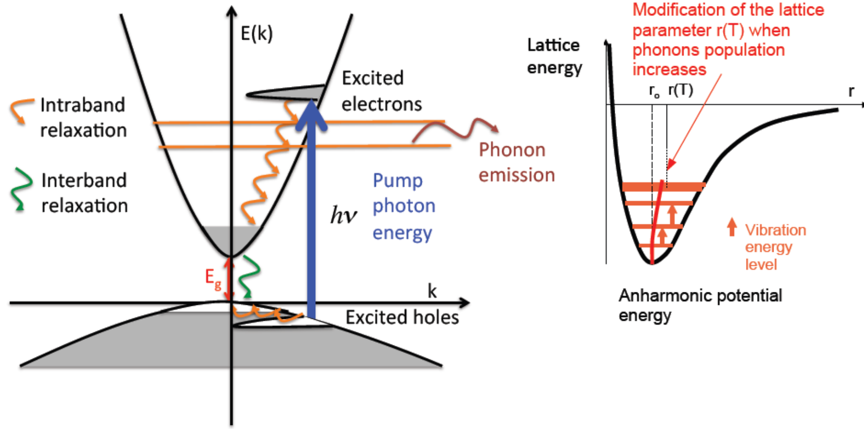

Fig. 2.4 Schematic representation of thermo elastic mechanism (left) in intraband relaxation process and (right) modification of mean interatomic distances [79].

be interpreted in terms of a semiconductor crystal's volume shrinkage on the density occupation of electronic energy levels while the lattice expansion causes crystal volume to increase. However, it should be stated that high carrier diffusivity and a high fraction of recombination during the laser pulse can substantially modify the observed temporal profile of the acoustic wave.

For absorbing media the thermoelastic (TE) process is also an important source for sound generation [79, 83, 84]. The TE process is based on a transient heating in a restricted excitation volume due to absorption of laser energy. Increased temperature results in the volume expansion (which is typically observed, but also can obey a shrinkage in a media with a negatively compressibility). The induced temperature gradient produces thermoelastic strain in the body:

$$\eta = \frac{\delta V}{V}. \tag{2.28}$$

The thermoelastic stress:

$$\sigma_{TE} = -3B\beta\Delta T(z), \tag{2.29}$$

where B is the bulk modulus, β is the thermal expansion coefficient in z-direction and ΔT is temperature change. The lattice heating comes from the energy transfer from the hot carriers' relaxation to lower energy levels, as shown in Fig. 2.4. This process emits optical or acoustic phonons in a time of ~1 ps [79, 82]. Thus, the thermoelastic contribution to the stress is determined

by the fraction of energy above the bandgap emitted phonons. Then, temperature difference can be calculated approximately by:

$$\Delta T = \frac{N(hv - E_g)}{C_V}, \tag{2.30}$$

where N is carrier concentration, C_V is heat capacity, hv is excitation quanta and E_g is the bandgap.

If recombination is occurring on a laser pulse time scale it also contributes to the thermoelastic pressure. When the recombination time is longer than the laser pulse duration, only usual relaxation thermoelastic generation prevails.

2.4.4. Acoustic wave equation

One dimensional wave equation for the particle displacement can be expressed [79, 83, 84]:

$$\rho\left(\frac{\partial^2 u}{\partial t^2} - v_{ac}^2\frac{\partial^2 u}{\partial z^2}\right) = d_{eh}\frac{\partial n}{\partial z} - B\beta\frac{\partial T}{\partial z}. \tag{2.31}$$

Assuming that both the carrier motion (first term) and the heat conduction (second term) have diffusive character, than spatial temporal evolution of the excited plasma and temperature rise can be modeled by the equations:

$$\frac{\partial n(z,t)}{\partial t} - D\frac{\partial^2 n}{\partial z^2} = 0, \tag{2.32}$$

$$\frac{\partial \Delta T(z,t)}{\partial t} - \chi\frac{\partial^2 \Delta T(z,t)}{\partial z^2} = 0, \tag{2.33}$$

Initial conditions for carrier concentration and temperature rise at the surface:

$$n(z,0) = \frac{\alpha_{exc}(1-R)}{hv_{exc}} \cdot \exp(-\alpha_{exc}z), \tag{2.34}$$

$$\Delta T(z,0) = \frac{\alpha_{exc}(1-R)Q(hv_{exc} - E_g)}{hv_{exc} \qquad C_V} \cdot \exp(-\alpha_{exc}z), \tag{2.35}$$

And boundary conditions:

$$D\frac{\partial n(0,t)}{\partial z} = 0, \quad \chi\frac{\partial \Delta T(0,t)}{\partial z} = 0 \tag{2.36}$$

Knowing the $n(z,t)$ and $\Delta T(z,t)$ distributions the Eq. (2.31) can be solved

$$\eta_{zz}(0,t) = \frac{1}{\rho v_{ac}^2}[3B\beta\Delta T(0,t) - d_{eh}n(0,t)\,], \tag{2.37}$$

The strain given by Eq. (2.37) is shown in Fig. 2.5 where ξ is absorption depth. One can see that for long ns times the strain can be divided into two parts. The region near $z = 0$ has a time-independent strain due to thermal expansion. The second part of the strain is a pulse which propagates away from the free surface at the speed of longitudinal sound v_{ac}.

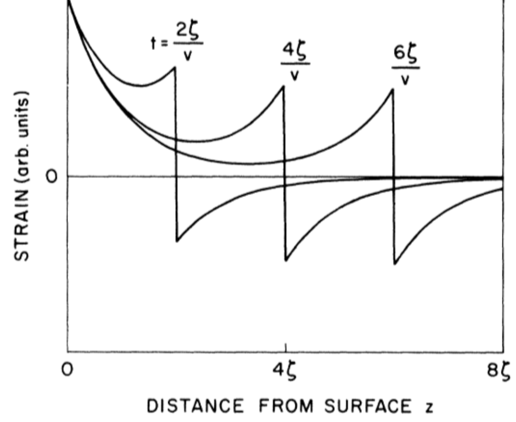

Fig. 2.5 The spatial dependence of the elastic strain at different times after the pump pulse absorption [84].

2.4.5. Photoacoustic wave detection by probe beam deflection

An ordinary PA detection scheme is when the piezoelectric transducer is placed on the back side of the slab sample. Then pressure is detected after calibration of the transducer. In our experiment we used optical approach which is based on perpendicular optical detection of the PA wave. This technique was applied for studies of PA signals in liquids [80] and is referred as *Shlieren* technique. A focused probe beam is directed to the lateral side through the sample. A knife edge cuts off half of the probe beam between two collecting lenses (see experimental setup in Fig. 3.5). This allows detecting of small variation of the refractive index induced by the passage of the acoustic wave. The time dependence of the photo receiver signal can be related to the acoustic pressure signal *p*(*t*) according to the following calculations in ref. [80]. The pressure induced change of the refractive index *n* can be well approximated by:

$$n(p,T) = n_0(T) + \left.\frac{\partial n(T)}{\partial p}\right|_{p\,=\,0} p\,, \tag{2.38}$$

where n_0 indicates the normal refractive index at temperature T and zero additional pressure. We may assume the second term on the right side is independent of the temperature:

$$n_1(T) = n_1 = \left.\frac{\partial n}{\partial p}\right|_{p\,=\,0} p. \tag{2.39}$$

We consider an acoustic wave propagating within a cylinder of pump beam spot diameter $d = 2a$ in the z direction (Fig. 2.6).

The change of the refractive index is proportional to the pressure according to Eq. (2.39) and assumed to be Gaussian in the (x,y) plane as the incident laser beam. (The same result has been deduced for cylindrical waves also [85]). The optical path $L_{opt}(z,t)$ of a beam crossing the acoustic transient is given by:

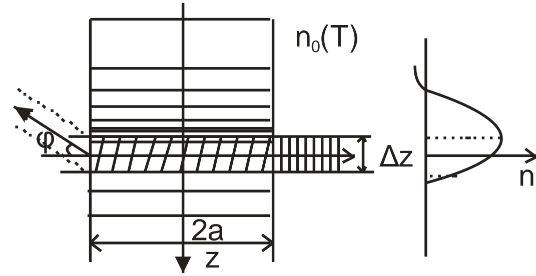

Fig. 2.6. Geometry of probe beam deflection, induced by the traversing gradient of the refractive index. $2a$ is equal to excited area or sample width [80].

$$\begin{aligned} L_{opt}(z,t) &= 2an_0 + \int_{-\infty}^{\infty} n_1\left(t - \frac{z}{c_0}\right) \exp\left(-\frac{2x^2}{a^2}\right) dx \\ &= 2an_0 + n_1\left(t - \frac{z}{c_0}\right) a \left(\frac{\pi}{2}\right)^{\frac{1}{2}}. \end{aligned} \tag{2.40}$$

For the fractional beams separation by Δz, one therefore obtains for the difference of the optical path ΔL_{opt}:

$$\Delta L_{opt} = a\left(\frac{\pi}{2}\right)^{\frac{1}{2}} \left.\frac{\partial n_1}{\partial z}\right|_{z\,=\,0} \Delta z. \tag{2.41}$$

Since

$$\frac{\partial n_1}{\partial z} = -\frac{1}{c_0}\frac{\partial n}{\partial t}\,, \tag{2.42}$$

one obtains an angular beam deflection in time $\varphi(t) \cong \Delta L_{opt}/\Delta z$:

$$\varphi(\mathrm{t}) = a\left(\frac{\pi}{2}\right)^{\frac{1}{2}} \frac{1}{\mathrm{c}_0} \frac{\partial n_1}{\partial t}\bigg|_{z=0}. \tag{2.43}$$

This deflection causes a parallel shift $\partial z = \varphi L$ of the probe beam after its passage through the second lens which is placed at a distance L from the interaction region in the sample. The part of the probe light intensity passing the knife edge is converted into a voltage signal by a photo receiver. Consequently, the relation between the beam shift ∂z and the relative change of the voltage signal ΔV compared to the *dc* voltage $V_0$is given by:

$$\frac{\Delta V(t)}{V_0} = \frac{\int_0^{\partial z}\int_{-\infty}^{\infty} I(z,y)dz\,dy}{\int_{-\infty}^{\infty}\int_{-\infty}^{\infty} I(z,y)dz\,dy} = \frac{\int_0^{\partial z} \exp(-2x^2/\rho_1^2)dz}{\frac{1}{2}(\frac{\pi}{2})^{1/2}\rho_1}, \tag{2.44}$$

where (z, y) represents the Gaussian intensity distribution of the probe beam radius ρ_1 at $x = L$. Equation (2.44) yields:

$$\frac{\Delta V(t)}{V_0} = \mathrm{erf}[2^{1/2}\phi(t)\pi\rho_0/\lambda] \quad (22) \tag{2.45}$$

where *erf* denotes the error function, $2\rho_1$ the focal spot diameter, and λ the wavelength of the probe beam. Hence, the photodiode signal does not depend on the distance L but only on the angular deflection $\phi(t)$, on the probe beam divergence $(\lambda/\pi\rho_1)$, and on the light intensity, which determines V_0. It has to be noticed that the error function and the photodiode signal are linear for small deflection angle ϕ, which corresponds to beam shifts $\partial z \leq 0.35\,\rho_1$. Introducing Eq. (2.43) and Eq. (2.39) in Eq. (2.45) yields for the transient signal on the photoreceiver:

$$\Delta V(z) = V_0\,\mathrm{erf}\left(k\frac{dp(t)}{dt}\right), \tag{2.46}$$

where:

$$k = \pi^{3/2}\frac{a}{c_0}\frac{\rho_0}{\lambda}\frac{\partial n}{\partial p}\bigg|_{p=0}. \tag{2.47}$$

For temporal pressure changes$dp/dt < 10^7$ bar/s we have:

$$\Delta V(t) \propto \frac{dp(t)}{dt}. \tag{2.48}$$

Therefore, the registered PAR detected perpendicularly is a measure of the time derivative of the acoustic pressure transient at the probe beam position.

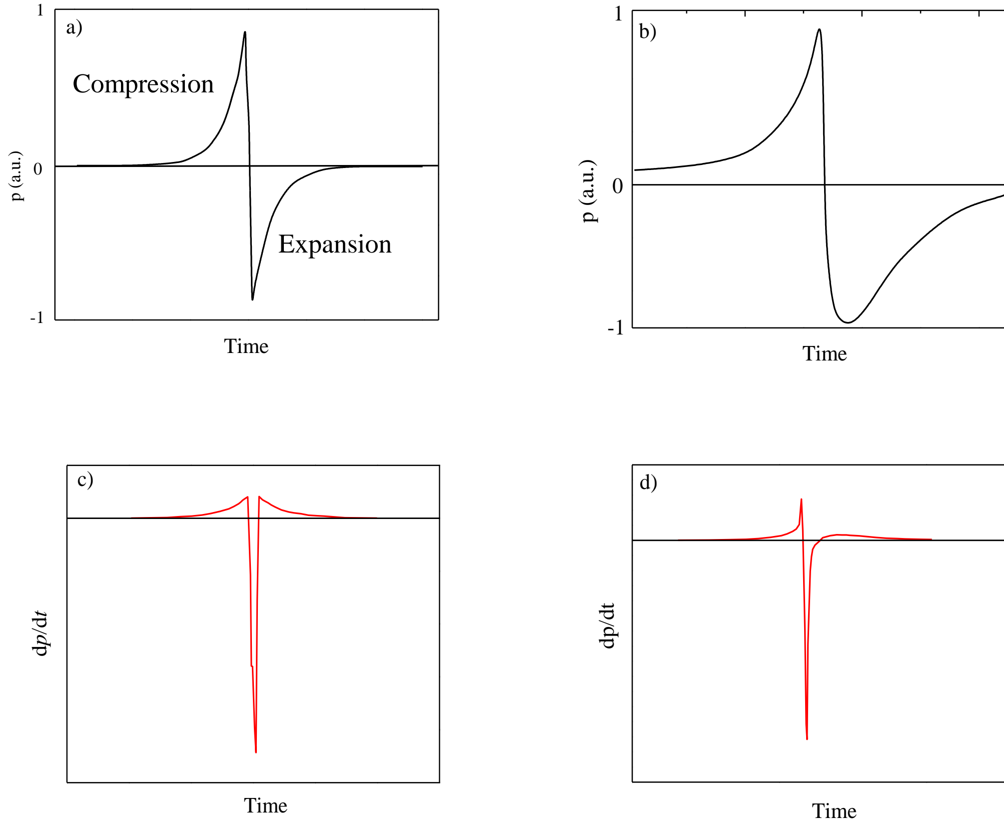

Fig. 2.7. PAR generated on free surfaces for (a) symmetrical signal (corresponding to low thermal diffusion); (b) its derivative; (c) PAR for asymmetrical signal including thermal diffusion; (d) its derivative [85].

An example of an ideal acoustic stress-confined PA wave induced by a laser pulse in a homogeneous medium is shown in Fig. 2.7(a) where the shape consists of compression and expansion counterpart waves. A subsequent expansion wave occurs due to free surface responding back to equilibrium. In Fig. 2.7(a) the PA shape is calculated without any thermal diffusion influence; in (b) the - heat diffusion (or carrier diffusion) is included [83] which expansion component makes asymmetrical; while in (c) and (d) PA pressure time derivatives are shown, respectively. The derivative (c) is of symmetrical shape while derivative (d) is slightly asymmetrical.

All theory stated above does not contain appreciable effects of sound dispersion of the acoustic waveform. We assumed that the longitudinal pressure wave propagates in one dimension without any diffraction and nonlinear effects. For large propagation distance, the shape of the strain pulse will leave the near-field region and become a spherical PA wave. As shown in Refs. [80, 83] boundary distance for these effects z_D can be estimated as $z_D = d_{spot}^2/4\lambda_{ac}$ (λ_{ac} – acoustic wavelength) or, for high α value, as $z_D = \lambda_{ac} d_{spot}^2$ approximately. So, it depends primarily on the pump laser beam diameter, d_{spot}. For d_{spot} = 0.1 cm and the sample thickness of 0.03 cm, $z_D \cong$ 0.1 cm which is appropriate for observing several PAR echoes in the sample.

3. Experimental setup

3.1. Pump-probe technique

Pump – probe technique can be exploited in two geometries [86]: the orthogonal and the parallel, referring to the angle between pump and probe beams (see Fig. 3.1). In orthogonal geometry the pump beam arrives to the front surface while the probe beam penetrates perpendicularly through lateral cross-sectional side of the sample allowing the depth-resolved investigation (Fig. 3.1(a), (b)). In the parallel geometry beams are intersecting in the same spot, which for example allows easy lifetime mapping on the surface. The FCA signal in the parallel geometry is averaged through the whole thickness of the sample. Being contactless and nondestructive, it is an appealing method for quick lifetime characterization [67]. The carrier concentration can be derived by calibration of the FCA cross section and, by varying the excitation pulse fluence with known absorption coefficient. This makes the method a research tool for separating various recombination mechanisms at different injections.

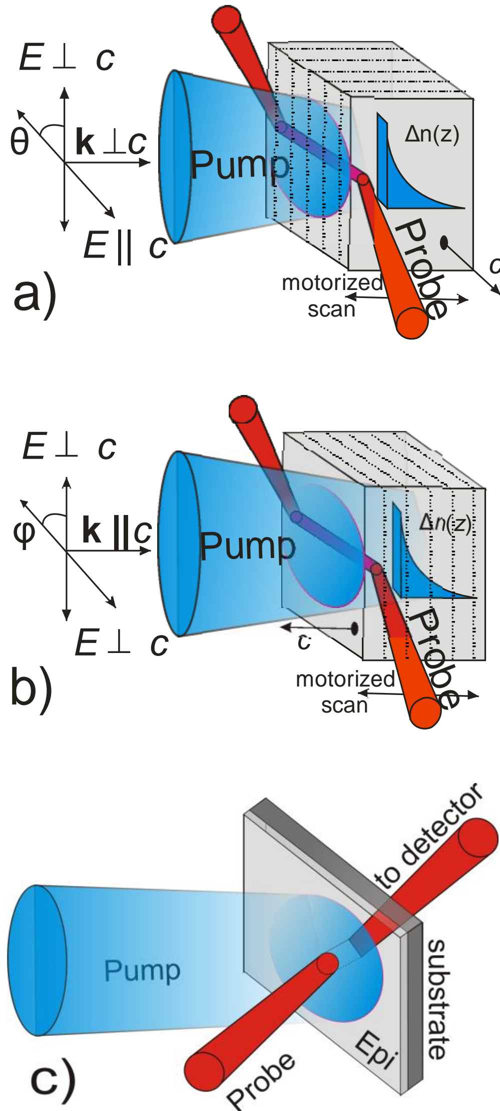

Fig. 3.1 Orthogonal pump-probe configuration where in respect to *c*-axis two notations are used (a) ***k*** || *c* and (b) ***k*** ⊥ *c*. (c) Parallel pump-probe configuration.

Moreover, for orthogonal

measurement configuration the excitation beam polarization angles are denoted in Fig. 3.1(a) and (b). Vector $\boldsymbol{k}$ defines excitation pulse propagation direction (in respect to c-axis of the sample as in SiC and $TlGaSe_2$), E is an electric field polarization vector. Layer plane in $TlGaSe_2$ is perpendicular to the c-axis (marked by dotted lines in Fig. 3.1(a) and (b)) . in By orientating sample we obtain two measurement cases: (i) when $\boldsymbol{k} \parallel c$ ($\boldsymbol{k} \perp$ layers), regardless electrical vector polarization angle φ, the light vector is always perpendicular to c-axis ($E \perp c$); (ii) when $\boldsymbol{k} \perp c$ the polarization angle θ can be rotated from $E \parallel c$ to $E \perp c$.

The pump beam spot must be large compared to the probe beam for ascertaining a homogeneously excited volume. The probe beam penetrates sample perpendicularly or, in some cases, at an angle close to the Brewster angle (not shown). Tilting the sample to the Brewster angle is essential for thin width samples (along probe direction) as multiple interference within the sample may dominate the refractive index by the excess carrier plasma.

In Fig. 3.2 the experimental set-up is shown. Solid black line represents the orthogonal pump-probe geometry and dashed line – the collinear geometry (appropriate optical elements are transferred on the beam path). Probe beam path remains the same for both configurations but the sample must be mounted accordingly.

Pump pulses of high energy with linear polarization are generated by a Q-switched *Infinity* (Coherent) Nd:YAG laser, pulse half-width is 2 ns, repetition rate is 40 Hz. Fundamental first harmonic passes second harmonic generation (SHG) crystal and then third harmonic generation (THG) crystal which tripled to output 355 nm (up to 300 μJ). Third harmonic is mainly used for SiC excitation. To obtain tunable wavelength excitation third harmonic is sent to OPO crystals. In OPO two beams are generated: the signal and the idler. The signal can be tuned in the 430 - 710 nm wavelength range and the idler operates in 710 – 1600 nm wavelength range. However, due to modes overlap at 710 nm wavelength, the reliable spectral region for measurements lay in the 430 – 690 nm and the 720 - 1500 nm ranges. Also, the power drops down to

the edges of spectral region and careful power monitoring must be performed within the tuning interval. Wavelength-set is controlled by computer. The output wavelength is calibrated using an external Ocean spectrometer which was double checked by narrow lines of the Hg lamp spectrum.

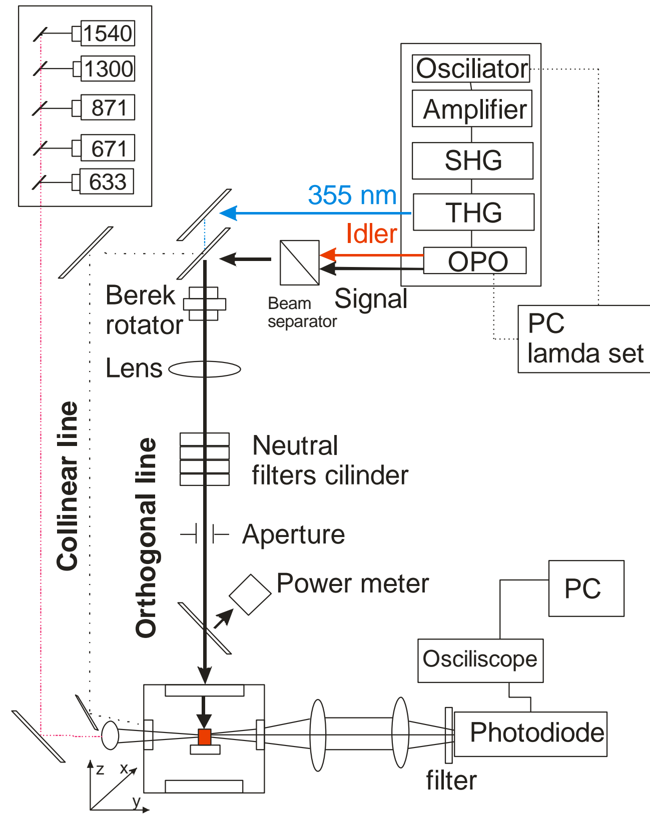

Fig. 3.2 Pump - probe measurement set - up. Orthogonal (solid) and parallel (dot) geometries are shown. For probing cw lasers were used of optional wavelength as described in the text.

On the exit, after passing OPO crystal, the excitation beam splits into the signal and the idler waves which propagate together slightly shifted in space but overlapping partly. Thus, the beam splitter or appropriate filters are used to separate them. Beam is guided by mirrors trespassing various optical components. On the beam path, the *Berek* rotator is used to select and rotate excitation polarization. Long focus (~1m) lens is used to focus the excitation beam to the sample. Excitation spot diameter is varied between 0.9 and 1.2 mm by shifting the lens position. The neutral filters are used to set wanted energy per pulse and the diaphragm of 4 mm diameter maintains beam quality. Flipping mirror is used to measure laser power just before it hits the sample.

The two power meters *Molectron* and *NewPort* are used which gives direct evaluation of the laser intensity.

The sample is attached typically to a cold finger cryostat which operates in the 77 K – 350 K range. A silver paste is used to provide good thermal contact. The cryostat is mounted on the motorized stage which allows sample transitions in three directions with 1 μm precision.

The red line in Fig. 3.2 represents the cw laser path used for probing. Few continuous wave (cw) lasers are available, namely 1540 (22 mW), 1300 (6 mW), 861 (40 mW), 671 (45 mW), 633 nm (2.5 mW). The tightly focused probe beam penetrates the sample and is collected by a system of two optical lenses to a 0.5 ns rise-time *New Focus* photoreceiver) which is connected to a digital 1 GHz bandwidth oscilloscope (with 2 GHz extension port) and to a PC.

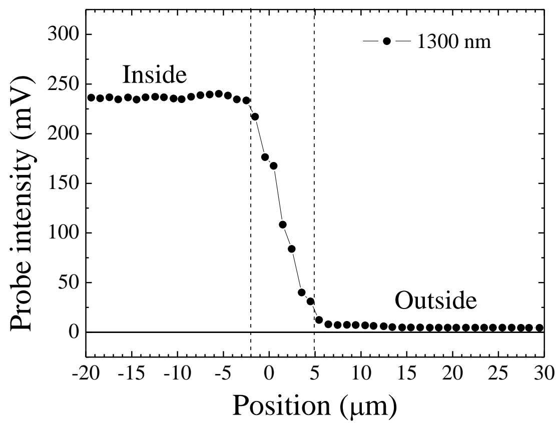

Fig. 3.3 Probe scan across the GaAs sample yields lateral resolution of 7 μm. Measurement is performed under Brewster angle geometry.

Comparing the geometries, one should note that the orthogonal scheme provides the depth resolution even though the excitation may be fairly inhomogeneous in depth. A motorized micro positioner of 1 μm is able to handle sample movements with precision. As focusing of the probe beam is crucial, each measurement is preceded by scanning of the probe intensity across the cross section (in-depth) of the sample by the sharp edge. The fall-off of the intensity at sample edges is an indication of probe beam focal point. Several scans using different lens-to-sample distances allow determining optimal focusing position. Fig. 3.3 represents such scan inside a sharply prepared GaAs sample of 1.1 mm width. The probe beam wavelength is 1300 nm and the scan is performed under a Brewster angle incidence. The applied fit gives the lateral resolution of about 7 μm.

The result can be compared with beam trajectory calculation (Fig. 3.4(a), [67]) on a 1 mm thick Si sample performed by Gaussian beam propagation theory. A high refractive index of semiconductor media clearly maintains a *soft* focusing of the beam in the sample. Fig. 3.4 (b) demonstrates overall calculated average diameter as a function of sample thickness for the parallel 2 mm of diameter probe beam before the lens.

The actual beam waist in air is determined by a knife edge scan. The resolution in a particular sample (*average focal diameter*) primarily depends on a focal distance of the lens, incoming beam diameter and wavelength, Gaussian shape quality. A higher resolution was obtained under focusing onto a front sample side. Previous experiments reported probe resolution investigations by a depth-resolved FCA [58, 87, 88] and by a depth-resolved absorption TG experiment [89-91]. The obtained best resolution varied from ~4 μm for 633 nm wavelength up to ~20 μm for 3390 nm probe wavelength.

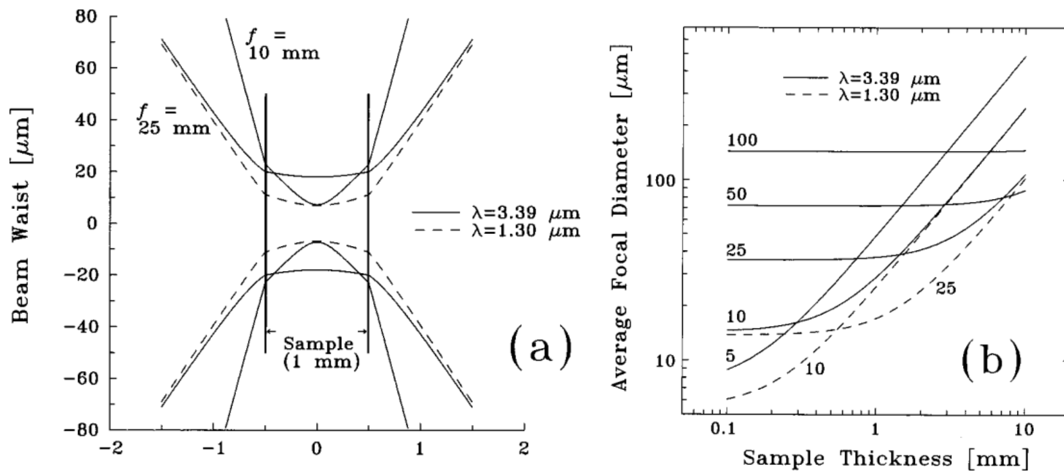

Fig. 3.4 Calculated beam trajectories at 90° incident angle for a probe beam properly focused within a wafer using lenses of 25 and 10 mm focal length. Note the difference in scale for the two axes. (b) Calculated average beam diameter within a sample vs sample thickness. Various lens focal lengths in mm are indicated. The average beam diameter may be taken as the lateral resolution set by the probe beam. The incoming parallel beam diameter before the lens was 2 mm [67].

3.2. Photoacoustic response (PAR) by probe beam deflection

For photoacoustic (PA) wave detection the orthogonal pump-probe set-up as shown in Fig. 3.2 can be exploited. Small modification must be made - in probe beam collecting part - a shadowing knife edge must be put between two lenses as shown in Fig. 3.5. The knife edge is set to block 40 - 60 % (along *z* direction) of the probe beam intensity. The beam deflection induced by the passage of the acoustic wave through the focused probe beam is monitored by a fast photo receiver.

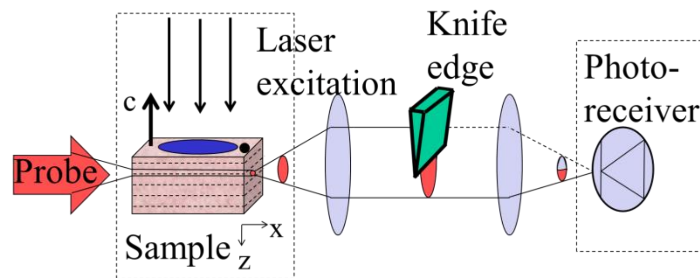

Fig. 3.5 Photoacoustic wave detection scheme. Excitation pulse generates the pressure wave which trespass the probe beam and causes beam to deflect. The 40 - 60 % of the probe is shadowed with knife edge to enhance the detection sensitivity.

When PA wave causes deflection, as described in chapter 2.4.5, the probe beam is diverted and the registered PAR polarity depends on the blocking side of the probe beam (Fig. 3.6) [92]. The blocking sides are denoted as front (excited surface side) and rear (back side). Front side blockage of the probe is shown in Fig. 3.5. In other words, the PAR polarity itself does not show the succession of compression and expansion pressure. The PAR polarity must be pinned to the scheme's arrangement (blocking side) and calibrated with a well-defined material (e.g., Si and GaAs [81]) to determine succession between compression and expansion pressure.

After PA wave is generated at the front surface it propagates across the sample with longitudinal acoustic velocity and experiences multiple echoes from the back and front surfaces (see Fig. 3.7). When PA wave is reflected it changes the polarity due to phase change by π. The change in wave propagation directions gives the same PAR polarity in the recording. In Fig.

3.7 PAR instant 1 is generated from the front surface, 2 - reflection from the back, 3 - reflection from the front, 4 - second reflection form the back and so forth. During time period between even or odd PAR transient, namely, 1st - 3rd and 2nd - 4th, PAR travels round trip or distance of a double sample thickness. No significant PAR magnitude decrease is observed in tens of reflections which indicate good surface quality. PAR magnitude is evaluated as ratio of whole PAR amplitude to initial probe intensity level in percent:

$$\mathrm{PAR} = \frac{\Delta I}{I_0} \times 100\ \%. \tag{3.1}$$

To get a clear image of PAR, the probing depth in the sample must be chosen correctly since compromise must be made due to multiple PA wave reflection from the back and front surfaces. Usually it is better to probe deep in the sample since the FCA decay interferes on the PAR near the surface. At the energies close to the bandgap where light penetrates deep in the sample PAR ads on FCA decay. Also, close to the boundaries of the sample, the incoming and the reflected PAR instances can overlap and the shapes are not resolved properly. If excitation quanta energy is even lower and penetrates via whole depth of the sample, there will be two PAR instances: generated on the front

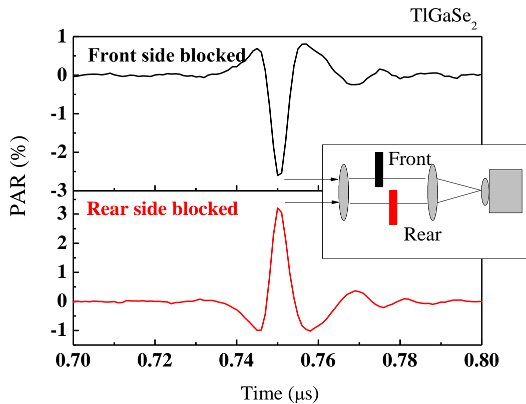

Fig. 3.6 PAR transient polarity is dependent on a detection scheme. PAR in $TlGaSe_2$ when front side of the probe beam is blocked is negative; when rear side – positive.

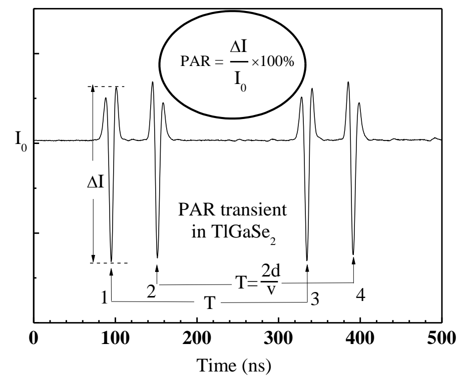

Fig. 3.7 Recorded transient with multiple PAR reflections. 1st – incident PAR, 2nd – reflection from the back surface, 3rd – reflection from the front, 4th – reflection from the back.

and on the back surfaces simultaneously which will propagate in opposite directions with opposite polarity [92]. As a consequence PA waves can meet in the middle of the sample and, therefore, signals can be distorted. To conclude, the best place to measure is in the middle of the rare half of the sample slab because: (1) it is further form the FCA signal dominating at the front surfaces; (2) generated PAR from the back surface does not overlap; (3) generated and reflected signals are equally spaced. As a matter of fact, in Fig. 3.7 transient is shown on this particular case.

3.3. Other techniques

The confocal photoluminescence (PL) and Raman measurements were performed in $TlGaSe_2$ in the backscattering geometry by Nanofinder HE (*LOTIS-TII, Belarus - Japan*) confocal system. The apparatus was equipped with a confocal 3D-scanning microscope with 0.95 numerical aperture achieving a large collection angle of emitted light from a nearly uniform segment on the selected surface and a 0.02 nm resolution spectrometer equipped with a cooled CCD camera. The excitation was performed by linearly polarized light of cw-laser at 532 nm, 473 nm or 405 nm wavelength. In most cases, the diameter of spot was about 200 nm.

Some other PL data was obtained using usual setups. Room temperature PL in five f-6H-SiC samples was measured using laser diode operating at 377 nm wavelength. Time-integrated PL study using 355 nm 25 ps duration pulses at various temperatures was performed in 6H-SiC ELS118 and ELS296 samples.

For transient grating (TG) technique in f-6H-SiC it was used 355 nm 25 ps pulsed laser in ns-long time scale measurements. The estimated absorption depth for such wavelength is ~11 μm ($\alpha \sim 900$ cm^{-1}). The period Λ of the TG was varied between 2 and 8 μm. The technique is based on monitoring diffraction efficiency grating decay time τ_G and varying the grating period Λ:

$$\eta(t) = \eta_{t=0} \exp\left(-\frac{2t}{\tau_G}\right), \frac{1}{\tau_G} = \frac{1}{\tau_R} = \frac{4\pi^2 D}{\Lambda^2} \quad (3.2)$$

The plot of inverse grating decay time $1/\tau_G$ vs $4\pi^2/\Lambda^2$ allows determining D (slope) and τ_R (intercept).

The investigation of carrier lifetime dependence on temperature in sample ELS118 has been performed in the collinear FCA measurement geometry with 351 nm 8 ps pulses of the TH from Nd^{3+}:YLF laser operating at 10 Hz. The FCA probing was performed in a collinear geometry with delayed pulses at either 1053 nm or 1064 nm wavelength in the transparency region of 6H-SiC. The delay of the probe was implemented optically, by changing the optical path of the ps-probe (to 4 ns), or electrically, when another YAG laser with 4 ns pulse was electrically synchronized with the pump laser (delay range ≈ 200 μs).

Photo-induced current transient spectroscopy (PICTS) was applied in $TlGaSe_2$ to examine carrier trap energy and its concentration. Thermally stimulated carrier emission from trap centers at particular temperature introduced the transient current. Long time component was analyzed of the photocurrent decay after the terminated excitation of a sufficiently long light pulse (to achieve steady-state condition). The samples were excited by a cw xenon lamp with photon energy selected by optical filter in the range of $h\nu =$ 1.84 – 1.93 eV. The frequency of photo excitation was set to 20 Hz with ratio of light-to-dark duration in the pulse as 1:6. The photon flux density was equal to $5 \cdot 10^{14}$ cm^{-2} s^{-1}. The sample was cooled in the darkness and PICTS measurements with current flow parallel to layer planes were performed in temperature range 77 – 320 K at the heating rate of 2 K/min. The photocurrent relaxation consisted of 2000 sampled points with 30 – 50 ms time quantization recorded at each 1 K step. All measurements were averaged over 50 transients to improve signal-to-noise ratio.

3.4. FCA reconstruction to absorption coefficient

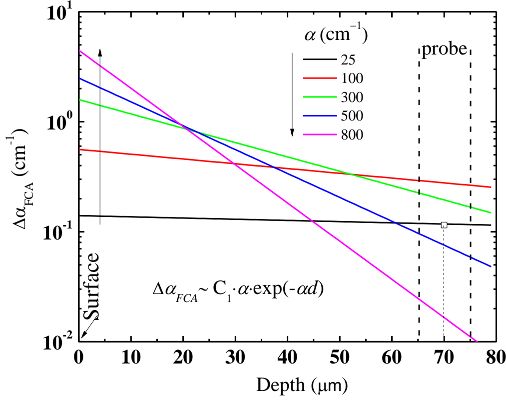

Fig. 3.8 Induced absorption $\Delta\alpha_{FCA}$ profiles shown for increasing absorption coefficient α. $\Delta\alpha_{FCA}$ profile in-depth drops exponentially overlapping at some point in depth. Black square data point is a pining point at measuring point (70 μm) for 605 nm excitation quanta.

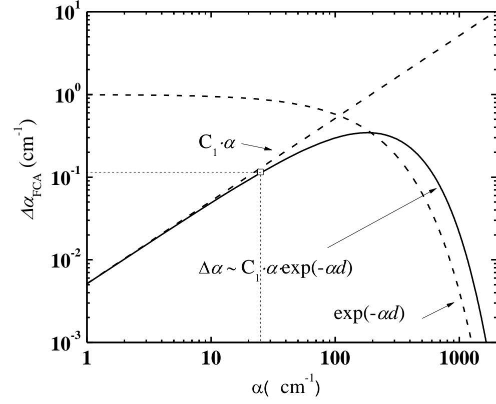

Fig. 3.9 Induced absorption $\Delta\alpha_{FCA}$ versus absorption coefficient value α at a certain probing depth (70 μm). Linear and exponential factors of Eq. (2.20) are shown by dashed lines. A pining point ($\alpha = 25$ cm^{-1} for 605 nm in $TlGaSe_2$) relates to the calibrated value.

FCA measured in orthogonal geometry represents absorption coefficient at certain depth but not on the surface exactly. As disclosed in Ref. [93], there are two alternative ways to extract the absorption coefficient α: either (i) from the exponential slope or (ii) from value $\Delta\alpha(0)$ at the incoming surface providing the calibration to the photon fluence as in Eq. (2.20). In Fig. 3.8 in-depth FCA depth profiles ($\Delta\alpha = N/\sigma$) are simulated and with increasing absorption coefficient the slope profile becomes steeper and at certain depth crosses lower absorption profiles. Thus the FCA value and spectral dependence would not be absolute. For example, spectra at 10 μm and at 70 μm depth would imply opposite dependence on α (Fig. 3.8). Therefore reduction of $\Delta\alpha_{FCA}$ in higher energy spectral region is more likely a footprint of an increased absorption which can be reconstructed to obtain surface absorption coefficient value using Eq. (2.20).

The simulated curve of FCA dependence at the depth of 70 μm versus the actual α is shown in Fig. 3.9. The linear and the exponential factor are given

by two dashed lines. Their product is resultant solid curve which show FCA dependence on the absorption coefficient. Eventually FCA starts declining after α is reaching 250 cm^{-1}. Note, that the resultant curve would be different at another probe depth position. For small α the FCA will be asymptotically close to a linearly proportional at the surface. For shown case, at d = 70 µm resultant FCA gradual slow increase reaches bending point at $\alpha \cong 250$ cm^{-1} and starts to decrease. We were pinning a low absorption coefficient 25 cm^{-1} from measured depth distribution slope to FCA value at depth 70 µm. (Pining point is shown Fig. 3.8 and Fig. 3.9). Thus we can reconstruct absorption coefficient from FCA spectra and attributing it to certain α value. Since one FCA value has two corresponding α values one must be careful to check the region around 250 cm^{-1}. In this way the reconstructed spectra was resolved in $TlGaSe_2$ and in 3C-SiC up to α = 2000 cm^{-1} and 200 cm^{-1}, respectively.

4. $TlGaSe_2$ results and discussion

4.1. Samples

For light penetration the optical surface quality must be achieved. Two different surfaces || *c* (perpendicular to the layer) and ⊥ *c* (parallel to the layer plane) were treated differently due to mechanical anisotropy of the material. For light penetration perpendicular to the layer plane (***k*** || *c*) the submilimiter thick slabs with mirror like surfaces were simply cleaved from the large pieces of the crystals by razor blade (scalpel). This cleavage produces mirror like surfaces, and no polishing or chemical cleaning is needed. However, the lateral surface preparation is much more difficult. 2 - 5 mm thick wide slabs have been cut and carefully polished on both lateral sides of layers cross cut planes along *a* and *b* crystallographic directions. Because $TlGaSe_2$ is a soft crystal – some corners crumbles after polishing. Therefore polished samples are cleaved again to remove damaged portion of a sample. The final samples thickness was of 200 - 300 μm with cleaved back and front surfaces (⊥ *c*) and polished lateral sides (|| *c*). Prepared sample is shown in Fig. 4.1 in respect to layered structure and perpendicular measurement configuration.

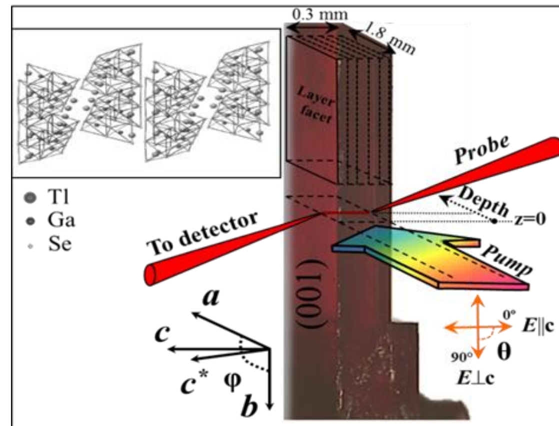

Fig. 4.1 $TlGaSe_2$ sample in respect to layered structure and perpendicular measurement configuration at ***k*** ⊥ *c* excitation direction [A3].

The 0.1, 0.5 and 3% molar ratios of Fe with respect to the Ga component were added in the melted mixtures of doped samples. The obtained $TlGaSe_2$:Fe specimens were increasingly darker with the increasing Fe content. Thermopower measurements showed a *p*-type conduction of all samples at room temperature.

The element ratio was identified by energy-dispersive X-ray spectroscopy (Appolo 300). The averaged values of Tl content was with a deficiency of 0.1 - 0.2%, Ga- with a deficiency of 1.3 - 1.4% and Se – with excess of 1.4 - 1.5% regarding to chemical formula. The presence of other elements was below detectability limit (0.1%). Samples with dopants (Fe = 0.1, 0.5 and 3%) also yielded the same tendency of three main constituents. From other literature reports it seems that Ga deficiency is typical for $TlGaSe_2$ samples [20, 94].

The Hall measurement was performed by Van der Pauw method with indium contacts had confirmed that our samples possess *p*-type conduction. An equilibrium hole concentration p_0 and Hall mobility μ_H along layers at RT have been estimated in one sample to be about $1.5{\cdot}10^{13}$ cm^3 and 65 cm^2/Vs, respectively. Such hole concentration and mobility values are in good agreement with data $5.9{\cdot}10^{12}$ cm^3 and 62 cm^2/Vs, respectively, reported by Qasrawi and Gasanly [95, 96].

PL investigation was performed in nine $TlGaSe_2$ samples: five initially undoped and four doped with Fe, Tb, B and Al and also in undoped $TlInS_2$.

4.2. Photoacoustic response of $TlGaSe_2$

Here we present obtained technical data on photo acoustic response (PAR) in $TlGaSe_2$ and the calibration measurements in GaAs. The results in $TlGaSe_2$ were obtained by probe beam deflection technique (see chapter 3.2) where excitation direction was $\boldsymbol{k} \parallel c$.

GaAs (100) was chosen because it is well established semiconductor and acoustical parameters are well studied in fs-to-ns pulse range [84]. Also, in GaAs PA pressure measurements were performed directly with piezoelectric transducer attached to the back of the sample at the similar ns pulse laser duration conditions reported by Song *el al* [81]. Song's results matching our PAR measurement in the energy range 1.4 - 1.75 eV are shown in Fig. 4.2 [K5]. PAR increases below 1.41 eV where stress confinement condition ($\alpha v_{ac} \tau_L < 1$) is satisfied. For large energies above 1.41 eV the absorption depth becomes smaller than the smallest area element which can propagate

acoustically, therefore, pressure starts to decrease following the dependence ~$1/\alpha$ [80]. In general, excellent agreement is found between our PAR spectrum measured by *Shlieren* technique and the spectrum obtained by conventional pressure detection.

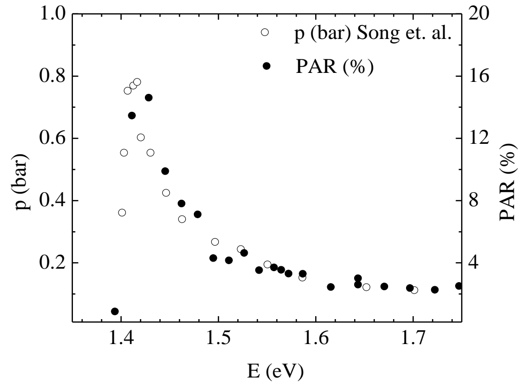

Fig. 4.2 Comparison of excitation spectrum of PAR in GaAs at 295 K with the data of Ref. [81] at the pump fluence of 2 mJ/cm^2. The results E > 1.41 eV cover the high absorption regime [K5].

Fig. 4.3 shows PAR echoes in $TlGaSe_2$ at RT in a 300 μm-thick sample for 6.3 mJ/cm^2 excitation fluence at different quanta below and above the bandgap. PAR shapes are symmetrical and no distortions are observed for laser fluence below the damage threshold (35 mJ/cm^2). This can be qualitatively explained considering that expansion and contraction stress components are proportional at the same depth and are not affected by any recombination change. PAR instants after multiple reflections show the same shape and amplitude which indicates high optical quality (small roughness) of the cleaved surfaces and low dispersion of

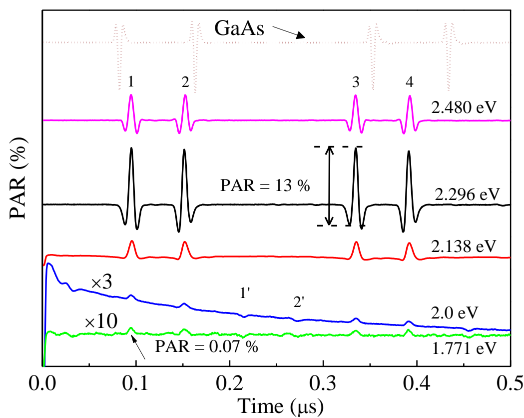

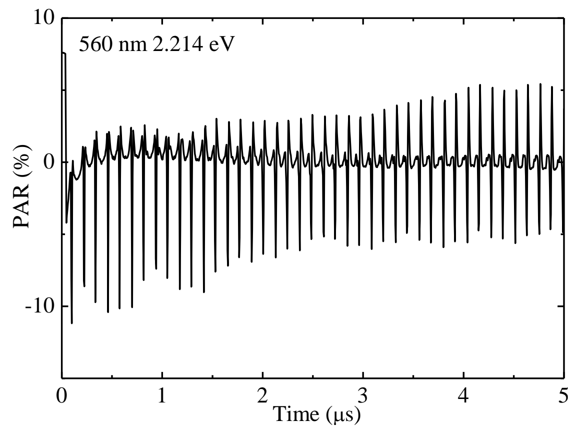

Fig. 4.3 Multiple echoes of PAR for different quanta energy at 6.3 mJ/cm^2 of fluence. Constant form of PAR after few reflections indicates a good optical quality of the cleaved surfaces [A4].

Fig. 4.4 Multiple echoes of PAR on 5 μs-time scale. Acoustic distortion of PAR shape (diffraction effects) is observed at t > 1. 5 μs [A4].

acoustic energy [80]. Some observable PAR shape distortion starts only above 1 μs transient time nevertheless slightly distorted PAR can be measured even above 5 μs (Fig. 4.4). Under a low excitation quanta in $TlGaSe_2$ (< 2.0 eV) the absorption coefficient is low enough to allow excitation through all the bulk of the sample. Then, the PAR superimposes on the background shape of the FCA decay. Also, in this spectral range, we observe a PAR generated from the back surface which is propagating in opposite direction and has the opposite polarity (the PAR depicted in Fig. 4.3 as (1`) - generated from the back surface and (2`) is a reflection from the front surface). This behavior was explicitly investigated by the laser pulse excitation on two opposite surfaces simultaneously [C3].

Fig. 4.5 depicts PAR measured at different excitation fluence of 2.194 eV at 77 K. Experiments were carried out in a wide spectral range 1.75 – 2.7 eV. At RT and 77 K, the PAR growth is observed over three orders of excitation laser fluence (see Fig. 4.6) and PA wave remains of the same shape though some FWHM narrowing occurs from 18 ns to 8 ns due to absorption depth shrinkage approaching 2.7 eV. The PAR increases linearly versus fluence at all spectral range. Few dependencies on excitation fluence are shown in Fig. 4.6 where magnitude of 70 % can be reached with no sign of PAR saturation. The small superlinear fraction at high intensities we explain by an additional input from the thermoelastic stress contribution by a fast recombination within laser

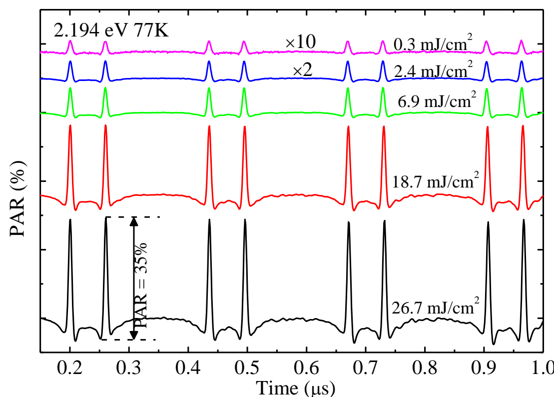

Fig. 4.5 PAR transients for different excitation fluencies at 2.194 eV at 77 K temperature [A4].

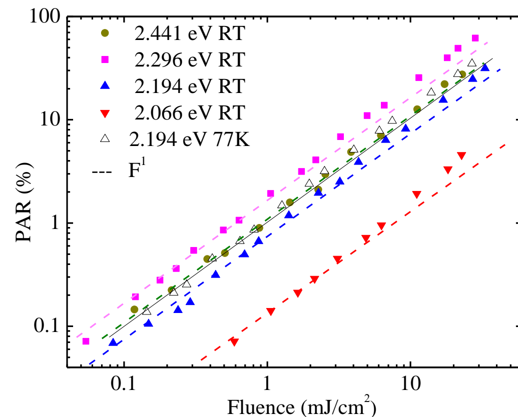

Fig. 4.6 PAR increases linearly with increasing laser fluence at different energy quanta at RT and at 77 K [A4].

pulse.

In contrast, in GaAs, the obtained PAR magnitudes saturate (Fig. 4.7) and a strong shape distortion is observed (Fig. 4.8). These effects can be interpreted by the fact that GaAs is a direct bandgap semiconductor with strong oscillator strength and with strong Burstein-Moss effect acting above the bandgap. In addition, GaAs has high carrier diffusion coefficients (> 5 cm^2/s at RT) and carrier dynamics must involve surface recombination. Primarily due to these effects the PAR saturates at RT for fluencies > 5 mJ/cm^2 and at 77 K the magnitude saturates at 2% of PAR for fluence > 0.5 mJ/cm^2 (Fig. 4.7) [K3]. So, the linear PAR in $TlGaSe_2$ with no sign of PAR saturation and distortion can be explained by predominantly forbidden electron optical transitions (low absorption with no Burstein-Moss effect because of indirect gap semiconductor) and the negligible carrier diffusivity which is obtained by lifetime analysis (discussed in further chapters).

It should be stated that two parameters determine amplitude in the *Schlieren* measurement of PAR: the deformation potential d_{DP} and the refraction coefficient dependence on pressure dn/dp which acts as a transfer function. In $TlGaSe_2$ both parameters still are not determined by independent experiments. However from our measurement we know that the sign of these

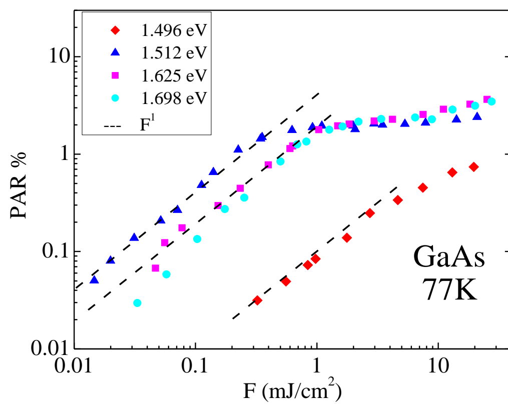

Fig. 4.7 PAR magnitude in GaAs dependence on fluence for several quanta energies at 77 K [K5].

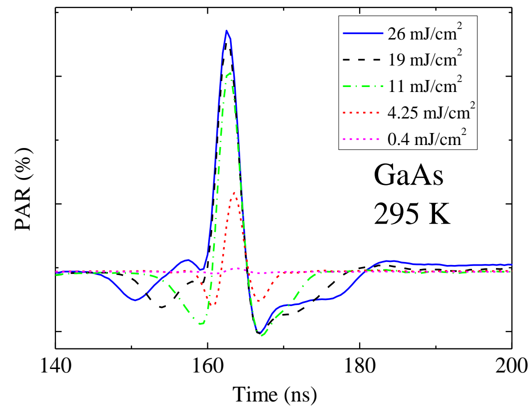

Fig. 4.8 PAR shape in GaAs becomes distorted with increasing fluence as shown at RT.

factors determine the actual PAR polarity. The PAR transients in Fig. 4.3 for identical experimental arrangement show, that PAR polarity in $TlGaSe_2$ is certainly opposite than in GaAs [K5].

We assume that sign of dn/dp in $TlGaSe_2$ must be positive as commonly observed in amorphous and 2D semiconductors and, contrary, the negative signs are observed in most of 3D crystalline semiconductors, including GaAs (dn/dp = 0.005) [97]. Assuming the positive sign for $TlGaSe_2$ and assigning experimental value of dn/dp determined in other layered crystals InSe and GaSe (dn/dp = 0.045) [98] we estimated the positive sign of deformation potential d_{eh} = 3 eV. It is three times smaller compared to known positive value for GaAs of d_{eh} = 10 eV [99]. Hence, high PAR of $TlGaSe_2$ is caused not by high deformation potential but most probably by the large dn/dp value. This value is controlled by interlayer spacing in $TlGaSe_2$ since the bandgap energy is controlled by interlayer Tl-6p and Se-4p electronic orbitals. These are the main factors that determine linear PAR dependence on the carrier injection and high PAR values.

The obtained results show that large dn/dp property and linearity of PAR in $TlGaSe_2$ can be exploited for optical switching. For example, a cw laser beam trespassing the crystal is controlling the circuit. Then a perpendicular laser pulse induces the deflection of cw beam which registered can turn on/off the optical or electrical circuit.

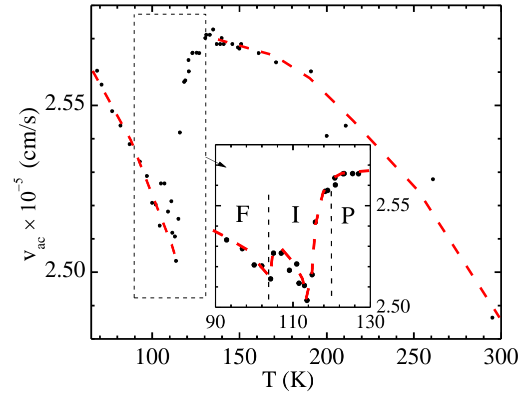

Fig. 4.9 The sound velocity thermal dependence measured using PAR with a prominent feature of P-I-F phase transitions indicated.

Fig. 4.9 displays the longitudinal acoustic velocity v_{ac} calculated from PAR reflection period (as in Fig. 4.2). The v_{ac} value increases slowly with decreasing temperature (dashed curve) and also undergoes pronounced dips in the prominent P-I-F crystal phase region between 120 - 107

K as shown in zoomed view in the inset of the Fig. 4.9. The similar v_{ac} dependence was reported by Ilisavski et al. [100] with only a small 2 % difference in absolute value. Acoustic velocity obtained by our PAR measurement also was confirmed in [100] GaAs ($v_{ac} = 4770$ m/s) which coincides well with literature [50].

We have shown that PAR technique by probe beam deflection is a sensitive tool due to high dn/dp value in $TlGaSe_2$. PAR signals are symmetrical and undistorted in wide excitation and spectral range. In $TlGaSe_2$ high PAR magnitude can be reached up to 70 %. Since PAR is proportional to absorption but does not depend on actual absorption location the sensitive spectral measurements can be performed.

4.3. Absorption anisotropy

In this chapter we show absorption spectra in nominally undoped $TlGaSe_2$ excited to the layer plane (***k*** || *c* excitation direction) obtained by conventional transmission measurements, FCA and PAR techniques. Low temperature *F*-phase absorption anisotropy revealed.

Optical absorption obtained by unpolarized light transmission in the direction normal to the layer plane (***k*** || *c*) is given in Fig. 4.10. The arrows

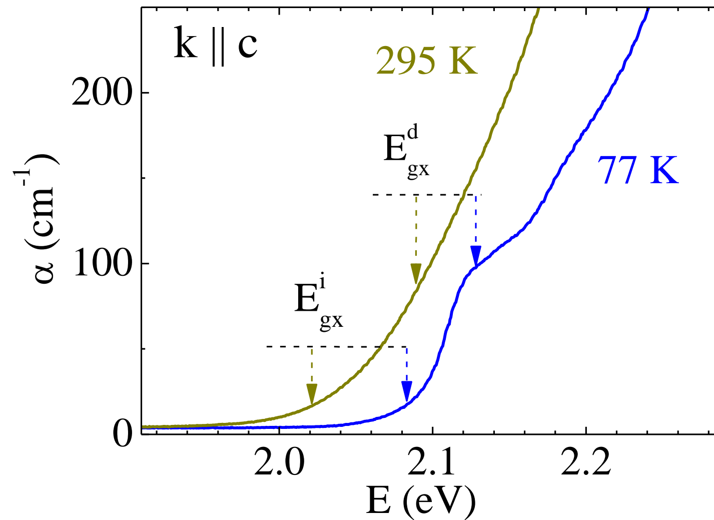

Fig. 4.10 Optical absorption spectra of undoped $TlGaSe_2$ crystal measured with unpolarized light directed normally to the layer planes at 295 and 77 K. Energies of the lowest indirect and direct excitons are indicated by arrows [A2].

show the positions of the lowest direct excitonic bandgap E_{gx}^{d} and the approximate threshold of the indirect excitonic bandgap E_{gx}^{i} exciton peaks at 295 and at 77 K. Energy positions were deduced by modeling of the direct and indirect absorption in $TlGaSe_2$ from data at 15 K [8].

One can see that the direct absorption is quite small compared to usual direct bandgap semiconductor crystals (where absorption coefficient is tens of thousands cm^{-1}). This peculiarity, like in a few other layered semiconductors, arises because direct optical transitions are nearly forbidden due to crystal symmetry. Damping effect is stronger in $TlGaSe_2$ comparing to $TlInS_2$ and $TlGaS_2$. Particularly strong forbidden role manifests for $E \perp c$ excitation direction [8, 13, 18]. Two lowest excitons have been deduced in $TlGaSe_2$ from modeling modelling of absorption at low temperatures, a direct exciton with the Rydberg energy of excitonic ground state of 23.5 meV and an indirect exciton with the large Rydberg energy of about 100 meV [8]. The Rydberg energy of indirect exciton is not defined exactly within the range 40 - 120 meV. Since *c*-axis is deviated by 10° angle from the normal direction, the

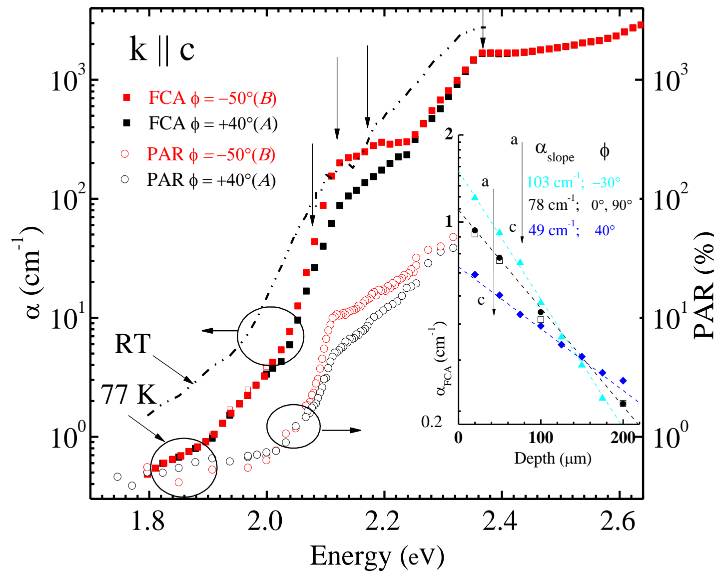

Fig. 4.11 The absorption spectra of $TlGaSe_2$ at RT (dash-dotted line) and at 77 K by FCA (solid symbols) and PAR (open symbols) for two light polarization angles on the *ab* plain (***k*** || *c*). Vertical arrows indicate critical energy points. The inset shows the depth distribution of FCA at three pump light polarization angles at 2.1 eV [A5].

obtained result testifies that $TlGaSe_2$ crystal is a bulk-like material with 3D semiconductor properties at room temperature.

At 77 K temperature after crystal transformation to *F*-phase the absorption spectra properties change. Fig. 4.11 compares the bandgap absorption spectra (FCA - solid symbols and PAR - open symbols) extracted in $TlGaSe_2$ under $\boldsymbol{k} \parallel c$ illumination at 77 K. We avoided keeping the sample between 90 - 200 K temperature due to possible dynamic change of topological disorder memory by the stacking fault or impurity rearrangement [43]. The band edge exhibits a slight shift to high energies due to expansion of the bandgap. The critical point energies are identified in Fig. 4.11 by vertical arrows as discussed below.

More significantly, the clear absorption anisotropy is observed in the region 2.06 - 2.26 eV. Both FCA and PAR methods (see squares and circles) demonstrate the same general features. The polarization diagram around exciton peak at $h\nu = 2.12$ eV is shown in the Fig. 4.12 for RT and 77 K. At room temperature no polarization dependence is observed. At 77 K the absorption maxima/minima occur on two nearly perpendicular directions *A* and *B*, with +40° and -50° polarization angle shift from the *a*-crystallographic direction, respectively.

The FCA depth-distribution at three polarization angles is exposed in the

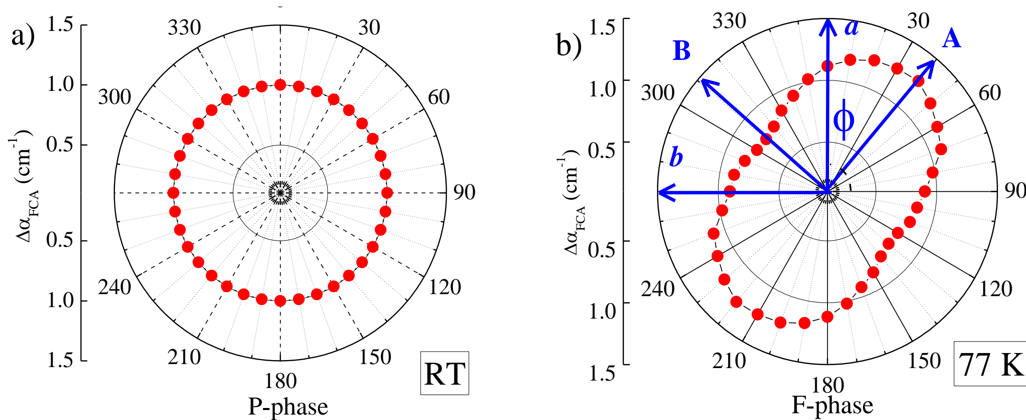

Fig. 4.12 The polarization dependences (a) at 2.12 eV at RT in *P*-phase and (b) at 77 K in *F*-phase. Directions *a*, *b* mark crystallographic directions, while *A* and *B* mark the maxima/minima of the absorption at 77 K [A5].

inset of Fig. 4.11. The higher absorption corresponds to steeper $\Delta\alpha$ exponential slope into the bulk on a semi-log scale. The same result was detected at various places of the sample and the same angular direction anisotropy for entire range 2.06 - 2.26 eV was detected. Hence the observed absorption feature is the bulk structure property of the material. This finding confirms that $TlGaSe_2$ structure loses quasi-uniaxial character and in the F-phase becomes optically biaxial on the *ab* plain.

To explain indirect absorption spectral shape the following fit with multiphonon absorption (Eq. (2.21)) was applied. Experimentally observed critical energies were applied in to the fit as indicated by arrows in Fig. 4.11, namely, the lowest indirect excitonic gap E_{gx1}^{i}=2.08 eV with binding energy of $E_{ex}^{i} = 100$ meV, the lowest Γ-direct band exciton peak E_{gx1}^{d}=2.117 eV, and the second indirect excitonic gap E_{gx2}^{i}=2.17 eV. In addition, the upper Γ-band at 2.37 eV is observed. The listed critical energies are in close agreement with reported data of unpolarized absorption spectra T < 20 K [8]. Absorption strength parameters were set A_1 = 1.6; A_2 = 16. The best fit was obtained including four main phonons. Their energies and relative amplitudes were evaluated from Raman lines [A3] (Fig. 4.15) which are listed in Table II.

Table II. Fitted phonon energies and strength element C^p.

Phonon	TA	LA	TO	LO
E_{ph} (meV)	2.5	11.5	16.6	24
C^p	5	1	3.5	2.6

The fit was performed on the spectrum for B direction and is shown in Fig. 4.13 (solid line) along with the original data (open circles). The terms in Eq. (2.21) representing transitions to exciton ground level $\sim(h\nu - E_{gx}^{i})^{0.5}$, and to the rest of continuum states $\sim(h\nu - E_{g}^{i})^{2}$ are shown by dashed lines. A similar result also can be found with one averaged assisted-phonon in Ref. [8].

The Fig. 4.14 shows that the subtrahend between the absorption fit and the experimental data of A and B direction spectra is quite similar (see dashed lines in Fig. 4.14). This fact imply that other spectra contributions, like the

impurity tailed fraction below 2.09 eV and the one above to the second indirect band (> 2.17 eV) are nearly unpolarized. The provided comparison indicates that the direct Γ-absorption band, as shown in Fig. 4.14 by solid line, becomes polarized on the *ab* plain. It is important to stress out that this component is completely dipole-prohibited in the *B* direction and allowed partially in the *A* direction. Its magnitude in *A* direction approximately doubles as extracted from unpolarized 15 K spectrum [8].

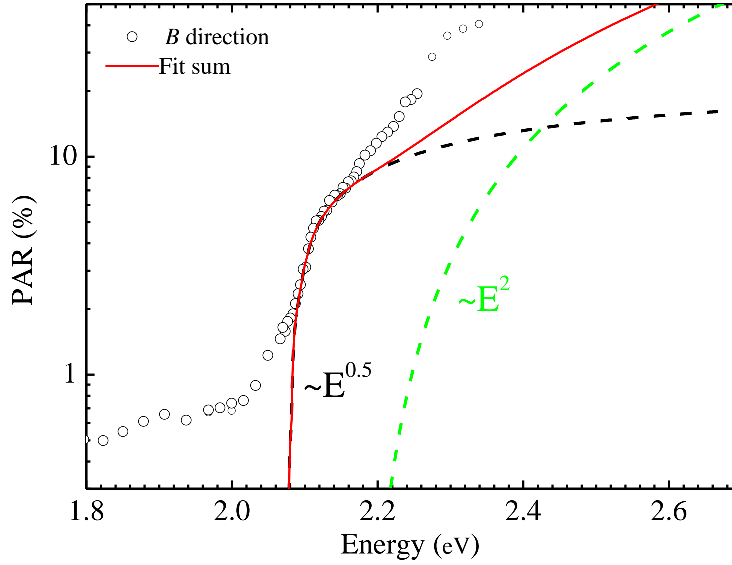

Fig. 4.13 Absorption spectra edge at *B* polarization (open circles). The red solid line is the best fit curve for the lowest indirect band according to Eq. (2.21); contribution of the first and the second term is indicated by dashed lines [A5].

The absorption shape calculation for Γ-point (direct exciton) in Fig. 4.14 was performed similarly as in Ref. [8] using the following parameters: E_{gx}^{d} = 2.117 eV, the direct bandgap E_{g}^{d} = 2.145 eV and exciton binding energy R_{ex}^{d} = 28 meV, with a broadening parameter Γ = 30 meV. A fit sufficiently well reproduces the experimental points. As a matter of fact, the oscillator strength of the exciton ground state had to be reduced by a factor of 100 in respect to the bandgap continuum (dotted line). Therefore, the presence of direct exciton in *A* direction could explain the absorption spectra anisotropy.

The shift of polarization angle in *ab* plain indicates a Tl^{+} slippage from *a* and *b* lines. A sketch of structure evolution around Ga_4Se_{10} cluster is shown for

a- and *b*-lines in the inset of Fig. 4.14. As predicted, this shift is a driving force to create the ferroelectricity [4, 36]. A double-well potential for Tl position was attested by calculation of the discrete Tl_2Se_9 molecular and the $TlSe_3$ 1D-chain model [4]. The Tl slippage renders stabilization in the structure since the asymmetric movement creates lone pair Tl^+ hybrids and reinforces Tl-Se bonding by changing the bond angle. This result is consistent with the interlayer distance reduction which is compensated by sudden enlargement of *a, b* basis [36].

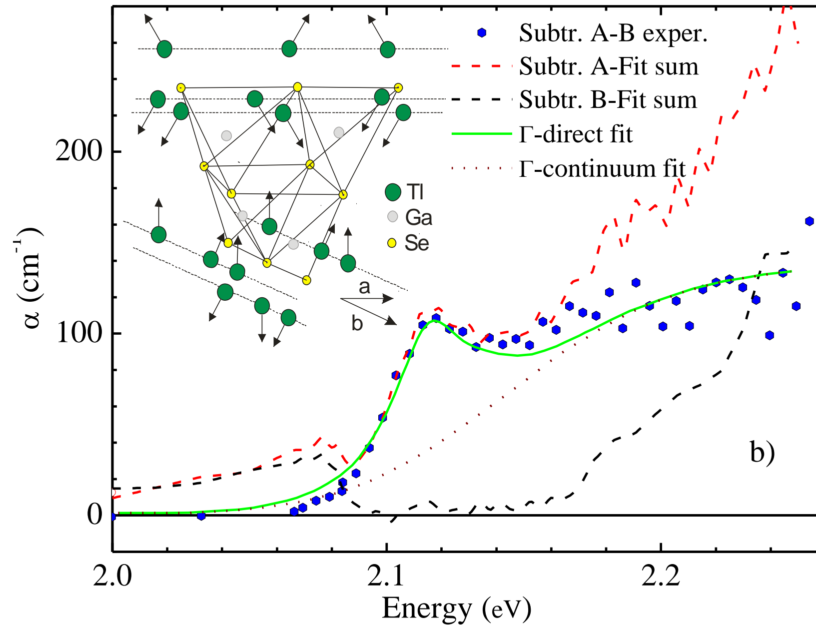

Fig. 4.14 Subtrahend of *A* and *B* spectra (circles) and direct exciton fit (solid line) with continuum states (dotted line). Dashed upper and lower curves are the shapes after subtraction of the fitted curve in Fig. 4.13 from *A* and *B* direction spectra obtained by PAR. (inset) Possible Tl atoms disposition in around the Ga_4Se_{10} cluster at *F*-phase in respect to *a* and *b* directions [A5].

Our result is also supported by asymmetric EPR resonance multiplication in the *F*-phase of $TlGaSe_2$ crystal when it was doped by Fe^{+3}. Since the Fe^{+3} replaces the Ga^{+3} position, a ligand can sense a field distortion angles on the Tl^+ ion [32] which is proved by angular dependences of EPR resonances. The current work implies that the intersection of two conduction band branches in the Brillouin zone at the Γ-point (Fig. 1.4) is removed by the Tl slippage and that only one branch creates oblique absorption in the *A* direction. A detailed

theoretical calculation of Tl and Se atoms bonding could further support this idea.

We have shown that in $TlGaSe_2$ on the layer plane at ***k*** || *c* excitation direction after transformation into *F*-phase absorption spectra becomes polarized while at room temperature in *P*-phase no polarization is observed. Spectral analysis showed that anisotropy could be explained by direct exciton absorption which is partly allowed in *A* direction. This suggests that Tl^+ ions slip from *a* and *b* crystallographic directions.

4.4. Photoluminescence and enhanced band edge absorption

We reveal the intrinsic band-to-band photoluminescence (PL) at RT in $TlGaSe_2$ and in isostructural $TlGaS_2$ by means of confocal spectroscopy. The band edge absorption spectra were determined at different excitation geometry by using techniques of depth-resolved FCA and PAR on laterally polished sample. Both ***k*** ⊥ *c* and ***k*** || *c* illumination directions were exploited at RT in *P*-phase and at 77 K in *F*-phase.

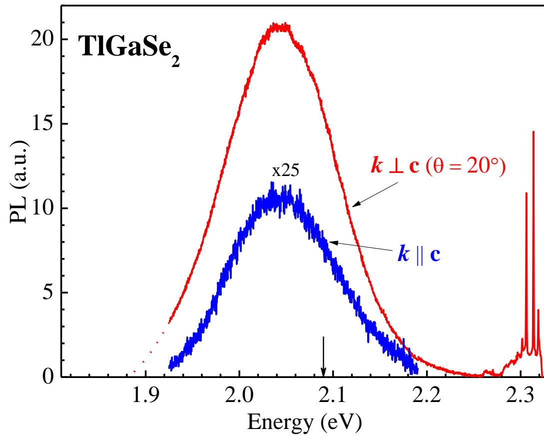

Fig. 4.15 Photoluminescence and Raman lines obtained from *ab* plane (blue) and from lateral surfaces (red) in undoped $TlGaSe_2$ ($h\nu_{exc}$ = 2.33 eV) [A3].

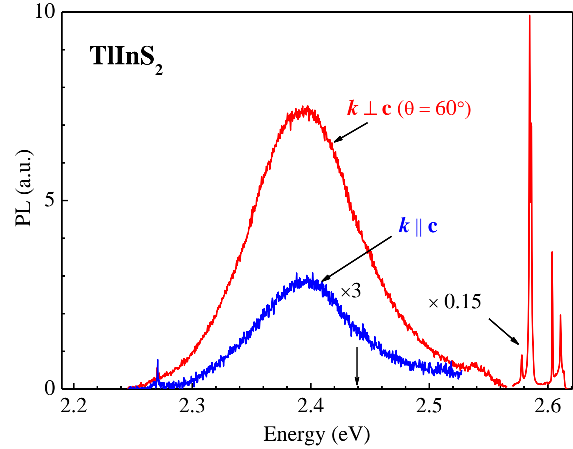

Fig. 4.16 Photoluminescence and Raman lines obtained from *ab* plane (blue) and from lateral surfaces (red) in $TlInS_2$ ($h\nu_{exc}$ = 2.62 eV) [A3].

The confocal PL was performed in the backscattering geometry with 532 nm, 473 nm with a spot diameter of ~200 nm and 60 μJ excitation. Here we investigated undoped $TlInS_2$ and nine $TlGaSe_2$ samples: five initially undoped

and four doped with Fe, Tb, B and Al by adding 0.1-0.5 % of the impurity to the melt.

Table III. The fit parameters of the Gaussian shape PL spectra.

Semiconductor	PL peak (eV)	FWHM (eV)
$TlGaSe_2$	2.042 ± 0.01	0.142 ± 0.04
$TlInS_2$	2.395	0.11

Two excitation geometries $\boldsymbol{k} \perp c$ (angle $\theta = 0^{\circ}$ corresponds to $E \perp c$ and $\theta = 90^{\circ}$ corresponds to $E \parallel c$) and $\boldsymbol{k} \parallel c$ (angle φ is always $E \perp c$ measurements in *ab* plane) (also see in Fig. 3.1) were exploited. Fig. 4.15 and Fig. 4.16 show PL spectra after excitation with polarized light of 2.33 eV in $TlGaSe_2$ and of 2.62 eV in $TlInS_2$. In Fig. 4.17 the corresponding PL dependencies on excitation beam polarization are shown. The intralayer optical phonon accompanied Raman lines were registered below these excitation energies which are virtually independent of the exciting light polarization.

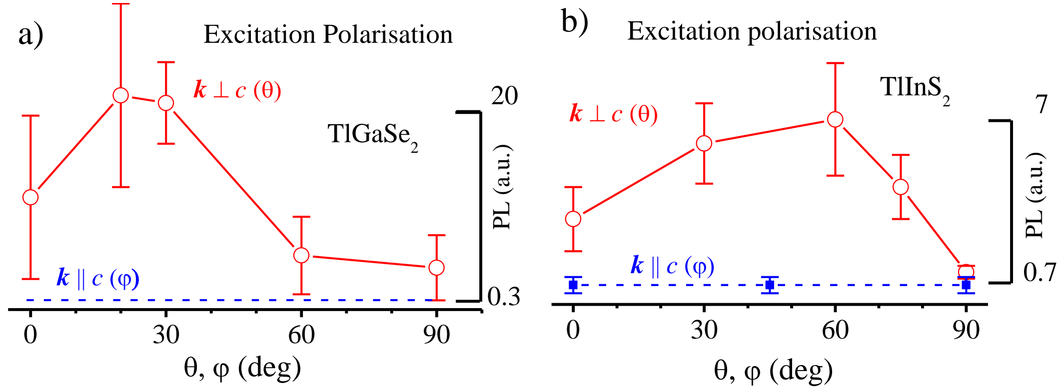

Fig. 4.17 Photoluminescence dependence on excitation pulse polarization angle for $\boldsymbol{k} \parallel c$ and $\boldsymbol{k} \parallel c$ excitation geometries in (a) $TlGaSe_2$ and b) $TlInS_2$ [A3].

The PL spectra appear as a wide Gaussian curves appearing below well-established the Γ-exciton energies [25][101]. Exciton positions are indicated by vertical arrows. The PL nearly linearly increases with the excitation power and is not detected for excitation quanta below the bandgap. These peculiarities are typical behavior for the intrinsic PL emission mechanism. The Gaussian fits of PL spectra are given in Table III. An error represents variation in different batches of $TlGaSe_2$ which implies some influence to the intrinsic PL

mechanism from a possible variation of the most common defect in layered crystals - the stacking faults.

For $\boldsymbol{k} \parallel c$ a weak PL peak is observed and, however, is independent of excitation polarization angle (φ) or a measurement position in both materials. Nevertheless $TlInS_2$ yields ~2.5 times stronger PL than $TlGaSe_2$ due to higher excitonic absorption. It is worth noting that the weak PL for $\boldsymbol{k} \parallel c$ in $TlGaSe_2$ was spotted only in undoped sample and no PL was observed for samples doped with Ag and Fe. This finding could be explained by overlapping of the band edge and the impurity absorption band.

For $\boldsymbol{k} \perp c$ the PL is substantially bigger and varies on measured spot position in the same sample as represented by error bars. Moreover, for $\boldsymbol{k} \perp c$ excitation direction the PL is strongly enhanced comparing to the PL obtained in $\boldsymbol{k} \parallel c$ excitation direction. The enhancement factor in $TlInS_2$ and in $TlGaSe_2$ is as much as 7 for $\theta \approx 60^{\circ}$ and ≥ 50 for $\theta \approx 20^{\circ}$, respectively.

The Fig. 4.18 shows PL emission light polarization obtained under 3.06 eV excitation. The sinusoidal dependence of the PL light approaches a maximum when $E \parallel c$. The obtained feature demonstrates that in $TlGaSe_2$ the PL emission is associated with out-of-plane oriented dipoles.

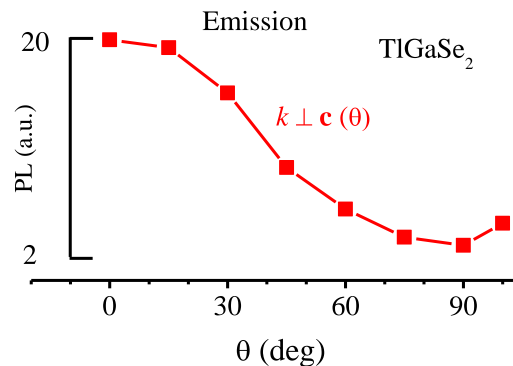

Fig. 4.18 Emitted PL intensity polarization dependence in $TlGaSe_2$ under 3.06 eV excitation [A3].

To account for these features, a combined study of light absorption peculiarities in $TlGaSe_2$ by FCA and PAR dynamic techniques has been carried out which data can be calibrated to the bulk absorption coefficient (as described in chapter 3.4.)

The absorption α_{bb} spectra in $TlGaSe_2$ for two illumination directions are presented in Fig. 4.19. In the case of perpendicular light incidence ($\boldsymbol{k} \parallel c$, $E \perp$

c), α_{bb} obtained from the FCA is shown by open circles, and almost coincide with the unpolarized spectrum obtained by conventional optical transmission (solid red line) [8]. No polarization dependence in this case was detected. For illumination through the lateral facet ($\boldsymbol{k} \perp c$), the enhanced absorption and to the large extent dependent on the light polarization absorption was found. The enhancement is detected in the large spectral area around the bandgap. For different energies the enhancement factor is different and can be estimated from Fig. 4.19. For excitation polarization $E \perp c$ the enhancement is**:** at 1.9 eV - 4 times, at 2.0 eV – 4 times and at 2.1 eV – 7 times. For $E \parallel c$ the enhancement is far bigger**:** at 1.9 eV - 8 times, at 2.0 eV – 47 times, at 2.1 eV - 100 times. Such enhancement is really surprising since it testifies that not only the Γ-direct absorption becomes allowed, as expected, but also the indirect and the sub-bandgap absorption must increase as well.

Furthermore, the FCA in-depth distribution results indicate that the enhanced absorption does not remain the same within the sample depth as

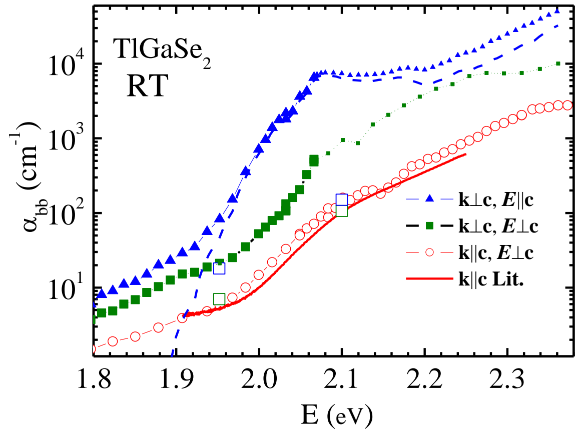

Fig. 4.19 Absorption spectra in $TlGaSe_2$ at different excitation geometry obtained from FCA - large symbol and PAR - small symbol. Open squares show α_{bb} obtained at $\boldsymbol{k} \perp c$ from the FCA slope in the in the bulk. The solid line - conventional measurement [8]. Direct absorption spectra given by dashed line was used for PL simulation [A3].

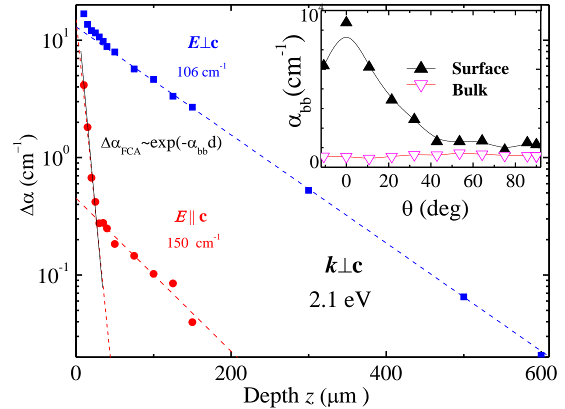

Fig. 4.20 The light induced depth-distribution of FCA at $\boldsymbol{k} \perp c$, extracted α_{bb} values are indicated. In the inset the polarization dependences of the absorption in the near-surface region and in the bulk at 2.1 eV [A3].

shown in Fig. 4.20 measured for $\boldsymbol{k} \perp c$ at 2.1 eV energy corresponding to Γ-exciton. In uniform case one would expect single exponential slope, however, we observe two regions with different slopes which are denoted as near-surface and bulk regions. For $E \parallel c$ the strong absorption reflected by steep slope of $\exp(-\alpha_{bb}z)$ which persist to about 40 μm at near-surface region. In this region ($z < 40$ μm) the α_{bb} obeys the dependence on polarization angle θ with a maximum at $\theta = 0^{\circ}$ (see the inset in Fig. 4.20, solid triangles). In the bulk region ($z > 40$ μm), the α_{bb} is substantially lower: for α_{bb} or $\boldsymbol{E} \perp c$ is 106 cm^{-1} and for $E \parallel c$ is 150 cm^{-1}.

The obtained bulk absorption values are very close to those measured for illumination normal to ab plane ($\boldsymbol{k} \parallel c$), as shown in Fig. 4.19 by large open squares. Moreover, the polarization dependence of α_{bb} in the bulk is almost negligible (see inset in Fig. 4.20, open triangles). Thus, we conclude that absorption enhancement is most probably caused by particular material property which exists in the near-surface region. We performed measurements in two polished $TlGaSe_2$ samples and estimated near surface region to be 40 – 100 μm of thickness from lateral side.

It seems likely that the variation in the size of near-surface region for broken lateral surface is larger than for polished one, as evidenced by large fluctuations of the intrinsic PL in Fig. 4.17. The near-surface region size of broken lateral surfaces is expected to be no less than a few micrometers.

Hence, we assume that during polishing (or breaking) the structural crumpling of the unit cell takes place all along the surface which leads to variations between the bonding angles of a corner connected M_4X_{10} polihedra units. That in its turn acts on a weak coupling of the buried interlayer Tl-X bonds (Fig. 1.2) and results in modification of the states at the extrema of the bands. The validation of slippage ability of Tl^{+} ion along *a-, b*-directions proven theoretically [4].

Usually PL in layered semiconductors is originating from DAP recombination and observed at low temperatures: in $TlGaSe_2$ at T < 2.2 K [44]

and up to 30 K [29]; in $TlInS_2$ at T < 100 K [45] when both materials are in *F*-phase. Recently a single report of the PL at RT in $TlGaSe_2$ was revealed with the peak at 630 nm (1.97 eV) and attributed to DAP emission [46]. One result published in the conference abstract in 2010 resembles PL caused by exciton emission at RT for $TlInS_2$, however the PL spectrum for $TlGaSe_2$ was mentioned but not exhibited [47]. Our PL spectra show that band-to-band transitions at RT are systematically enhanced for $\boldsymbol{k} \perp c$ excitation direction. Since the PL is weak it can be detected only by means of confocal spectroscopy in specific areas of surface. The present data implies that the PL in $TlGaSe_2$ (as well as in $TlInS_2$) can be explained by an enhancement of band-to-band absorption. This enhancement exists only in the subsurface region but is not a material bulk property under $\boldsymbol{k} \perp c$ light direction.

We have performed the PL spectra simulation in $TlGaSe_2$ using the direct band-to-band absorption from the spectrum obtained at $\boldsymbol{k} \perp c$, $E \parallel c$, shown in Fig. 4.19 by the dashed line. The ground state 2.095 eV Γ-exciton and the direct bandgap $E_g = 2.12$ eV, both broadened by 35 meV, were applied for the PL spectra simulation. We were able to reproduce the experimentally measured PL spectrum shape in the case of dipole-forbidden optical transition as well as for the dipole-allowed one. As a matter of fact, it was essential to reduce the oscillator strength of the dipole-allowed optical transitions from the ground state of the exciton by 100 times (similar reduction as in *F*-phase).

We have revealed photoluminescence at room temperature for the first time originating from band-to-band transition in $TlGaSe_2$ and $TlInS_2$. The PL observed by other authors at RT was originating from donor-acceptor pairs recombination. The PL was weak and yielded polarization dependence. Near surface region revealed 40 – 100 μm of thickness possessing enhanced absorption and pronounced polarization dependence compared to the bulk properties. The PL was explained by direct exciton recombination which oscillator strength was reduced 100 times.

4.5. $TlGaSe_2$ doped with Fe

Three $TlGaSe_2$ samples intentionally doped with Fe by adding 0.1, 0.5 and 3 % of molar ratio in respect to Ga constituent were investigated. Optical transmission was measured in cleaved 100 μm platelets in wide temperature range and recalculated to absorption coefficient.

Significant differences in the absorption of Fe doped samples appear at energies below the bandgap (Fig. 4.21). Two wide and overlapping absorption bands emerge at 1.6 and 1.9 eV with growing Fe content. Absorption of these peaks exceeds the detection limit in the 3% Fe sample. With the increasing temperature, the peaks show a noticeable thermal broadening and a slight shift to lower energies. Such behavior is characteristic to the free-to-bound optical transitions in semiconductors [102]. Similar Fe absorption band were also observed in $TlInS_2$ [103].

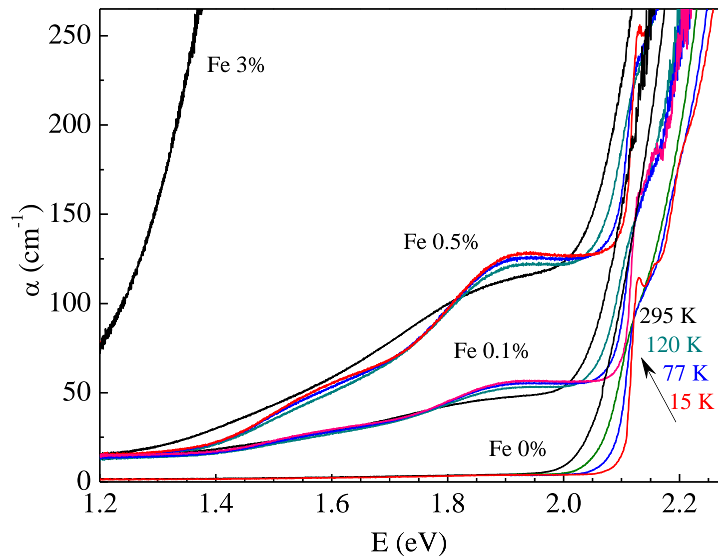

Fig. 4.21 Absorption spectra of $TlGaSe_2$ crystals doping with 0.1, 0.5 and 3 % of Fe as measured in 243, 154 and 122 μm thick samples, respectively at four indicated temperatures [A1]. Spectrum of undoped sample (Fe 0 %) is taken from Ref. [8].

Since $TlGaSe_2$ is *p*-type the spectral positions of Fe impurity absorption indicate that Fe energy levels must be in the upper part of the forbidden gap, i.e., Fe generates deep donor levels. Optical transitions then arise between the top of the valence band into the empty Fe states. To simulate optical transitions

we use the modified classical photo-deionization model. Absorption spectrum was composed of transitions form valence band to the empty three deep donor (DL1, DL2, DL3) levels using Lucovsky type model with structural disorder and the thermal broadening [A1]. At first it was applied for the sample with Fe = 0.1% and later extended for samples with Fe = 0.5% and 3%. A linear dependence of absorption versus Fe concentration was obtained in the temperature range 15 - 300 K. The parameters of energy positions at RT from the valence band have been deduced: E(DL1) = 1.26 eV, E(DL2) = 1.465 eV, E(DL3) = 1.725 eV [A1]. According to this dependence, value of Fe contamination of about 0.01% was determined in intentionally undoped $TlGaSe_2$ sample. From modeling we evaluate the electron-phonon coupling (the Huang-Rhys factor) as 3.93 which estimate average number of emitted phonons for impurity transition to the neutral state. The disorder energy broadening was set to 50 meV and 75 meV for DL3 and DL2 levels, respectively.

Fig. 4.22 shows the fundamental absorption edge of $TlGaSe_2$ samples at 15 K after the subtraction of the numerically simulated absorption of Fe impurities. The result shows that the doped $TlGaSe_2$ have essentially the same spectral shape of the residual absorption as the undoped $TlGaSe_2$. We simulated it using the contributions of the direct and indirect bandgap absorption components as indicated by the respectively labelled curves. The data fit curve (black line) represents the sum of these curves. The direct absorption consists of the broadened exciton peak at 2.128 eV and continuum band. The following indirect absorption consists of the multiple transitions into n = 1 ground exciton state. Here $E_{ex}^{i} = 2.094$ eV is the ground exciton energy and E_{ph} represents energy of a particular assisted phonon. Multiple phonons in the energy range 5 – 35 meV were reported by Raman scattering for $TlGaSe_2$ [104]. For the simulation we consider only the strongest 24 meV phonon. The exponential absorption tail below 2.09 eV can be attributed to unknown shallow impurity at 60 meV below the absorption edge.

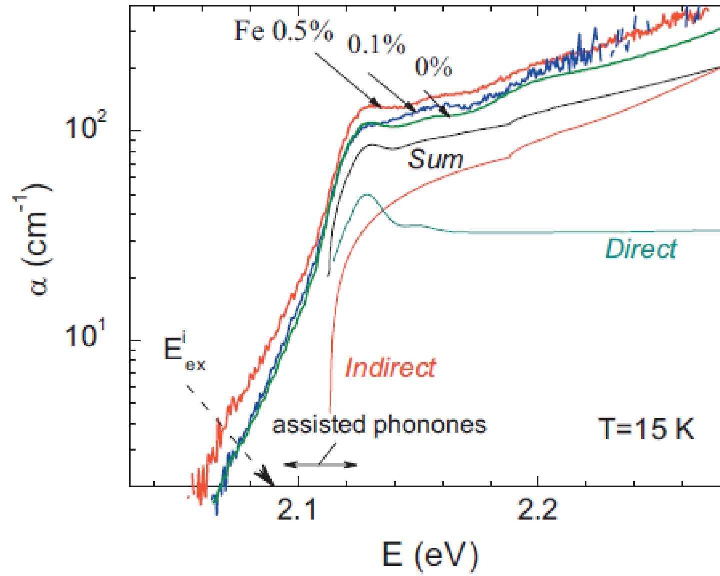

Fig. 4.22 Fundamental absorption edge of undoped and $TlGaSe_2$ samples with Fe = 0.1 and 0.5 % after subtraction of subband absorption at 15 K. Contribution of calculated Direct and Indirect (with assisted phonon 24 meV) and their sum (Sum) absorption is indicated. Horizontal arrow shows range of threshold spread for assisted phonon energies between 5 and 35 meV [A1].

The subband absorption spectra allow only relative estimation of the deep Fe level concentration. The particular density of donor levels cannot be determined from the absorption data alone since the oscillator strength constants are not calibrated. We only estimate upper concentration limit of the centers from the total concentration of atoms ($1.35 \cdot 10^{22}$ cm^{3}) existing in the $TlGaSe_2$ crystal. For 0.5% molar Fe/Ga ratio in the growing mixture of the melt we calculate that the incorporated Fe concentration cannot exceed $1.7 \cdot 10^{18}$ cm^{-3}.

The absorption spectra of a similar nature with 1 – 2% Fe admixtures were obtained by Gurbulak [103] for isostructural compound $TlInS_2$. Gurbulak found two strong free-to-bound absorption bands starting at 1.83 and 2.2 eV, whereas the band edge of $TlInS_2$ crystal is 2.6 eV. He also detected substantial background absorption of about 80 cm^{-1}. This result suggests that Fe creates similar subband absorbing centers in all ternary Tl compounds.

In EPR study [30, 32], $TlGaSe_2$ samples with Fe concentration of 2% were investigated. It was shown, that EPR spectra originate from four different

but structurally equivalent Fe^{+3} spin multiplets of d5 electron configuration. The EPR resonance lines showed splitting after passing through the PT region [32]. The similar results were observed in Fe doped $TlInS_2$ [30] and $TlGaS_2$ [105] crystals. Such results were interpreted as changing of the position of nearby Tl^+ ligand ions in respect to the Fe^{+3} ion in the $FeSe_4$ or FeS_4 tetrahedral units.

For Fe atom substitution of Ga one may expect certain influence on the bandgap states and fundamental absorption but the influence is minor (Fig. 4.22). Theoretical calculations show that neither the top of valence band at the Γ-point nor the indirect conduction band bottom is composed of Ga electron wave orbitals [9-11]. Only a relative small (about 21%) contribution of electron of Ga:4s is constituted the direct conduction band bottom at Γ-point [12]. So, Ga atom replacement by Fe atom also should give only a small change for the direct optical transitions. Insensitivity of the bandgap absorption in respect to Fe concentration (Fig. 4.22) confirms general indirect optical transition nature in $TlGaSe_2$ [8].

Recently, Gasanov et al. [34] investigated the above bandgap absorption in $TlGaSe_2$ with a molar ratio of Fe equal to 0 and 1 %. He observed above bandgap absorption enhancement by a factor of 3 in Fe = 1% sample and the shifting position of the direct band exciton peak. Note, that without subtraction we also observe enhancement in the above bandgap absorption by a factor of 2.3 for the sample with Fe concentration of 0.5% (Fig. 4.21). Subtraction of Fe related subband absorption, however, does not shift the exciton peak position and cannot explain the second feature of Ref. [34]. At this point, we have to note that variation of direct exciton position in undoped $TlGaSe_2$ was so far reported in the literature.

Three deep donor levels in $TlGaSe_2$:Fe related to Fe impurities are detected from impurity absorption spectra. The fundamental absorption edge structure of the $TlGaSe_2$ crystal remains almost unchanged at least to the doping level of Fe = 0.5 %. Also we show that Fe atom can change Ga in

$GaSe_4$ unit which agrees with EPR measurements and with theoretical calculation that Ga atom contribution to direct Γ-point absorption is small.

4.6. Carrier trapping and recombination

Here we have evaluated results obtained from carrier trapping and recombination study in high quality $TlGaSe_2$ crystals. Investigation was performed by depth-resolved FCA combined with measurement by photo-induced current transient spectroscopy (PICTS) [A2]. The FCA probing was obtained by 1.96 eV He-Ne light which reflect mainly on the majority holes [106]. The probe beam was focused and at the Brewster angle directed along the layers i.e., normal to excitation direction. The depth-resolution was about 7 μm.

The inset of Fig. 4.23 shows an example of induced excess free carriers (holes) transients $\Delta p(t)$ measured close to the excited surface (25 μm depth) at

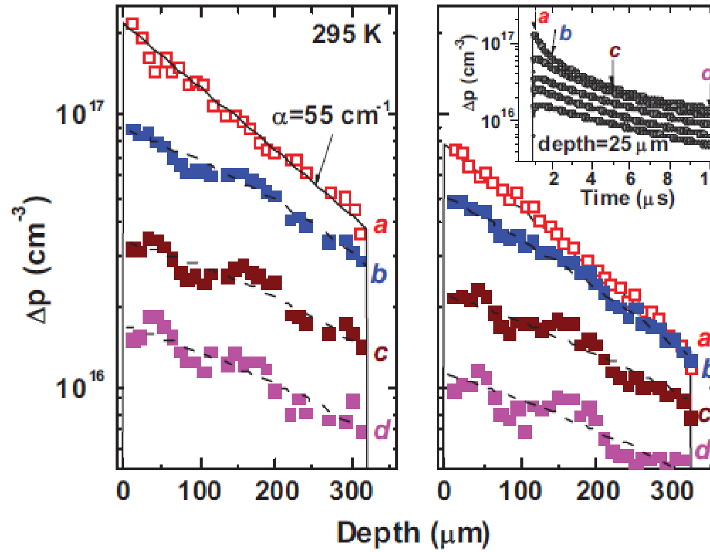

Fig. 4.23 Excess hole concentration $\Delta p(t, z)$ depth-distribution for two excitation fluencies at 295 K. Excitation photon energy was of 2.066 eV; the fluence was 3 mJ/cm^2 and 1 mJ/cm^2 for the left and right panes, respectively. The initial carrier distribution after excitation pulse follows exponential curve with the slope a = 55 cm^{-1} (solid line). The dashed curves are guides for an eye for Δp depth distribution at the elapsed times *b*, *c*, and *d*. In the inset an example of five $\Delta p(t)$ carrier transients at depth of 25 μm is shown where the elapsed times *a*, *b*, *c*, and *d* are indicated [A2].

four different excitation fluencies after termination of the pump pulse. The slope of the curve increases with pump intensity. To verify that such behavior of $\Delta p(t)$ is common to any point of the crystal the depth profiles of free carriers was measured at several excitation fluencies. Depth distribution for two different pump fluencies are shown in left and right panels of Fig. 4.23 at four elapsed times indicated a, b, c, and d as marked in the inset. On the right panel the pump intensity is reduced 3 times.

At time a the carrier depth distribution well described by equation $\Delta p(a,z) = \Delta p(a)epx(-\alpha z)$ according to absorption coefficient $\alpha = 55$ cm^{-1} which is in excellent agreement with a value determined in Fig. 4.10 from absorption spectrum ($\alpha = 59$ cm^{-1} at 2.066 eV). Similar in-depth slope match to absorption spectrum was obtained at 77 K (α = 60 cm^{-1} for excitation energy of 2.109 eV). Therefore, the excess hole concentration $\Delta p(a,z)$ just after excitation is determined only by generation slope of free carriers. It is neither suppressed nor enhanced by the other phenomena during the excitation pulse. The depth distributions of holes at later times are guided by dashed lines in Fig. 4.23.

As is clear from Fig. 4.23, significant faster reduction of hole concentration is observed at higher initial injection in whole sample depth. Nearly the same difference between $\Delta p(a,z)$and $\Delta p(b,z)$ is observed in the left and right panel for the same $\Delta p(a,z)$ values. This reveals that hole lifetime depends only on the injection level and is independent of the initial injection as well as the location of the measuring point in the crystal. However, some small lifetime variation can be observed in the Δp distribution plots. A slower reduction of $\Delta p(t,z)$ referred here to a longer than an average hole lifetime, which arises around the depth of 40, 160, and 280 μm. In contrast, a faster reduction of $\Delta p(t,z)$, referred to a shorter lifetime, can be noticed at 15 μm, 100 μm, and over a range of 200 – 270 μm.

We want to point out that no progressive changes in time of carrier concentration profile nearby front and back surfaces were observed. Such behavior is in notable contrast to a typical profile in a vicinity of bare surfaces

of crystalline SiC and Si [86] (see Fig. 6.3 for 4H-SiC with a diffusion coefficient $D = 3.5$ cm^2/s). The absence of this feature in $TlGaSe_2$ implies that across the layers the carrier diffusion coefficient D is small. We estimate D approximately from the limit of diffusion length $L = (D\tau)^{0.5}$ which must be less than the experimental resolution – a diameter of the probe beam. This suggests that the diffusion is lower than 0.05 cm^{2}s^{-1}. This finding is in agreement with high ratio of dark conductivity along and across the layers $\sigma_{||}^0/\sigma_{\perp}^0$ observed (Fig. 1.5) showing a restriction of carrier motion across the layer barriers [13].

The existence of minority carrier traps with a high capture cross section was detected by PICTS. The method analyses photocurrent decay after termination of long light pulse. Thermally stimulated carrier emission from traps at particular temperature induces transient current. PICTS signal for 100 s^{-1} rate window is shown in Fig. 4.24. Five analyzed peaks are indicated A1 - A5 and similar five peaks were observed in the samples obtained from other vendors, therefore A1-A5 must be regarded as set of carrier traps peculiar to $TlGaSe_2$.

The temperature displacement of the peaks positions for different rate

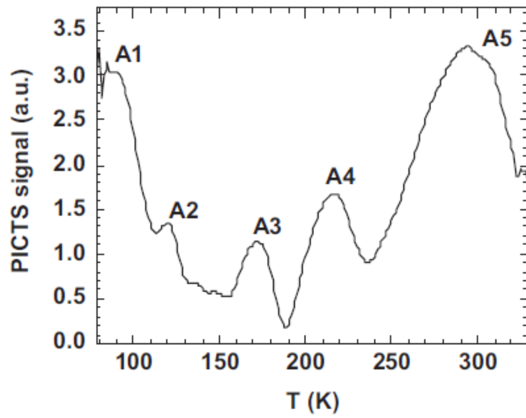

Fig. 4.24 PICTS spectrum for majority and minority carrier traps in $TlGaSe_2$. The rate window is 100 s^{-1}. To reduce noise the spectrum was smoothed by nine-point triangular smooth algorithm [A2].

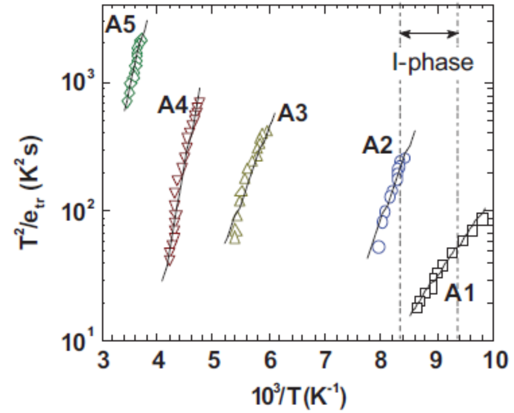

Fig. 4.25 Arrhenius plot of five trapping centers derived from PICTS temperature scans with various rate windows. The vertical lines denote a region of *I*-phase [A2].

windows enables to determine emission rate from each trap level. Corresponding Arrhenius plot is presented in Fig. 4.25 where slope reveals trap energy and the intercept shows capture cross section. Parameters are summarized in Table IV. The trap type was deduced indirectly by analyzing temperature dependence of the steady state photocurrent. With temperature increase the A1, A3 and A5 photoconductivity increases but in the range of A2 and A4 photoconductivity remains steady. Therefore we assign A1, A3, A5 to acceptors and A2 and A4 to donors (Table IV).

Table IV. Trap parameters in $TlGaSe_2$

trap	T (K)	E_t (eV)	σ (cm^2)	type	n_t (PICTS) comparative	N_t (cm^{-3})
A1	100-110	0.12	1×10^{-17}	acceptor	0.44	2×10^{15}
A2	120-130	0.23	4×10^{-14}	donor	0.19	5.3×10^{15}
A3	170-190	0.225	2×10^{-17}	acceptor	0.18	1×10^{15}
A4	210-240	0.45	1×10^{-13}	acceptor	0.27	7×10^{14}
A5	270-290	0.35	2×10^{-18}	donor	1	4×10^{15}

To clarify the injection-dependence behavior of excess free holes, we extracted instantaneous lifetimes from the successive tangent lines from concentration decays at different carrier concentrations. The data were smoothed by applying an adjacent point averaging algorithm and the results are presented in Fig. 4.26. At RT the lifetimes from various depths were collected in order to demonstrate the statistical lifetime dispersion. The statistical lifetime scattering is not a surprising fact owing to a large variation of lifetime in compound semiconductors. For example, in high quality epitaxially grown SiC the spatial dispersion of lifetime comes up to 20 – 40 % [86].

The instantaneous free excess holes lifetime versus their concentration presented in Fig. 4.26 is independent of the crystal depth in which lifetime was extracted. At low and intermediate injection regions the hole lifetime τ^* was fitted by a logistic function:

$$\tau^* = \frac{(\tau_{LL} - \tau_{HL})}{\left[1 + \left(\frac{\Delta p}{p^*}\right)^s\right]} + \tau_{HL}\,, \tag{4.1}$$

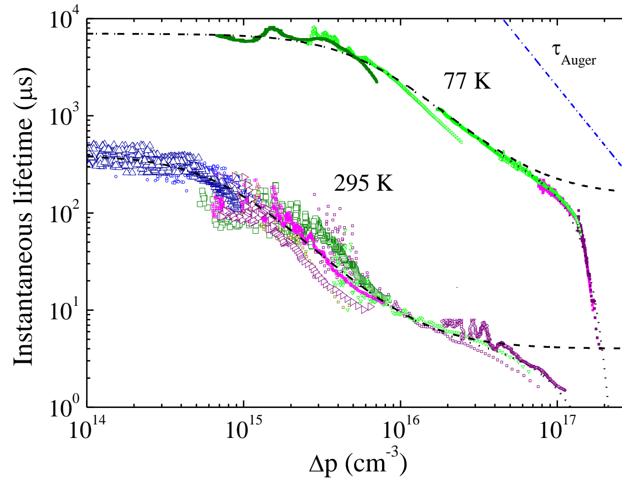

Fig. 4.26 Instantaneous excess free holes lifetime versus their concentration at 295 and 77 K. Each type of symbol represents the result obtained from a single $\Delta p(t)$ decay. Dashed black line is a logistic function described by Eq. (4.1). Dotted black line at high injection is an exponential cut-off function which is given by Eq. (4.2). The Auger lifetime τ_{Auger} is also plotted [A2].

where τ_{LL} is the lifetime at low level injection; τ_{HL} is the lifetime at intermediate level injection; p^* is hole concentration representing the curve center, Δp is the injected carrier density and s is a power factor.

The fit parameters are listed in Table V. Both τ_{LL} and τ_{HL} increase 20 times at 77 K temperature compared to RT. The transition betweenτ_{LL} and τ_{HL} occurs at a characteristic injection level corresponding to the hole concentration defined by parameter p^*. The p^* values are of orders higher than the equilibrium hole concentration p_0 and shift in the opposite direction with decreasing temperature (Table V). This indicates that mechanism of the observed p^* changes cannot be attributed to the concentration variations of equilibrium holes. Note that under a standard SRH recombination model the lifetime injection dependence is explained by the transition from minority carrier recombination regime, $\Delta p/p_0 \ll 1$, to ambipolar regime, $\Delta p/p_0 \gg 1$ [86]. In our case a plateau at low injection region (τ_{LL}) may be attributed to a fast excess minority carrier (electrons) trapping and, therefore, prohibiting to participate in recombination process. The existence of minority traps with high absorption cross section is detected by PICTS. When such traps become

saturated at higher injection level, hole lifetime achieves τ_{HL} value. For this reason parameter p^* represents the injection level necessary for filling the available minority traps at particular temperature so is equal to general number of traps N_t obtained by FCA which are summarized in Table IV.

Table V. Fitting parameters.

T (K)	p_0 (cm^{-3})	τ_{LL} (s)	τ_{HL} (s)	p^*(cm^{-3})	s	p^{**}(cm^{-3})	k	γ (cm^{6}s^{-1})
295	1.5×10^{13}	4×10^{-4}	4×10^{-6}	7×10^{14}	1.6	1×10^{17}	1.8	
77	$\leq 10^{10}$	7×10^{-3}	1.3×10^{-4}	6×10^{15}	1.6	1.35×10^{17}	3.5	5×10^{-32}

The extracted carrier concentrations were used to extract trap concentration N_t. First consider the effect of minority carrier trapping at A2 and A4 centers. Since it is compensated semiconductor donor and acceptors must be in equal amounts. At 77 K the possibility for electron to escape from both traps is restricted by very low trap-escape time ratio, then trap concentration equals to both donor traps. At RT only deeper A4 trap is filled. This allows assuming that concentration of A4 trap is equal to $p^* = 7 \times 10^{14}$ cm^3 and the total concentration of both donor traps comes out to $p^{**} = 6 \times 10^{15}$ cm^{-3}. Other traps were calculated proportionally to n_t.

One can note in Fig. 4.26 a drastic decrease of carrier lifetime for the injection level above 10^{17} cm^{-3}. The character of lifetime reduction is incompatible with Auger lifetime τ_{Auger} dependence as in. Eq. (2.11) which is shown by dashed-dotted line in Fig. 4.26 for γ value expected for Auger process (see Table V). Extra high recombination at high injection level can be closely fitted by including an exponential cut-off multiplier:

$$\frac{1}{\tau^{**}} = \left[\frac{1}{\tau^*} + \gamma \Delta p^2\right] \cdot \exp\left(\frac{\Delta p}{p^{**}}\right)^k, \quad (4.2)$$

where the second term in the brackets represents the Auger recombination for $\Delta p = \Delta n$, p^{**} is corresponding injection level, k is power factor.

It is likely that the observed sharp lifetime reduction is caused by enhancement of carrier diffusion across stacked layers in $TlGaSe_2$ crystal. Under a restrictive diffusivity even a small change in probability of jumping or tunneling across the stacked layers can enhance electron access to holes and

provide acceleration of recombination process. It is possible that the excess electrons and holes after thermalization in the bands are situated on an opposite stacked layers of the compositional stacking faults thus are spatially separated. Moreover, carriers of opposite charges can be separated by potential barriers generated by stacking faults.

We have evaluated by PICTS technique trap levels of energy 0.23 - 0.45 eV from conduction band with high electron capture cross-sections with total concentration of traps about 6×10^{15} cm^3. These traps sufficiently enhance majority hole lifetime at low level of injection and can be saturated for sufficient injection under bipolar injection conditions. We attributed these traps to the existing stacking faults in $TlGaSe_2$.

The low carrier diffusivity across stacking layer planes was reflected by the absence of diffusion-related recombination near $TlGaSe_2$ surfaces. We discovered carrier lifetime reduction at high intensities which cannot be explained by Auger recombination. The sharp lifetime reduction at hole concentration above 10^{17} cm^{-3} was attributed to diffusion enhancement which increases access of electrons to holes and recombination becomes faster. The existence of such behavior implies that generated excess holes and electrons are spatially separated, e.g., separated by stacking faults.

4.7. Summary

We have applied a *Schlieren* optical probe method for the detection of PA waves in $TlGaSe_2$. High sensitivity is obtained due to high dn/dp value. PAR exhibits symmetrical shape and linear magnitude growth up to ~ 30 mJ/cm^2 of excitation fluence reaching high magnitude of ~70 %. PAR is independent of actual absorption spot and can be observed from the subbandgap excitation spectral range from 1.7 eV (at $\alpha \sim 1$ cm^{-1}) into the above bandgap range until 2.7 eV (at $\alpha > 5 \times 10^3$ cm^{-1}) therefore is applicable for sensitive absorption edge measurements in $TlGaSe_2$ and for applications in optical switching.

The bandgap absorption in the F-phase (at 77 K) at $\boldsymbol{k} \parallel c$ excitation direction shows optically biaxial character with a light polarization appearing

in the layer plain while at room temperature at *P*-phase there is no polarization dependence in the layer plain. The low temperature anisotropy could be explained by direct exciton absorption which is partly allowed in *A* and prohibit in *B* directions which are nearly perpendicular but shifted from crystallographic *a* and *b* directions. This suggests that Tl^{+} ions slip from *a* and *b* crystallographic directions and form nonequivalent Tl^{+} rearrangement.

We revealed photo luminescence at RT in $TlGaSe_2$ and in isostructural $TlInS_2$ most likely originating from band-to-band transitions with Γ exciton of low oscillator strength and with its polarization normal to layer plain. The PL signal yielded polarization dependence and at $\boldsymbol{k} \perp c$ excitation direction (cleaved surface) was weak and even weaker in $\boldsymbol{k} \parallel c$ direction (polished lateral surface). This feature is explained by the specific crystal places on the edges and by existence of near surface region (40 – 100 μm) with modified properties. By the surface the absorption is enhanced and has substantial dependence on polarization while in the bulk the polarization dependence is negligible. This finding let us to conclude that enhanced absorption occurs in the surface region which, in turn, increases injected carrier density and makes photoluminescence possible. The near-surface behavior, different from the bulk, might implement useful photonic functionality at RT.

Three deep donor levels in $TlGaSe_2$:Fe related to Fe impurity are detected from impurity absorption spectra. The fundamental absorption edge structure of the $TlGaSe_2$ crystal remains almost unchanged at least to the doping level of Fe = 0.5 %. This result agrees with theoretical calculations, which show small Ga (and Fe replacing Ga) contribution to the direct conduction band bottom states formation at Γ-point.

By PICTS technique trap levels were determined of energy 0.23 - 0.45 eV from conduction band of huge electron capture cross-sections and with a total trap concentration of about $6 \cdot 10^{15}$ cm^{3}. Experiments also demonstrated hole traps. Electron traps sufficiently enhance majority hole lifetime at low level of injection and can be saturated for sufficient injection under bipolar injection conditions which we attribute to the existing stacking faults in $TlGaSe_2$.

By depth-resolved FCA method the injection dependence of majority carrier (hole) lifetime in undoped $TlGaSe_2$ crystal were determined. The low carrier diffusivity across stacking layer planes is reflected by the absence of diffusion-related recombination near $TlGaSe_2$ surfaces. We discovered sharp carrier lifetime reduction above 10^{17} cm^{-3} hole concentration which cannot be explained by Auger recombination and is attributed to diffusion hop which can increase holes access to electrons and recombination becomes much faster. The existence of such behavior implies that generated excess holes and electrons are spatially separated, e.g., separated by layers or stacking faults.

To sum everything up, two independent results the RT PL and the 77 K exciton absorption spectrum could be explained by direct exciton absorption with oscillator strength reduced by 100 times. PL and absorption show polarization dependence which combined with lifetime reduction at high intensity suggests that excited *e-h* pair should be localized on a different layer plain in order to obtain the radiation.

5. Fluorescing 6H-SiC

We investigated highly co-doped B-N 6H-SiC epilayers and characterized optical properties to study basic requirements for light emission. The main goal of the current chapter is to elucidate the findings for nonequilibrium carrier recombination and transport in heavily B-N co-doped 6H-SiC. Luminescence spectra were obtained at high excitation level. In-depth FCA measurements yielded extremely low diffusion coefficients and long carrier lifetimes. Picosecond lifetime measurements were performed by transient grating in various injection dependencies. PL and lifetime dependence on temperature investigation allowed determining recombination mechanism and obtain activation energies of recombination centers.

5.1. Experimental approach

Thick epilayers of 6H-SiC were grown by the fast sublimation growth process (FSGP) on 2 inch 6H-SiC (0001) substrates with off-orientation angle 1.40º toward $[11\bar{2}0]$ direction [107]. The distance between source and substrate was adjusted to be about 1 mm at T = 1750 °C. As a source of N and B atoms were polycrystalline SiC plates with enhanced B and N density [108]. Additionally, N incorporation was enhanced due to growth in N gas ambient at different pressures. Samples denoted as ELS were grown in Linkoping University Sweden and RF samples were grown in the Meyo University in Japan. The SiC epilayers first were characterized regarding to the polytype and to structural quality by SEM and TEM optical measurement [B3] which showed that epitaxial relation is very good, i.e., interface could not be observed even in several samples. Moreover, any effects from step-bunching at the interface, a common feature of off-axis grown layers, could not be observed even when using lower-off-axis substrate. This result indicates a perfect epitaxial growth by the FSGP without the formation of dislocations. Raman scattering also showed that N-B co-doping does not degrade the quality of crystal structure up to the doping of 10^{19} cm^{-3} [B6].

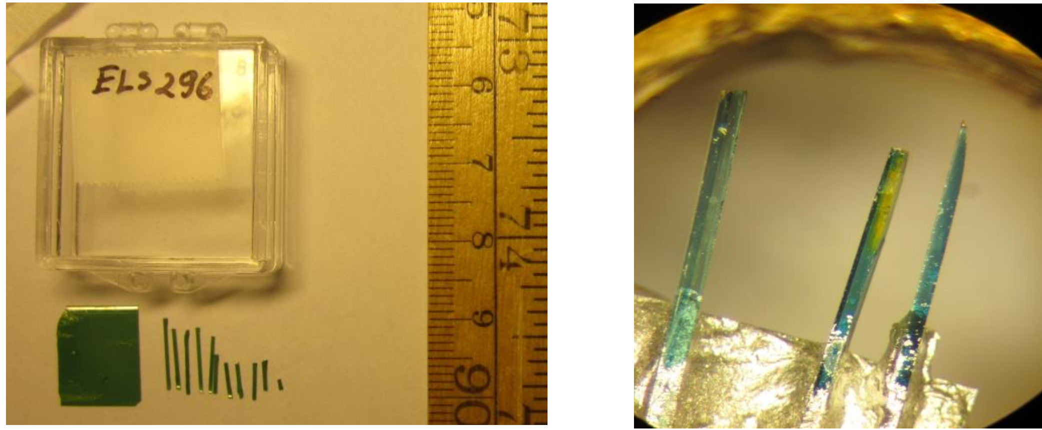

Fig. 5.1 (left) 6H-SiC 6H-SiC wafer with cut stripes along the ruler. (right) Few polished lateral side stripes attached to the holder with silver paste for probe beam penetration.

Dopants concentration was measured with secondary ion mass spectrometry (SIMS). Epilayers parameters are given in the Table VI. Except to the sample ELS 297, which had a rather low boron concentration (4×10^{16} cm^{-3}), B varied from 2.2×10^{18} cm^{-3} to 5.2×10^{18} cm^{-3} and the N varied from 4×10^{18} cm^{-3} to 1.3×10^{19} cm^{-3}. The backside of each sample was polished to allow beam transmission for absorption measurements. Few samples were cut into strips of 5-7 mm of length with width of ≈(200 × 500) μm^2 (Fig. 5.1). Then both lateral edges were carefully polished to optical quality to allow depth-resolved free carrier absorption optical measurements utilizing orthogonal pump-probe set-up with ns pulse duration (shown in Fig. 3.1 and Fig. 3.2). Also the picosecond pulse using TG technique and the depth-

Table VI The parameters of epilayers: doping N, B (SIMS); defects: *(a) carbon inclusions; *(b) polycrystalline inclusions; Some other extracted parameters are show which will be later referred in the text.

Sample No.	Thick-ness (μm)	N (cm^{-3})	B (cm^{-3})	$N_D - N_A$ (cm^{-3})	Comparative PL intensity	Defects (cm^{-2})
ELS 111	60	4.0×10^{18}	8.0×10^{18}	-4.0×10^{18}	0.0 %	
ELS 115	50	3.2×10^{18}	6.9×10^{18}	-3.7×10^{18}	6.6 %	
ELS 116	45	6.0×10^{18}	6.9×10^{18}	-0.9×10^{18}	8.3 %	
ELS 117	45	9.0×10^{18}	4.4×10^{18}	4.6×10^{18}	100.0 %	-
ELS 118	45	9.2×0^{18}	5.2×10^{18}	4.0×10^{18}	77.1 %	-
ELS 296	200	1.3×10^{19}	2.1×10^{18}	$\sim1.1 \times 10^{19}$		10^{1} *(a)
ELS 297	200	1.1×10^{19}	4.0×10^{16}	$\sim1.1 \times 10^{19}$		10^{6} *(a)
RF 18	130	4×10^{18}	2.5×10^{18}	1.5×10^{18}		10^{1}-10^{2} *(b)
RF 04	110	8×10^{18}	2.2×10^{18}	5.8×10^{18}		10^{5} *(b)

integrated FCA measurements were applied at the collinear pump-probe excitation geometry (at ***k*** || *c*) [109].

5.2. Photoluminescence vs carrier lifetime

Room temperature continuous wave luminescence was measured in five samples from ELS111 to ELS118 (see Table VI) with laser diode operating at λ = 377 nm as shown in Fig. 5.2. The integrated PL peak intensities were normalized to the strongest luminescing sample ELS117 (Table VI). The calibration of the internal quantum efficiency (IQE) for this sample was obtained under a close sphere optical measurement and yielded 7 % of IQE. The difference between donor and acceptor concentration $N_D - N_A$ is also shown in Table VI where negative and positive signs means *p*-type and *n*-type conductivity, respectively. In the highest *p*-type sample ELS111 no PL was registered. With decreasing *p*-type conductivity at ELS115 and ELS116 we observed small increase of PL. When the sample turns *n*-type, the PL increases dramatically. The strongest DAP observed in ELS117 sample with the largest $N_D - N_A$ concentration difference. Clearly there is a trend that PL increases with higher nitrogen concentration overwhelming boron concentration.

The average lifetime values were extracted from induced free carrier absorption decays at ***k*** || *c* excitation direction as shown in Fig. 5.3. Thin lines

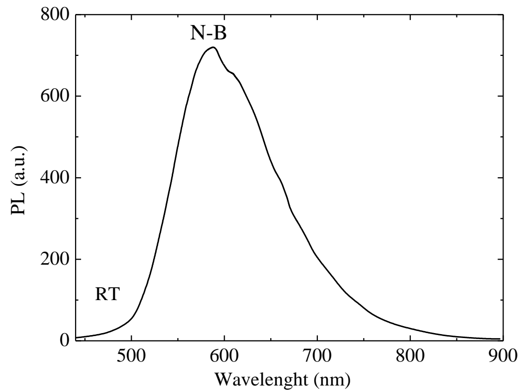

Fig. 5.2 Room temperature photo-luminescence in a fluorescent SiC [B3].

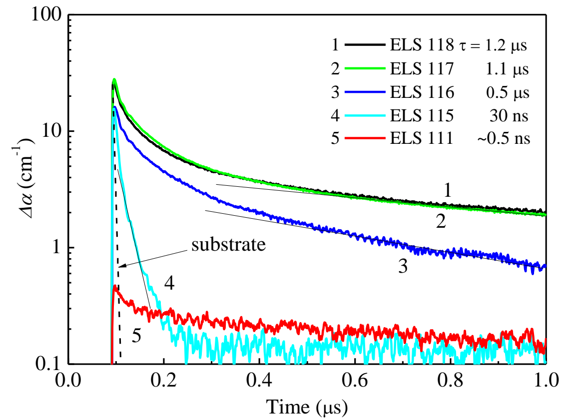

Fig. 5.3 Induced FCA transients in different doping fluorescent 6H-SiC epitaxial layers at constant excitation at ***k*** || *c*. [B3].

represent the exponential lifetime fit at moderate injection conditions where decay nonlinearity is not strong. It is exaggerating the fact that a longer electron lifetime is responsible for stronger emission and *n*-type doping should prevail over the *p*-type doping in the active layer of 6H-SiC. Samples ELS118 and ELS117 with the highest N concentration and the highest $N_D - N_A$ difference showed microsecond carrier lifetime. With decreasing $N_D - N_A$ difference the lifetime decreased and in ELS116 it became 500 ns and even less in ELS115 - 30 ns. In ELS111 sample with the highest B concentration lifetime was even shorter than the laser pulse duration which resulted in drop of FCA amplitude.

We found a correlation between PL emission, carrier lifetime and sample doping type. The stronger the PL is the longer carrier lifetime manifests. Since the PL is mainly caused by DAP recombination the long carrier lifetime means longer reemission from donor or acceptor states which in turn enhances radiative recombination probability (later by carrier decay analysis it is attributed to reemission time from deep boron state and is denoted as τ_2). Clearly the PL intensity is increasing from *p*- to the *n*- type samples; therefore, the further investigation was going to be focused mainly on the *n*-type samples.

5.3. Absorption depth distribution

The usual continuous absorption at $\boldsymbol{k} \parallel c$ was obtained from transmission measurements on samples with polished substrate as shown in Fig. 5.4. All *n*-type epilayers exhibit two broad absorption bands at 1.98 eV and 2.8 eV below the bandgap (~3.0 eV). The same bands are observed in *n*-type substrate with N doping ~10^{18} cm^{-3}. These bands are related to well-known vertical electron optical transitions into two upper conduction band branches. A broad absorption increasing towards the infrared region (below 1.0 eV) is caused by the phonon-assisted FCA. The absorption in different epilayers tends to increase with increasing donor concentration over acceptor concentration (N_D - N_A) according to SIMS data (Table VI). At the peak energy (1.98 eV) a small

deviation from this tendency is observed. Still the behavior of FCA implies that free electron concentration is determined by the N_D - N_A.

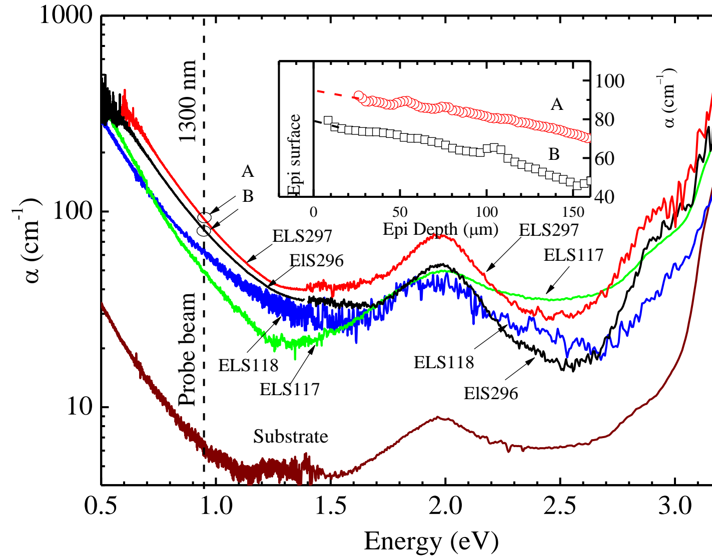

Fig. 5.4. Absorption spectra of different co-doped samples and a substrate. Dashed vertical line marks probe laser energy at 1300 nm. A and B points mark the thickness-averaged absorption in ELS297 and ELS296, respectively, while in the inset the absorption coefficient depth-distribution for these samples is shown [B6].

In the inset of Fig. 5.4 the absorption is shown as measured via the lateral polished crosscut side of the epilayer (in ELS297 and ELS296 strips by using 1300 nm (0.96 eV) probe beam at the same polarization). Obtained absorption is in good agreement with depth-integrated absorption value as marked by points A and B on a vertical dashed line. Moreover, we observe the higher absorption on the top of the epilayer which decreases gradually by 20 - 30 % towards the substrate. This trend indicates either some nonhomogeneous doping or/and some compensation ratio change of nitrogen vs boron during the epilayer growth process.

Fig. 5.5 shows the induced FCA depth-distribution for ELS296 and RF18 samples at different time lapse t after the laser pulse excitation in orthogonal pump-probe configuration (see chapter 3.1) where pump was 355 nm and the probe was 1300 nm. The initial FCA in-depth profile is exponential and the slope represents band-to-band absorption coefficient (α_{bb}) value. The obtained

value from the slope is α_{bb} = 900 cm^{-1} as shown with dashed line. It is very close to the value of 1000 cm^{-1} reported for undoped 6H-SiC at the same 355 nm excitation wavelength [58]. This difference indicates that the bandgap absorption is a little bit affected by high co-doping or some part of carriers may recombine within pulse duration scale (< 10ns).

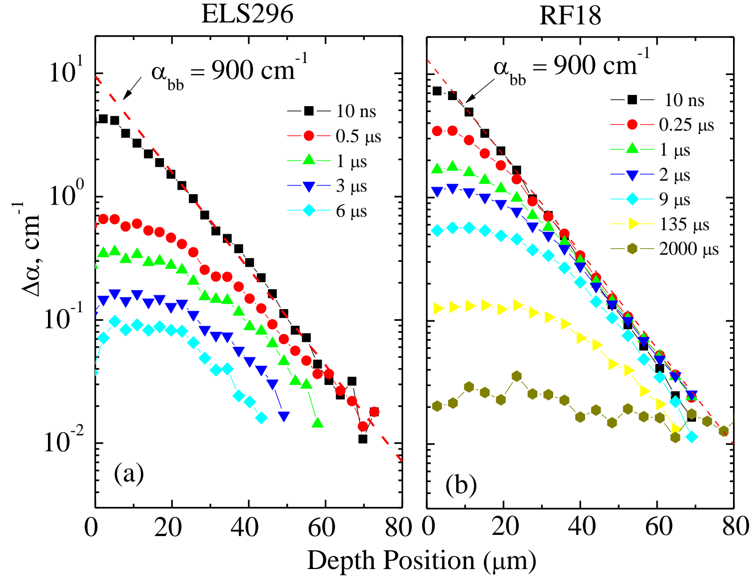

Fig. 5.5 Free carrier absorption $\Delta\alpha(t)$ depth-distributions of in ELS296 and RF18 samples at different time lapse after exciting laser pulse excitation [B5].

At the later μs-long time-lapse the FCA profiles decrease gradually maintaining profile shape as gained just after initial surface recombination process. We may conclude that the diffusion driven surface recombination on the excited surface remains small (S < 10 cm/s) or almost negligible because no carrier gradient arises towards the surface as seen at later elapsed times for both samples. This can be caused by low carrier diffusion. These findings are in contrast to undoped 6H-SiC ambipolar carrier diffusion phenomenon observed in [58].

5.4. Carrier decay analysis

The decay of photo-excited carriers is sometimes not a single exponential curve but has a slow component in the later part of the curve. When the excess electron-hole pairs are created by illumination, the excited holes are captured

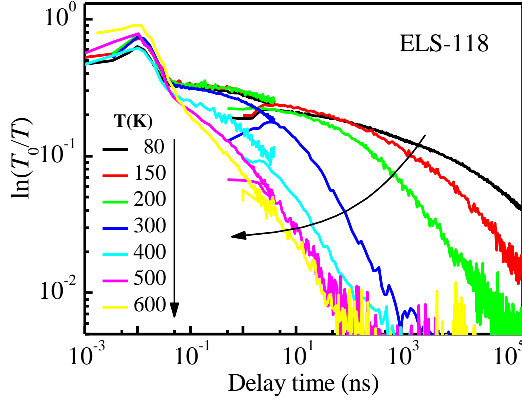

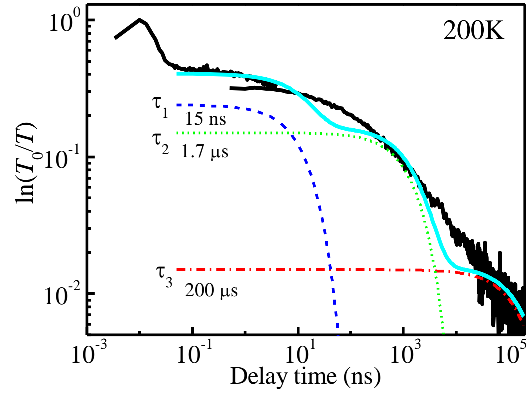

Fig. 5.6 FCA signal as a function of delay time at different T. An overlapping of delay lines was done at t = 4 ns. T dependant part can be viewed [B7].

Fig. 5.7 Fitting of three independent exponents τ_1, τ_2, τ_3 to the experimental data at 200 K [B7].

by the charged traps. Electrons are not captured completely and remain in the conduction band. Consequently, the decay of excess majority carriers has a long time constant. The slow decay rate reflects the reemission processes of holes from the traps and we may deduce some trap properties from the temperature dependence of the decay component.

The investigation of FCA transients ($\ln(T_0/T) = \Delta\alpha d$) temperature dependences in an ELS118 has been performed in the collinear FCA measurement geometry with 8 ps pulses from Nd^{3+}: YLF laser (351 nm) [B7]. It allowed distinguishing three main recombination paths which are strongly dependent on temperature. There is also a very fast component (t < 0.04 ns) which is independent on temperature but not analyzed here. In Fig. 5.6 the temperature dependent FCA signal on log-log scale is shown. The maxima are artificially set at 10 ps. Clear temperature dependence of slow parts is observed which also can be divided into three exponential processes in Fig. 5.7 and denoted as τ_1, τ_2 and τ_3 (also shown in Table VII below). All of them can be treated independently because the time constants are separated by an order or more.

From Fig. 5.8(a) and (b) we find two faster components τ_1 and τ_2 which have a strong T-deactivated relaxation time but their amplitudes weakly

depend on temperature. While τ_3 exhibits opposite behavior: reemission time is T-independent but the amplitude is strongly thermally activated. For two fast components τ_1 and τ_2 the Arrhenius plots showed activation energies of 200 ± 30 meV and 500 ± 120 meV, respectively (Fig. 5.8 (a)).

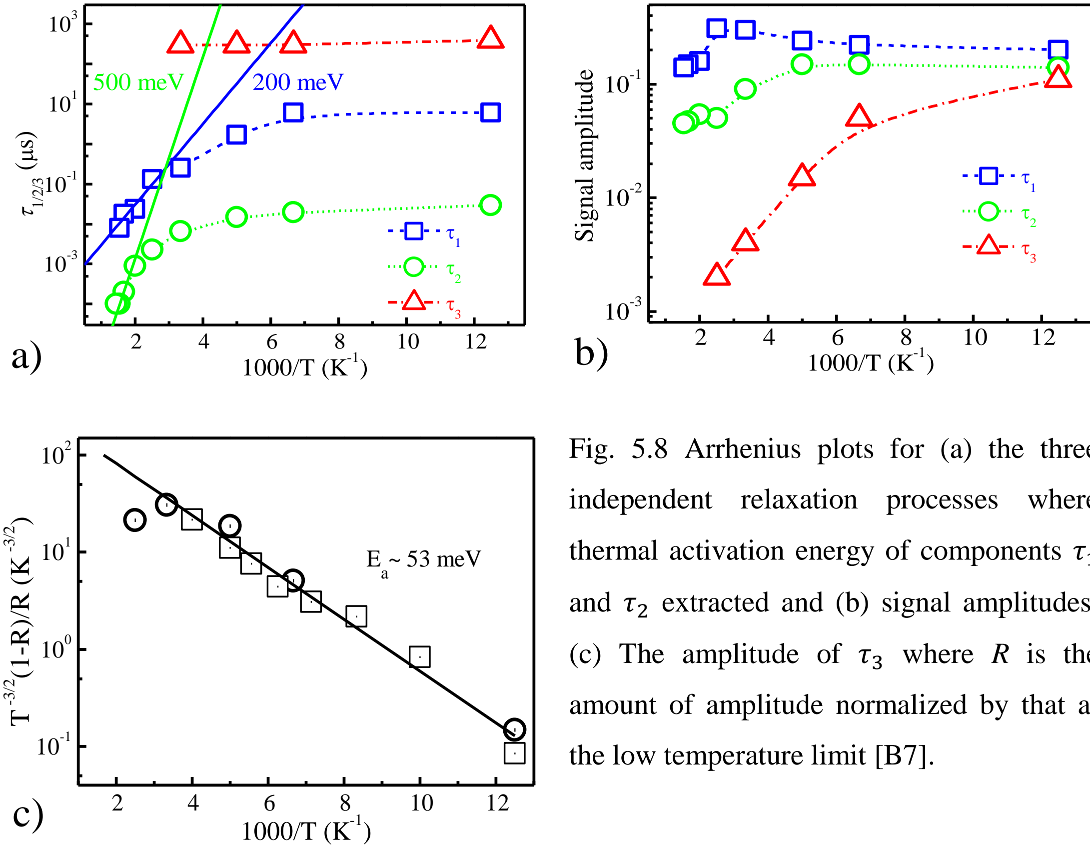

Fig. 5.8 Arrhenius plots for (a) the three independent relaxation processes where thermal activation energy of components τ_1 and τ_2 extracted and (b) signal amplitudes. (c) The amplitude of τ_3 where R is the amount of amplitude normalized by that at the low temperature limit [B7].

Slow component τ_3, however, remains constant with increasing temperature, but its amplitude decrease by two orders. According to the analysis provided by Ichimura [110], the carrier trapping amplitude change without a change of relaxation time can be attributed to minority carrier recombination via the majority carrier trap – after electron is emitted from trap, i.e., the trap cannot capture minority holes. Arrhenius plot of $T^{-3/2}\,(1-R)/R$ for component τ_3 as proposed by Ichimura revealed activation energy of 53 ± 5 meV (see Fig. 5.8 (c)). Here R is amount of normalized amplitude to that at low temperature limit and the factor $T^{-3/2}$ corrects temperature dependence of conduction band density of states. The extracted energy is close to the N donor energy level in heavily doped 6H-SiC.

It is well known that boron atoms are acceptors in SiC and can have shallow boron (sB) and deep boron (dB) energy states in the bandgap [112]. Extracted activation energies can be attributed to sB (200 meV), dB (500 meV) and N (53 meV) energy levels. These values are lower than reported in the literature, namely, sB (220 - 350 meV), dB (550 - 750 meV) and N (80 meV) [111]. The dB centers are related to carbon sublattice and occupy smaller volume than sB centers. Also it can be located either at *k*- or *h*- sites. The discrepancy between these findings and literature can be explained by three reasons. First, high concentration of both N and B induces bandgap shrinkage and perhaps the energy levels spread into impurity band. Second, close distance between dB-N pairs can transform the structure of dB complex. Third, we have omitted recapture process for holes.

Very little is known on centers acting as the competing nonradiative recombination channels [51, B3] and on acceptor traps in co-doped SiC [112]. Here we shall focus on previously observed injection dependence of the carrier lifetimes [51] and their dependence on the concentration of in-grown threadlike defects. The injection dependence of the carrier lifetimes in RF18 sample with lower defect concentration is shown in Fig. 5.9 measured at the 10 μm depth

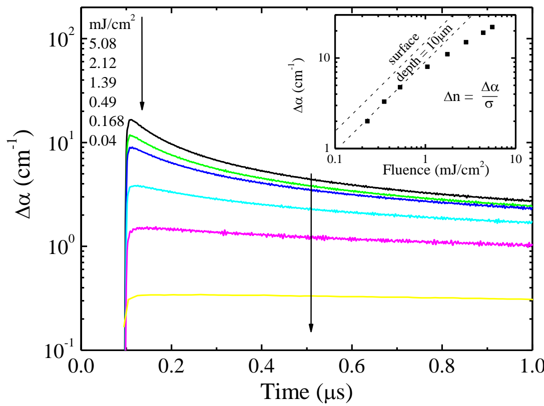

Fig. 5.9 Induced FCA transients and amplitude (inset) at different excitation fluence in the depth position of 10 μm from the excited surface in RF18 sample. Note that carrier lifetimes are injection dependent [B5].

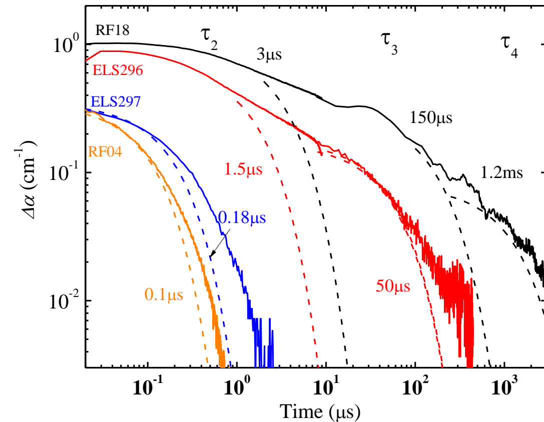

Fig. 5.10 FCA transients on a double-log scale in four samples at 300 K. Exponential carrier lifetime fits are shown by dashed curves [B5].

from the surface using orthogonal pump-probe method. With increasing excitation fluence the FCA amplitude saturation is observed (see inset of Fig. 5.9). The saturation is initiating at 1 mJ/cm^2 excitation fluence which corresponds to injected carrier density of boron at about 5×10^{18} cm^{-3}. It can be attributed to the fact that carrier lifetime becomes shorter than the excitation pulse ($\tau_L < 2$ ns).

Fig. 5.10 shows the corresponding FCA transients on log-log scale in low and high defected samples (Table VII) at the medium carrier injection of about >10^{17} cm^{-3}. Exponential decay fits are shown by dashed lines and time-constants fits are summarized in Table VII below. In the samples with higher defect concentration ELS297 and RF04 quite short and almost exponential reemission τ_2 is detected: 100 ns and 180 ns, respectively. While in two less defective samples ELS296 and RF18, the fast reemission τ_2 is substantially longer covering the range of 1.5 – 3 μs and more exponential processes, τ_3 and τ_4, can be excluded with longer carrier lifetimes being in the range from 50 μs to 1.2 ms. Samples with more defects show faster τ_2 component and the absence of slower decay. In RF-batch samples the short sub-μs lifetime 0.22 and 0.8 μs has been also detected by microwave photoconductivity decay at lower injection level of about 10^{16} cm^{-3} [B5] which are in good agreement with presented FCA measurements.

These samples (presented in Table VII) are *n*-type and grown similarly

Table VII The parameters of sample defects: *(a) carbon inclusions; *(b) polycrystalline inclusions; ambipolar diffusion coefficient *D*. *C*arrier lifetime extracted using various methods.

Sample No.	B (cm^{-3})	Defects (cm^{-2})	*D* (cm^2/s) at 3×10^{18} cm^{-3}	Lifetime (τ)				
				μW-PC (μs)	TG τ_1 (ns)	FCA (μs) τ_1	τ_2	τ_3
ELS 117	4.4×10^{18}	-	0.1	-	8		1.1	50
ELS 118	5.2×10^{18}	-	-	-		15	1.7	200
							1.2	50
ELS 296	2.1×10^{18}	10^1 *(a)	0 ± 0.05	-	6		1.5	50
ELS 297	4.0×10^{16}	10^6 *(a)	1.15	-	0.5		0.18	
RF 18	2.5×10^{18}	10^1-10^2 *(b)	-	0.8			3	150
RF 04	2.2×10^{18}	10^5 *(b)	-	0.22			0.1	

with similar amount of boron (except for ELS297). At room temperature, DAP PL was observed in ELS296 and RF18 samples which yield longer reemission time τ_2 (as earlier in ELS117 and ELS118) however for the samples ELS297 and RF04 with short τ_2 no PL was observed. Therefore the decrease of τ_2 component in RF04 and ELS297 must be related somehow to the extended defect concentration which is four orders higher. Again we observe strong correlation between carrier reemission time and PL emission - for more efficient PL the longer nonradiative recombination times are needed.

The even faster recombination time τ_1 in ns scale and ambipolar diffusion coefficient D were obtained by picosecond TG technique at 3×10^{16} - 1×10^{19} excitation range. The τ_1 and D measured for the injection level of 3×10^{18} cm^{-3} are shown in the Table VII while the recombination time and diffusion coefficient dependence on injected carrier concentration is presented in Fig. 5.11. Both τ_1 and D are significantly related to B concentration. In the sample with the lowest amount of boron ELS297 the τ_1 decreases when injection level approaches B concentration and at $\Delta n \geq 10^{17}$ cm^{-3} it becomes $\tau_1 = 0.5$ ns and remains independent of excitation. For ELS296 and

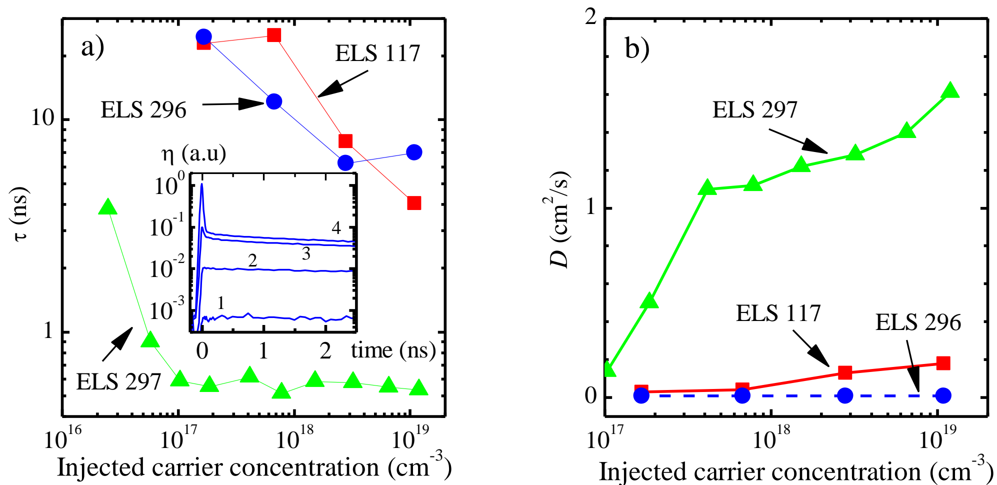

Fig. 5.11 (a) Carrier lifetime and (b) ambipolar diffusion coefficient *versus* excited carrier concentration in N-B co-doped 6H-SiC samples at RT. The inset shows carrier diffraction efficiency η kinetics at increasing excitation fluencies from 0.2 to 12 mJ/cm^2 (1 to 4) in the sample ELS296 [B6].

ELS117 samples with high B concentration the carrier lifetime reaches 20 ns and also decreases with injection level approaching B concentration. The opposite trend is observed for diffusion. For the samples with high B concentration ELS296 and ELS117 the ambipolar diffusion coefficient is very low and on the edge of measurement error D ~ 0.1 cm. For the sample ELS297 with the lowest amount of boron the D sharply increases up to 1.15 cm^2/s at 3×10^{17} cm^{-3} and further slowly increases up to 1.6 cm^2/s at 10^{19} cm^{-3}. Clear increase of D with injected carrier concentration is observed when injection exceeds the B concentration (Fig. 5.11 (b)). It is noteworthy that in the undoped 6H-SiC for similar injection level Δn ~3×10^{18} cm^{-3} the ambipolar diffusion coefficient and lifetime were determined D = 2.7 cm^2/s and $\tau_1 \approx 0.4$ ns, respectively [57].

Carrier lifetime versus diffusion coefficient trend is shown in Fig. 5.12. Clearly the increase of D diminishes carrier lifetime. The opposite relationship between D and τ_1 versus injected carrier concentration (Fig. 5.11) suggests that the carrier lifetime is determined by diffusion limited time to approach the recombination site. This behaviour is quite common for wide bandgap compound semiconductors, and was observed in GaN epilayers [113].

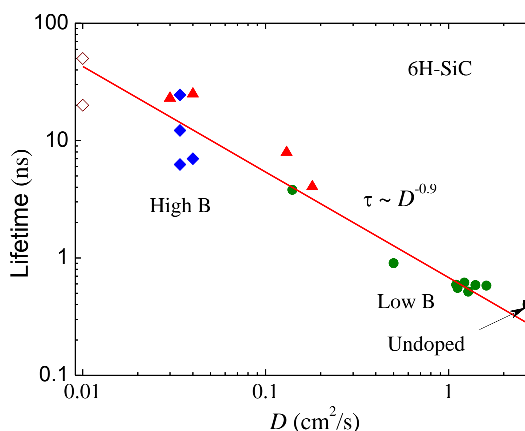

Fig. 5.12 Lifetime versus diffusion coefficient. Boron concentration is also indicated.

For high B concentration at low injection the diffusivity is restricted due to columbic attraction of minority holes to negatively charged B traps. At high injections when the B traps are filled the excess holes can move more freely. Therefore the diffusivity increases with an increase of the free hole and electron concentration. However it leads to increased access to other favourable non-radiative recombination centers. This assumption supports the

experimental finding that PL radiative emission at low injection can be steeply enhanced in co-doped 6H-SiC epilayers with N > B > 4×10^{18} cm^{-3} due to reduction of the carrier diffusion coefficient [114].

5.5. High injection level photoluminescence

We have performed time-integrated PL study by excitation with 355 nm 25 ps duration pulses at various temperatures in samples ELS118 and ELS296 having long nonradiative recombination times.

Measurement was performed from 8 K to 300 K as shown in Fig. 5.13. Both samples emit broad range PL. ELS118 shows 3-5 times higher PL amplitudes than ELS296 for the same excitation fluence. In both samples PL maximum shits gradually to the blue wavelength but the PL peak energy positions are slightly different. At room temperature PL also was measured by orders weaker cw-excitation, as reported in [114] and normalized to RT amplitude the PL data are shown in Fig. 5.13 by the dotted curves. Clearly, the

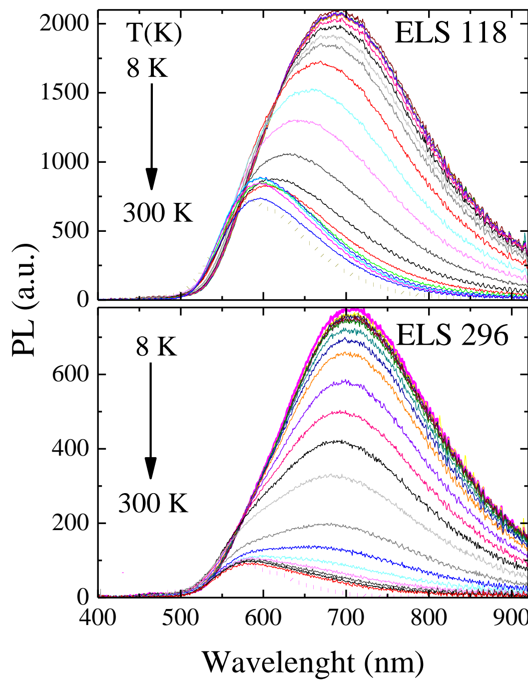

Fig. 5.13 PL spectra of two samples at different temperatures. The excitation fluence is 1.5 mJ/cm^2 [B4].

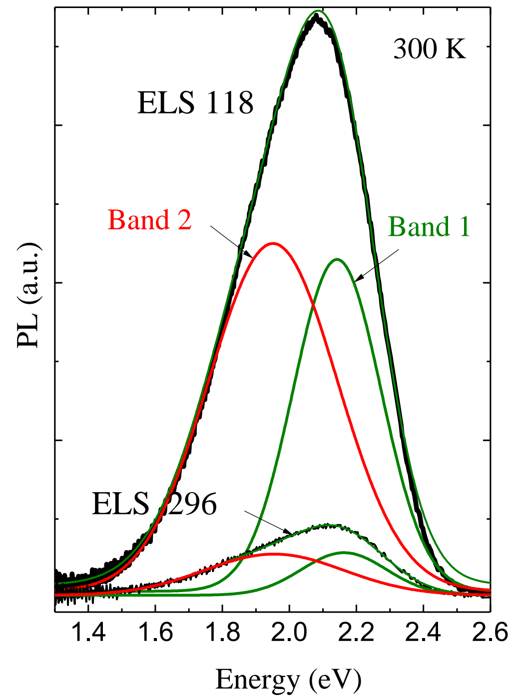

Fig. 5.14 Fitting of two Gaussian bands for PL spectrum of two samples at 300 K.[B4]

high-injection RT PL data display substantial enlargement on the red emitting spectrum side. Nevertheless the cw-excited PL show weaker shoulder at 610 - 630 nm which is attributed tentatively to the phonon-assisted replica in the N-dB DAP emission mechanism (as in Fig. 5.2.) [114]. For the high-injection conditions we did not record any shoulder at fluence from 0.025 to 2.5 mJ/cm^2. The shoulder most likely is over helmed by a broad PL enlargement on the red wavelength emission side.

The best fit to PL yielded that PL spectra consist of two overlapping Gaussian shapes (see Fig. 5.14). Peak energy positions (half-width) at 2.15 eV (0.25 eV) and 1.95 eV (0.45 eV) at 300 K which are denoted as “Band 1” and “Band 2”, respectively. In order to explore temperature behaviour the same fitting procedure was performed for each measured temperature. Gaussian fitting parameters are shown Fig. 5.15. With increasing temperature: “Band 2” energy position for both samples increase but “Band 1” increases only in ELS118 while ELS296 peak energy remains constant; FWHM is slightly shrinking in both samples; the amplitude for “Band 2” steeply decreases in both samples; the amplitude for “Band 1” decreases in ELS296 while in ELS118 it remains about the same. In general two band model is applicable for temperatures higher than 100 K. At RT the amplitudes of two bands are almost equal while at $T < 50$ K one band (single Gauss fit) is sufficient to explain the PL.

In Fig. 5.16 single Gauss fit parameters at 8 K dependence on excitation intensity is shown. With increasing excitation fluence: the energy peak position is almost independent in both samples; FWHM exhibit slight decrease; the amplitude increase linearly until 0.2 mJ/cm^2.

The deep boron (dB) is the dominant acceptor impurity with energy ~550-750 meV in the investigated epilayer [51]. Thus, the electron emission from N trap to the dB, i.e., DAP emission, could be related to the “Band 2”. The “Band 1”, which intensity increases with temperature, can be assigned to the emission of free electron from conduction band (CB) to the dB.

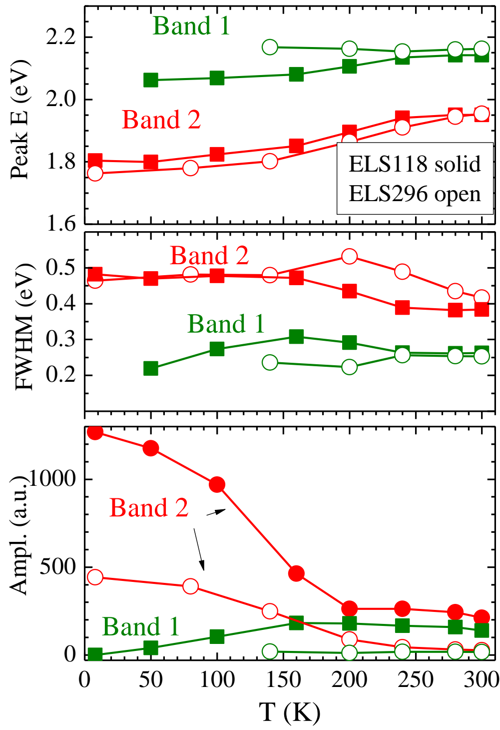

Fig. 5.15 T-dependencies of "Band 1" and "Band 2" peak energy, FWHM and the relative amplitudes at the excitation fluence of 1.5 mJ/cm^2 [B4].

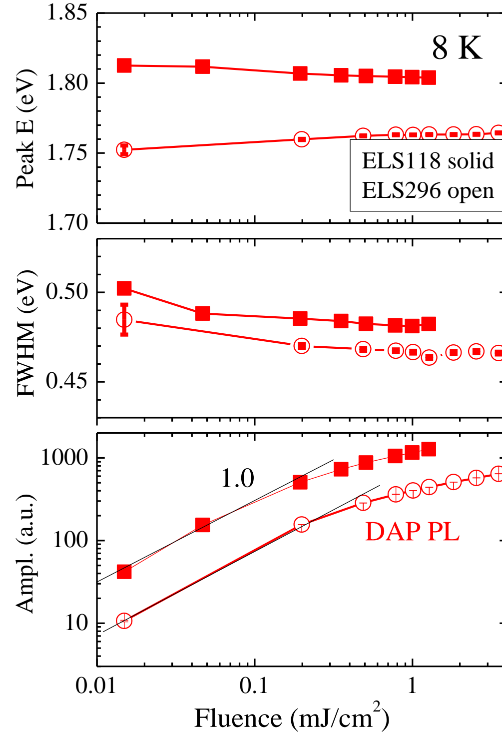

Fig. 5.16 "Band 2" dependences on fluence of PL peak energy, FWHM and the amplitude in two samples at 8 K [B4].

Electron and hole pairs for DAP process are located in a close lattice sites and present the strongest coulomb interaction. Larger energy photons contributing to the blue side of the DAP process band [78] evaluated by Eq. (2.24) for infinite distant pairs. Therefore, emission from "Band 2", would account for $h\nu < 2.2$ eV energy transitions, estimating $E_g = 2.95$ eV, $E_a = 0.65$ eV, $E_d = 0.1$ eV. For the emission of electron from CB-to-dB (for "Band 1") the donor energy is set to zero, $E_d = 0$ eV, which corresponds to emission at $h\nu > 2.3$ eV. Both approaches cannot account for the red energy side of the observed PL spectra. Thus, to explain PL spectra by the DAP recombination model it should be assumed that either the impurities are distributed in a wider energy range within the bandgap or that the energy portion is taken by the assisted phonons which are common to the SiC. An alternative approach could be excitonic recombination mechanisms at the deep trap but this mechanism is unlikely at high-injection conditions.

In Fig. 5.17 the Arrhenius plots for the amplitude of “Band 2” in ELS118 and ELS296 are shown. Excluding the high T range for the sample ELS118, we may estimate from the slope of PL the activation energy of the trap - 53 meV. This value is in a perfect agreement to the same value deduced for the hundred-μs-long electron lifetime component in the sample ELS118 (see Fig. 5.8).

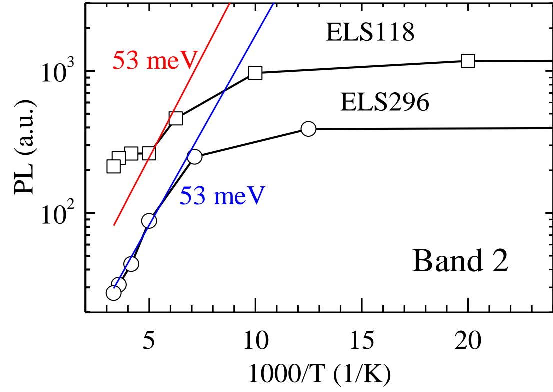

Fig. 5.17 Arrhenius plot of PL amplitude for the “Band 2” [B4].

5.6. Recombination scheme

To summarize the obtained findings we provide a possible recombination scheme which is shown in Fig. 5.18. Extracted activation energies can be attributed to sB (200 meV), dB (500 meV) and N (53 meV) energy levels. Carrier reemission processes from sB, dB and N energy states with time constants τ_1, τ_2 and τ_3 are also indicated in Fig. 5.18, correspondingly. Also

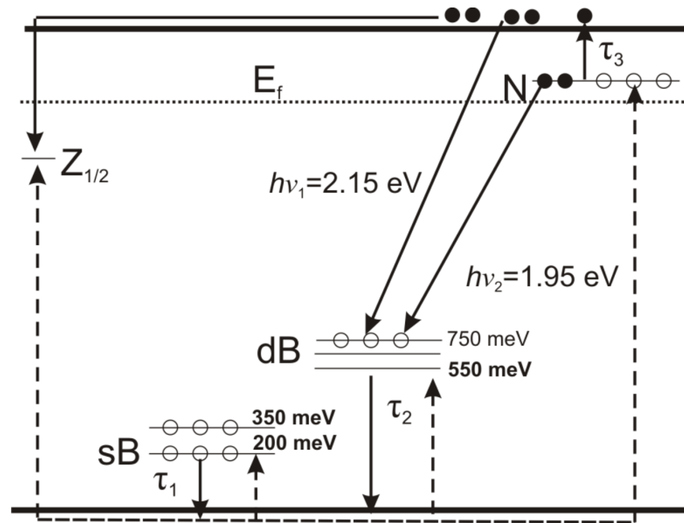

Fig. 5.18 Band diagram and possible recombination scheme. Carrier reemission processes from sB, dB and N energy states with time constants τ_1, τ_2 and τ_3 and nonradiative recombination channel through $Z_1/_2$ center are indicated. Radiative recombination occurs from CB-to-dB and N-to-dB.

$Z_{1/2}$ (carbon vacancy) center is shown which is mainly responsible for non-radiative recombination in SiC with a microsecond long time constant. This path is suppressed due to observed low diffusion of the free electrons in a heavily co-doped 6H-SiC. Radiative emission from boron center also competes with nonradiative recombination channel through dominating $Z_{1/2}$ type center.

From PL spectra we extracted two overlapping bands: "Band 1" and "Band 2" which at room temperature yield energies $h\nu_1 \cong 2.15$ eV and $h\nu_2 \cong 1.95$ eV (see Fig. 5.18). "Band 1" we attribute to transitions from conduction band to deep boron (CB-to-dB) and band 2 from nitrogen to boron (N-to-B). However the PL peak energy positions and impurity activation energy values do not fully overlap to explain obtained results.

5.7. Summary

The favourable conditions for DAP emission can be obtained for co-doped 6H-SiC with high B concentration but still smaller than the N concentration. In this case, the restricted diffusivity (most probably due to induced space-charge field of trapped holes) is a limiting factor of electron recombination through nonradiative centres. Multiple trapping of electrons to N traps stimulates further radiative emission to dB levels. To achieve efficient DAP luminescence in co-doped samples the long reemission times (up to ms) from B traps are needed. This can be optimized by balancing the doping and improving the crystal quality of the material.

By applying PL measurements at high-injection levels we have shown that PL emission spectra are composed of two distinct broad bands. The low energy band we relate to the phonon-assisted N-to-dB DAP radiation with a thermal activation energy of 53 meV which is assigned for the N-trap. While the high energy band component is attributed to the phonon-assisted free-electron radiation recombination from CB-to-dB trap. The general behaviour of the T-dependencies in PL bands is basically governed by the occupation probability of the N-trap.

The free carrier absorption depth distribution in co-doped B-N 6H-SiC shows that, even at high injection level, the surface recombination driven by carrier diffusion is small. However, by increasing injection into bipolar regime diffusion allows access to the non-radiative centers and carrier recombination rate increases. Diffusion coefficient and carrier lifetime are both dependent on B concentration and behave in the opposite way versus injected carrier concentration.

6. 4H-SiC thin epilayers

This chapter is oriented towards the effort to achieve a better surface passivation technique using 4H-SiC epilayers for field transistor applications. Our goal was to evaluate the relative trend of surface recombination velocity (SRV) in order to find critical points depending on the passivation scheme for oxides SiO_2 and Al_2O_3. In addition, passivation resistance to external radiation has been studied by an effect of Ar^+ ion irradiation at the interface between dielectric and 4H-SiC employing specific ions of an energy range where elastic (nuclear) scattering dominates. Silicon dioxide (SiO_2) is the common choice in most 4H-SiC applications today and has been studied in comparison to a potential alternative of dielectric Al_2O_3 [62], to test the reliability of the interface after severe damage.

6.1. Experimental approach

4H-SiC epilayers were grown by hot-wall CVD on high quality *n*-type 4° off-axis Si face (0001) of 4H-SiC wafers (d = 330 – 345 μm), purchased from "SiCrystal" AG company. The doping level of the substrate was of about 1×10^{19} cm^{-3}. The *n*-type epilayer doped with nitrogen (N) 3-5$\times10^{15}$ cm^{-3} had 8-15 μm thickness, while the *p*-type epilayer doped with aluminum (Al) 10^{17} cm^{-3} (only partly activated at room temperature) had a thickness of 7 μm. The samples of 1 cm^2 size were cut and then treated by different passivation techniques to accomplish various degrees of surface passivation. SiO_2 film was deposited using plasma enhanced CVD while Al_2O_3 was deposited by atomic layer deposition (ALD) using the precursors – trimethyl aluminum (TMA) for Al and H_2O for the oxide at 250 -300 ºC. More details on sample preparation see in Refs. [B1, B2]. First set of samples was: (a) a reference *n*-type sample with naturally formed native oxide due to exposure to air (estimated thickness is about 2 nm); (b) a *n*-type sample with 50 nm SiO_2 film; (c) a *n*-type and (d) a *p*-type samples covered by 80 nm Al_2O_3 film. No annealing was done prior to the measurements for this set of samples.

Another set of samples with high quality oxides were prepared for radiation impact investigation. Identical epilayers of 8-10 µm were grown by the same growth process and then different passivation processes applied. Samples with SiO_2 (e) after deposition were annealed at 1150ºC N_2O environment and the oxide thickness of 54 nm was determined afterwards by thin film interferometry. Samples with Al_2O_3 (f) were obtained by thermal ALD process using TMA which provided 56 nm Al_2O_3 film. A backside contact was then provided with nickel silicide for CV measurements. Rutherford backscattering analysis was performed on SiO_2/SiC and Al_2O_3/SiC structures and revealed no contamination from precursor gases also validated the stoichiometry of the oxide layers.

These sample sets (e-f) were exposed to 50 keV argon ions (Ar^+) at room temperature using an ion implanter at Ion Technology Center in Uppsala, Sweden. The fluence of Ar ions was varied from 1×10^9 to 1×10^{13} cm^{-2}. Samples with different exposure doses were obtained. Simulations by the SRIM simulation have shown that the Ar ions produce large amount of elastic scattering damage at the interface between the oxide and SiC. A summary of the sample parameters is given in Table VIII.

All samples were polished from the back side (substrate) to provide good optical quality surfaces for probe beam penetration. The samples were excited with 355 nm quantum via oxide film to epilayer under ambipolar level injection condition using the optical collinear pump-probe measurement scheme (see Fig. 3.1(c) and Fig. 3.2). The carrier decay was obtained in various positions in the sample and 40 - 100 decay data were extracted for

Table VIII Summary of sample growth parameters.

Preparation method	Epilayer thickness (µm)	Doping type	Epilayer doping (cm^{-3})	Oxide type (thickness in nm)
(a)	15	*n*-type	$(3\text{-}5)\times10^{15}$	SiO_2 Native (2)
(b)	15	*n*-type	$(3\text{-}5)\times10^{15}$	SiO_2 (50)
(c)	15	*n*-type	$(3\text{-}5)\times10^{15}$	Al_2O_3 (80)
(d)	7	*p*-type	1×10^{17}	Al_2O_3 (80)
(e)	8-10	*n*-type	$(3\text{-}5)\times10^{15}$	SiO_2 (54)
(f)	8-10	*n*-type	$(3\text{-}5)\times10^{15}$	Al_2O_3 (56)

every sample to maintain good statistics. For (e) and (f) sample sets CV measurements were also performed.

The pulse energy of 13 μJ was maintained constant for all measurements; Applying α_{4H} – for 355 nm of ~ 200 cm^{-1}; Spot area S_{area} = 0.5 mm^2; and R – reflectivity (0.25), we calculated by Eq. (2.20) the injected excess carrier density in the epilayer ~ 7×10^{17} cm^3. No Auger recombination occurs in 4H-SiC under these injection conditions [115] and, under bipolar condition, we can expect the same bipolar lifetime value for holes and electrons.

6.2. Carrier lifetime and surface recombination

A typical carrier decay transient after laser pulse excitation is shown in Fig. 6.1 and similar ones were measured in other samples. The FCA decay comprises of three decay parts which can be distinguished: a fast one, an intermediate and a slow tail. The fast component lifetime is around 15 ns as measured only in the substrate (red dashed line in Fig. 6.1). Since the light penetration depth $1/\alpha_{4H} \approx$ 50 μm is more than the epilayer thickness a fraction of excess carriers generated in the substrate also is visible in the kinetics [116]. It varies on the polarization and wavelength of the probe light [117] and for 861 nm wavelength under $E \perp c$ polarization used, this component is smaller than for corresponding 1300 nm probe wavelength [58, 118]. The intermediate component refers to the effective carrier lifetime in the epilayer τ_{epi} [119] which is of the major importance in the current investigation. The remaining tail of the decay is caused by carrier trapping (mainly in the substrate) due to carrier leakage over the epilayer/substrate interface [119]. The sum of the three recombination processes gives a resultant experimental curve. The slow component is expected to be of very small amplitude within time span of 1-2 τ_{epi}, therefore, it has no significant importance to our measurements and will not be analyzed further. So, we extracted τ_{epi} by fitting an exponential slope rejecting fast and slow parts as show in Fig. 6.1 with dashed blue line.

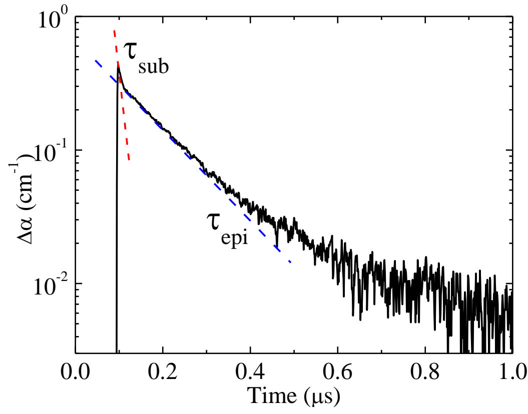

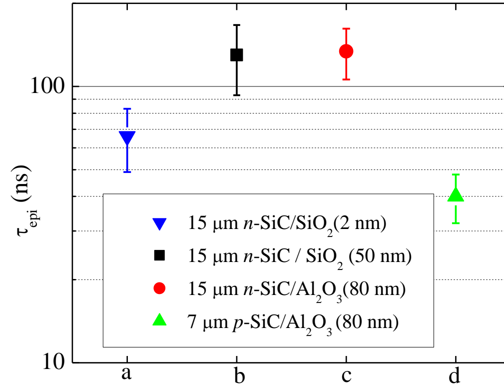

Fig. 6.1 FCA decay for sample passivated with SiO_2 film: exponential lifetimes in the substrate and in the epilayer are shown by dashed lines [B1].

Fig. 6.2 Extracted effective lifetime τ_{epi} in the epilayers with different surface treatments using SiO_2 and Al_2O_3 oxides [B1]. Error bar shows the standard spread.

Extracted effective carrier lifetimes τ_{epi} and standard its spread for each sample is shown in Fig. 6.2. The longest lifetimes are observed in 4H-SiC *n*-type samples passivated with SiO_2 and Al_2O_3 oxides which vary around 130 ns. In a reference sample (with native oxide) the lifetime value was ~70 ns. The lowest lifetime was observed in the thinnest *p*-type sample with Al_2O_3 oxide and its value was about 40 ns.

In the following SRV simulation we will assume that S_1 (at the epi/substrate plane) is constant (as determined by growth technique) and S_2 (at the epi/film plane) can be varied via passivation, hence it can be much smaller than S_1. Numerical simulations were performed for two cases by solving Eqs. (2.14) - (2.16). First, when $S_1 = S_2 = S$ then the fundamental mode carrier depth distribution in the sample is of the symmetrical form. This case is illustrated in Fig. 6.3(a) for S = 10^3, 10^4, 10^5 cm/s after 100 ns (dashed line shows initial carrier distribution at $t = 0$). The carrier diffusion flow is directed equally towards opposite surfaces and the appropriate solution for lifetime is given by Eq. (2.17). Second case, when $S_1 \gg S_2$, then it causes excess carrier diffusion flow towards the S_1 surface because of the asymmetrical carrier distribution across the sample as shown in Fig. 6.3(b). As a result, the surface recombination lifetime varies according to Eq. (2.18).

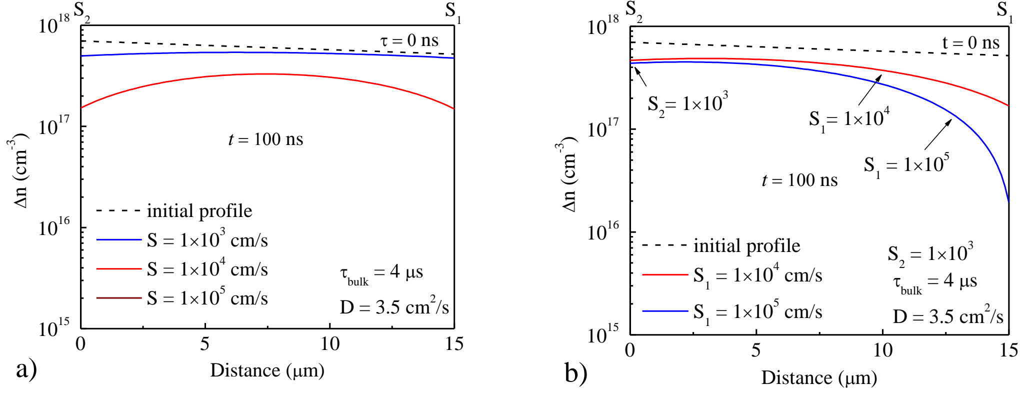

Fig. 6.3 Excess carrier quasi-stationary distribution across 15 µm of thickness thin slab after 100 ns time lapse (a) for the homogeneous surface recombination case then $S_1 = S_2$ and (b) for the asymmetrical surface recombination case $S_1 \gg S_2$.

According to the two possible limiting conditions as described above, we have developed a formula for the intermediate cases of a surface recombination ratio $S_1/S_2 > 1$:

$$\frac{1}{\tau_{epi}} \cong \frac{1}{\tau_{bulk}} + \left(\frac{d}{k^2 S_1} + \frac{d}{k^2 S_2} + \frac{4d^2}{k^2 D \pi^2}\right)^{-1}. \tag{6.1}$$

Here k is a dimensionless coefficient developed empirically which confirms both the symmetrical Eq. (2.17) and the asymmetrical Eq. (2.18) cases:

$$k = 1 + 10^3 / \left(10^3 + \left(\frac{S_1}{S_2}\right)^2\right). \tag{6.2}$$

From Eq. (6.2), it follows that when $S_1 = S_2$ the $k = 2$ and Eq. (6.1) becomes Eq. (2.17). When $S_1 \gg S_2$ the $k = 1$, and Eq. (6.1) becomes Eq. (2.18). When S_2 is somewhere in between the Eq. (6.1) gives a smooth transition towards the other boundary condition. The coefficients in Eq. (6.2) were chosen empirically to fulfill a k value in a sufficiently large range of the S_1/S_2 ratio.

The proposed model of the problem for a transient solution between symmetric and asymmetric SRV on two surfaces is not unique. Several more sophisticated models have been applied for carrier lifetime evaluation in 4H-SiC epilayers [120, 121]. We should note that reasoning of the model depends

on the experimental technique, and the thickness of samples in respect to laser light penetration depth. Authors typically apply mixed simplification with a numerical fit for a particular case [70]. Since we are interested in the tendency of the SRV reduction on the passivation scheme rather than on the actual SRV values, our model looks applicable for integrated FCA type measurement under a small epilayer thickness ($d \ll 1/\alpha$) and a constant medium/high injection condition ($\Delta n = \Delta p \gg n_0, p_0$) when a constant D value can be used at room temperature.

The next step is to simulate lifetime versus epilayer thickness curves according to Eq. (2.17) and Eq. (6.1) for different values of recombination parameters. The diffusion coefficient was set to be D = 3.5 cm^2/s (a common value for 4H-SiC) for carrier injection of about 10^{17} cm^{-3} [89]. Excess carrier bulk lifetime τ_{bulk} is not known precisely for particular growth process in these epilayers. It can be varied in the range τ_{bulk} = 0.3 - 4 μs covering a typical range for values observed in a number of thick epi-growth 4H-SiC layers by CVD. However, we are going to use mainly the highest bulk lifetime of 4 μs value, since the epilayer quality is improving annually [122]. The bulk lifetime is the upper boundary in simulation since it is described only by inner processes.

The obtained experimental data from every sample is compared with two sets of simulated curves in Fig. 6.4. The first set was made for the homogeneous case $S_1 = S_2$ where SRV were simulated from 2×10^3 cm/s to 1×10^6 cm/s as shown by solid lines. The extracted lifetimes (see Fig. 6.2) are also shown according to epilayer thickness (sample (c) is slightly shifted in x-axis for better view). Lifetime values in *n*-type samples with SiO_2 and Al_2O_3 films and also *p*-type epilayer fits in between simulated lines of $S_1 = S_2 =$ 1×10^4 – 2×10^4 cm/s. Only the sample with native oxide indicated the highest SRV rates of 10^5 - 10^6 cm/s.

A second set of curves was also simulated for the asymmetrical carrier distribution case $S_1 > S_2$ using Eq. (6.1). Simulation was made assuming a high value of $S_1 =$ 1×10^6 cm/s at the epi/substrate interface while S_2 at

epi/oxide interface was varied. Simulated sets for S_2 varying from 1×10^4 to 1×10^5 cm/s are shown in Fig. 6.4 with dashed lines. The fit gives values of $S_2 = 4\times10^4$ cm/s in *n*-type epilayer and about 3×10^4 cm/s in *p*-type epilayer. The sample with native oxide could be described again with high SRV of $S_2 > 1\times10^5$ cm/s, although Eq. (6.1) becomes Eq. (2.17) when S_2 approaches $S_1 = 1\times10^6$ cm/s.

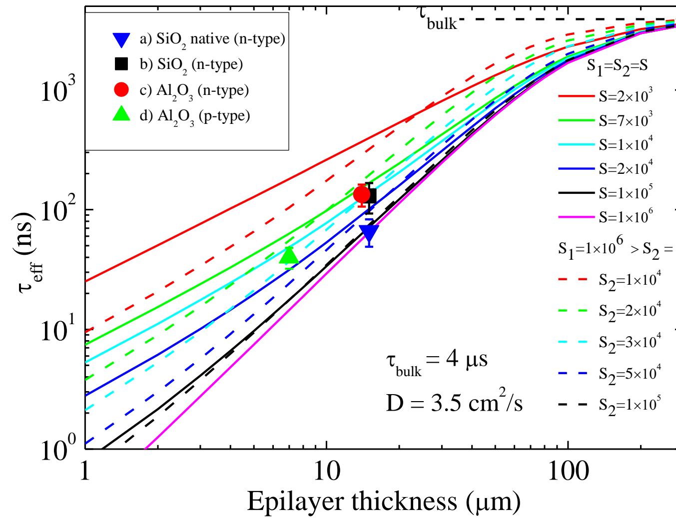

Fig. 6.4 Simulated curves for various SRV values are shown for effective carrier lifetime as a function of epilayer thickness. Points represent experimental results. Solid lines are constructed for the case $S_1 = S_2$ by Eq. (2.17) and dashed lines are constructed for the case $S_1 > S_2$ by Eq. (6.1) when $S_1 = 1\times10^6$ cm/s. Other parameters remain constant $\tau_{bulk} = 4$ μs, $D = 3.5$ cm²/s [B1].

The fit for the asymmetrical SRV profile gives slightly higher S_2 values than for the symmetrical case. To establish the actual one value it is crucial to know all parameters, such as diffusion coefficient and the bulk lifetime. The diffusion coefficient for possible excess carrier density variation was evaluated in Fig. 6.5. With increasing diffusion coefficient, curves representing the same SRV shifts downwards describing a region with lower carrier lifetimes. Nevertheless, the diffusion coefficient variation versus injection might give only a slight shift. Another parameter τ_{bulk} may also vary which influence is shown in Fig. 6.6. However, with decreasing τ_{bulk} the τ_{eff} is affected only for thicker layers and for given case affecting at about 20 – 30 μm epilayer thicknesses and thicker.

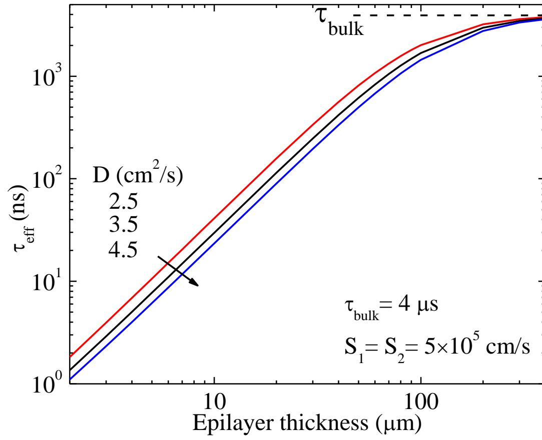

Fig. 6.5 Influence of diffusion coefficient for lifetime curves while other parameters remain constant [B1].

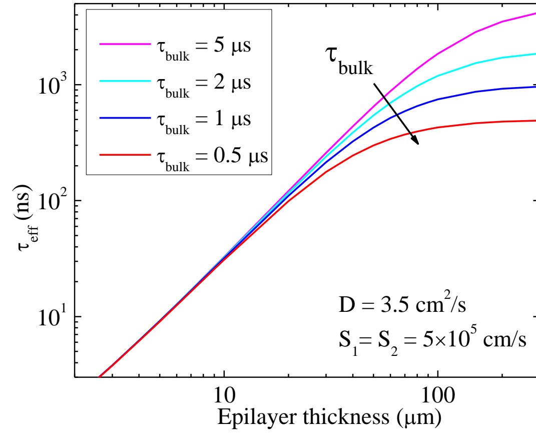

Fig. 6.6 Influence of bulk lifetime τ_{bulk} to lifetime curves for same SRV.

Two measurements were conducted to evaluate oxide reliability before and after Ar^+ implantation to the (e) and (f) sample sets: CV and FCA. It can be observed from CV measurements of SiO_2/SiC (Fig. 6.7(a)) that for low Ar^+ fluence no significant flat band shift (V_{fb}) occur until the fluence level of 1×10^{11} cm^{-2}. Here the shift in V_{fb} demonstrates an increase in the amount of charge in the oxide. It was estimated by Terman method that trap density increased at least 6 times compared to undoped sample. For higher fluence the CV curve starts to be severely affected. Also the hysteresis in CV curve is also increased for higher ion fluence which indicates increased number of near interface states. On the other hand, the Al_2O_3 interface is not so strongly affected (Fig. 6.7(b)) and a capacitor can still hold charge until 1×10^{12} cm^{-2} of fluence. Also the hysteresis remains unaffected. Together it means less surface defects in the interface.

The average lifetimes extracted from FCA measurements for SiO_2 and Al_2O_3 after producing damage near the interface with different Ar^+ fluencies are show in Fig. 6.8. For the interface made with SiO_2 the lifetime dependence on surface defects is clearly fluence dependent. The decrease of lifetime was observed until 5×10^{11} cm^{-2} of Ar fluence. Close to the fluence where V_{fb} occur. Then it remains constant probably due to the increased charge in the oxide caused by electronic stopping. On the other hand, interface with Al_2O_3 does not

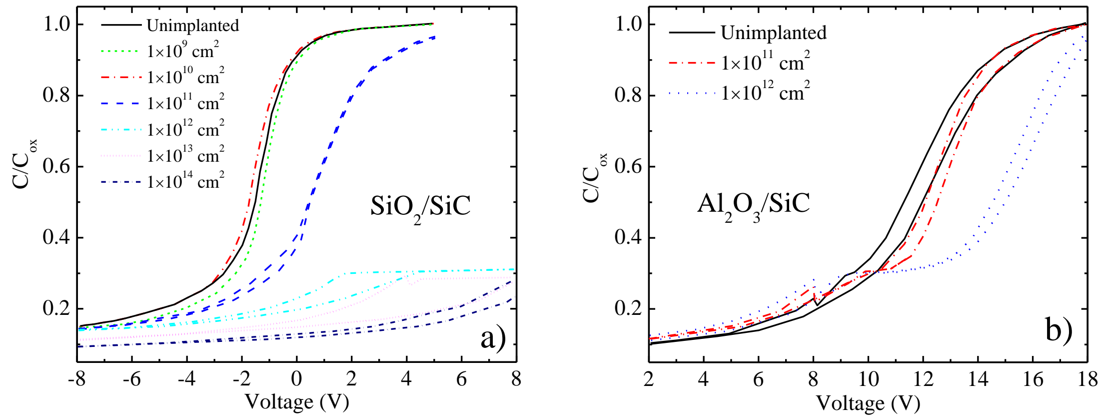

Fig. 6.7 High frequency (100 kHz) CV characteristics of Ar^+ implanted (a) SiO_2/SiC (b) Al_2O_3/SiC [B2].

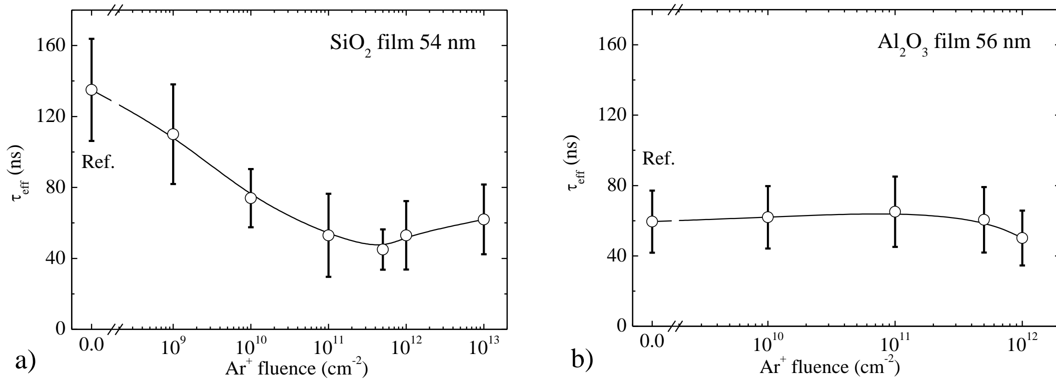

Fig. 6.8 Effective lifetime in the epilayer after different Ar implantation dose for (a) SiO_2/SiC and (b) Al_2O_3/SiC [B2].

show any lifetime dependence on fluence which is nearly constant for all implantation doses. Slight lifetime reduction was observed only at the highest Ar dose where the highest V_{fb} shift is observed. This yields higher stopping values in the oxide and less damage to the interface.

The carrier lifetime dependence results are in qualitative agreement with the CV measurements. Damaged interface states in the epilayers passivated with SiO_2 clearly influence the carrier lifetime or, in other words, surface recombination velocity. However, in the epilayers with Al_2O_3 the carrier lifetime is not affected so strong. Therefore, it may be concluded, that Al_2O_3 could withstand higher nuclear scattering damage and shows less interface degradation.

6.3. Summary

We have compared the interface quality of thin 4H-SiC epilayers prepared by the same epitaxial process but passivated with two different oxides: common choice SiO_2 and promising alternative Al_2O_3. We have presented a simple model for graphical evaluation of surface recombination velocity (SRV) using carrier lifetime dependence on epilayer thickness simulated using different SRV parameters. We have found that the highest SRV was in the n-type epilayer with native SiO_2 which yield limiting SRV of 10^5 – 10^6 cm/s. The n-type samples passivated with high quality SiO_2 and Al_2O_3 yielded the SRV which was well described for the case $S_1 = S_2$ within 1×10^4 – 2×10^4 cm/s and for $S_1 > S_2$ within 2×10^4 – 4×10^4 cm/s, respectively. The p-type epilayer was grown thinner, yet still fitted within SRV values of about 1.5×10^4 cm/s and 3×10^4 cm/s.

Although passivated epilayers with high quality SiO_2 and Al_2O_3 showed similar carrier lifetime and SRV, after nuclear scattering damage at the interface (produced by Ar^+ bombardment) the Al_2O_3/SiC interface appears to be substantially less affected by ion implantation damage in comparison to the SiO_2/SiC. It shows that Al_2O_3 may offer relatively higher resistance to nuclear scattering damage and shows less degradation at the interface. This makes Al_2O_3 oxide a good candidate for application in radiation rich environment.

7. 3C-SiC free standing wafers

Here, we study free-standing 3C epilayer obtained by etching away the Si substrate. We identify residual stress effect regions that lie parallel to the epilayer surfaces. We show that lifetime is reduced in stressed regions towards the surfaces. However in the middle region the lifetime is high. We provide absorption edge spectra below band gap. By depth-resolved FCA the absorption is measured down to the value of 0.01 cm^{-1} at room temperature. This is exceeding the 5 cm^{-1} limit caused by unintentional doping at RT.

7.1. Experimental approach

3C-SiC was grown by CVD technique (*Hoya* Ltd.) on undulated Si (001) substrates [123] with ridge-to ridge direction etched parallel to [110] direction. The advantage of this technique is that originating stacking faults (SFs) are terminated by other crossing SFs which makes total reduction of SFs density in the middle of the epilayer. However, it was experimentally observed that SFs vanish with increasing epilayer thickness but still a considerable amount of SFs remains. The epilayer was unintentionally doped by hydrogen with concentration varying (1 – 3.5) $\times 10^{17}$ cm^{-3}. After growth the substrate was removed by chemical etching and the back side was polished to optical quality. Free standing 3C-SiC wafer was obtained with final thickness of 160 μm. Then the wafer was cut into strips of 0.7 - 1 mm width and their cross sections were polished. The stripes were examined by optical microscope and DPB defects and stressed regions have been revealed.

The properly polished samples were applied for FCA measurements at orthogonal geometry which was exploited for two sample orientations (see Fig. 3.1(a), (b) and Fig. 3.2). Note that here (for cubic material) *c*-axis denotes growth direction of epilayer. The crosscut surface of the epilayer was homogeneously excited and in-depth scans were performed for absorption edge measurements. For lifetime measurements on the mid cross section part the top epilayer was excited by the pump beam while the probe beam penetrated the crosscut. The excitation level was maintained at about 5×10^{17} cm^{-3}.

7.2. Absorption edge

Exponential in-depth free carrier absorption $\Delta\alpha_{\mathrm{FCA}}$ profiles for different excitation quanta are shown in Fig. 7.1. Exponential fits are applied by solid line which provides bulk absorption coefficient and agrees well with the data found in literature [124-127]. With decreasing excitation quanta the slope becomes more flat and it is hard to extract low absorption coefficients. Nevertheless, after $\Delta\alpha_{\mathrm{FCA}}$ profile becomes flat the $\Delta\alpha_{\mathrm{FCA}}$ amplitude can be still detected by two orders below. Therefore the amplitude can be pinned at higher absorption coefficients and the low band-to-band absorption coefficients α_{bb} may be extracted (see chapter 3.4. for more details). In Fig. 7.2 solid circles are the data extracted from exponential in-depth slope as in Fig. 7.1. The data points at 10 cm^{-1} and 6 cm^{-1} were used as pinning points for relative $\Delta\alpha_{\mathrm{FCA}}$ amplitude measurement which are shown by open circles at 77 K and 295 K temperatures. Our data at 77 K is in good agreement with absorption data shown by blue line from Ref. [128] at 4.2 K. Room temperature data show step like structure below bandgap value ($E_g \cong 2.36$ eV) which is a consequence of phonon-assisted optical transitions. In fact, we performed multiphonon absorption spectra fit (Eq. (2.21)) to find the best match at 295 K and 77 K temperatures (solid black lines). The phonon energies and relative amplitudes were taken from PL spectra in Ref. [129] and shown in Table IX. Other fitted parameters were maintained constant for all temperatures: $A_1 = 0.054$, $A_2 = 1$, $E_{ex}^{i} = 30$ meV and $E_{gx}^{i} = 2.36$ meV.

Table IX Fitted phonon energies and strength parameter

Phonon	TA	LA	TO	LO
E_{ph} (meV)	49.3	79.4	94.4	102.8
C^{p}	505.7	1372	2131	1733

At room temperature we obtained α_{bb} values much below 5 cm^{-1} (Fig. 7.2) which is a common limit due to unintentional nitrogen impurity absorption in standard transmission measurements. The impurity absorption (5 cm^{-1}) tail overlap the characteristic edge of the phonon-assisted band-to-band absorption,

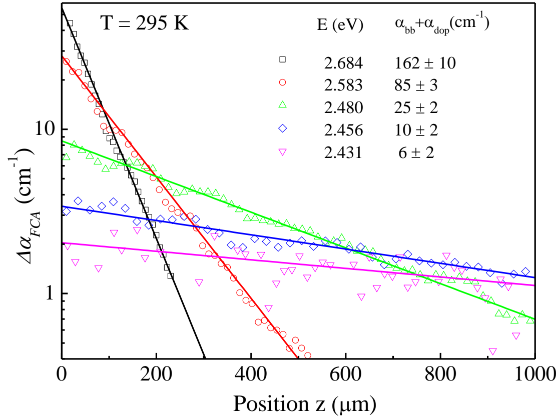

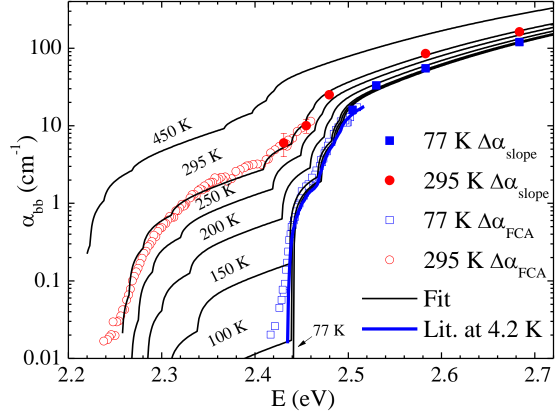

Fig. 7.1 In-depth $\Delta\alpha_{FCA}$ profiles determined for 5 different excitation energies at room temperature. Thin line represents exponential fit. [B9]

Fig. 7.2 Extracted α_{bb} spectra from exponential slope (solid circles) as in Fig. 7.1 which serve as pining points for relative $\Delta\alpha_{FCA}$ measurements (open circles) [B9]. Solid thin lines show multiphonon fits and thick line is taken from [128] at 4.2 K.

while in FCA transient we are able to register only a fraction of band-to-band transitions which are due to non-equilibrium excited carrier pairs.

7.3. Stressed regions influence to carrier lifetime

In Fig. 7.3 a cross section view of 3C-SiC sample under polarized light is shown. Dashed arrows show double position boundary (DPB) defects which are originating from the substrate. The solid arrows parallel to the surfaces extend via whole length of the sample and depict a boundary of a strained region. The probe beam (1540 nm) was transmitted across the sample thickness via the cross section as show in Fig. 7.4. Two dips marked by arrows are caused by probe deflection which occurs due to regions with stress gradient. Deflection indicates a residual strain in the wafer. The dashed line in Fig. 7.4 shows how the ideal probe transmission profile would look like in the sample without tensions.

We measured FCA in-depth profiles at various times after excitation as shown in Fig. 7.5. A zero coordinate in depth is set in the middle of the sample and credible results are obtained in the mid of the sample within about 100 μm.

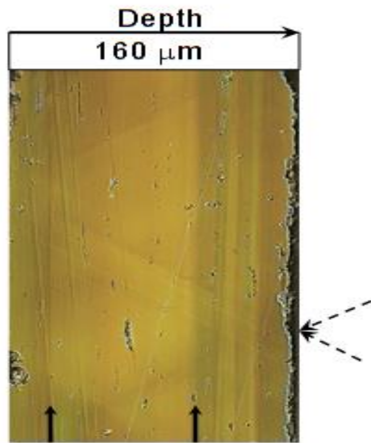

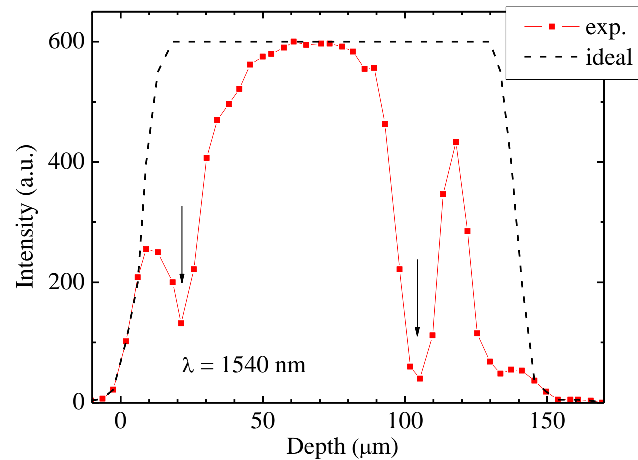

Fig. 7.3 Cross section view of 3C-SiC epilayer under polarized light. Dashed and solid arrows show DPD directions and strain related boundaries, respectively [B8].

Fig. 7.4 Transmitted intensity of 1540 nm probe beam through the cross section (as in Fig. 7.3) of 3C-SiC. Arrows show strained region boundaries. Dashed line shows sample transmittance profile without tensions [B8].

Results near the surface are omitted due to unknown beam reflection path in the sample. The observed asymmetric distribution was clearly observed with an evolution of time in the decay.

In Fig. 7.6 the recombination lifetime is extracted at various depths at 295 K and 77 K temperatures. In the mid of the sample the lifetime is the highest and gradually decreases towards the edges where residual stress regions prevail. At 77 K the measuring position is slightly shifted and the in-depth profile is smoother, perhaps due to an increase of the carrier diffusion coefficient at low temperature. We measured a few distributions in different strips of the same sample. In all cases lifetime obey Λ-shape profile with the highest lifetime value in the middle of the sample. Although it looks very much like as diffusion driven surface recombination but, in fact, diffusion coefficient at 295 K was obtained only 1.4 cm^2/s by transient grating technique. Therefore the lifetime reduction cannot be explained by surface recombination.

We assume the in-grown stress below the subsurface region is responsible for additional defect generation and consequently to the observed lifetime reduction. Recently, lifetime mapping in strained regions in 3C-SiC wafer was

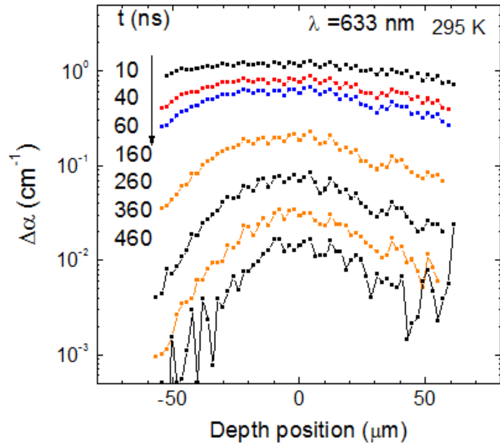

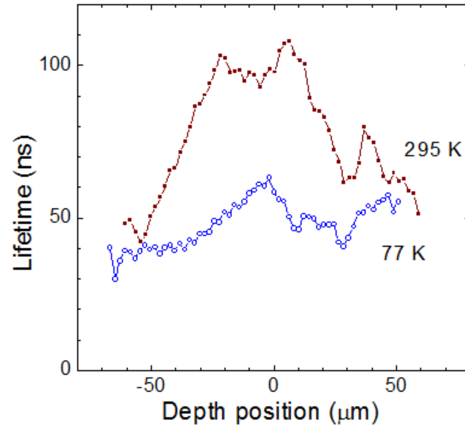

Fig. 7.5 FCA distributions vs. depth position at various times after the pump pulse termination [B8].

Fig. 7.6 Extracted recombination lifetime depth-variation at two temperatures [B8].

performed by Kato et al. [130]. It was shown that defects are present in strained regions at higher concentrations and photo conductance lifetime is shorter than in other regions which agrees with our findings. The results suggest that for devices fabrication using such 3C-SiC wafers, the active regions must be chosen to be outside of strained regions.

7.4. Summary

To conclude, in free standing 3C-SiC grown on undulant Si substrate defect concentration is drastically reduced, however, strain regions has been observed near both surfaces. In these regions the lifetime reduction and perhaps the reduction of minority carrier mobility may exist. However, middle region of the epilayer cross section (~40 μm) showed high lifetime yielding better quality of the material. We have detected the fundamental bandgap absorption edge of 3C-SiC at room and 77 K temperatures much below to the available results in literature (5 cm^{-1}) down to 0.01 cm^{-1}. At room temperature absorption edge is well represented by assisted phonon absorption using four phonons in the strain-free region within the sample. Strain at the top surface can provide high material deterioration of free-standing 3C-wafers. Thus

advanced technology should be developed to avoid these strained areas for device applications.

Concluding summary

$TlGaSe_2$. Photoacoustic response (PAR) is shown to be sensitive technique to obtain absorption spectra in $TlGaSe_2$ due to high dn/dp value and low absorption coefficients. PAR technique could be applicable for other layered semiconductors with low absorption coefficients.

At 77 K in the F-phase at $\boldsymbol{k} \parallel c$ excitation direction (to the layer plane) the bandgap absorption shows optically biaxial character with a light polarization appearing in the layer plain. The anisotropy directions do not match a and b crystallographic directions, which suggests that Tl^+ ions slip and form nonequivalent Tl^+ rearrangement. However, at room temperature at P-phase there is no polarization dependence.

At room temperature we reveal band-to-band photo luminescence in $TlGaSe_2$ and in isostructural $TlInS_2$. The PL signal yields polarization dependence and at $\boldsymbol{k} \perp c$ excitation direction is weak and even weaker in $\boldsymbol{k} \parallel c$ direction. This feature is explained by the existence of absorption enhancement in the near surface region (40 – 100 μm) with modified structural properties in the layer.

Both results the PL at RT and absorption anisotropy spectrum at 77 K could be explained by partly allowed direct exciton absorption with an exciton oscillator strength reduced by 100 times. The PL exciton emission is polarized perpendicular to layer plain.

Three deep donor levels in $TlGaSe_2$:Fe related to Fe impurity are detected from impurity absorption spectra. The fundamental absorption edge structure of the $TlGaSe_2$ crystal remains almost unchanged at least to the doping level of Fe = 0.5 %.

Trap levels were determined of the energy 0.23 - 0.45 eV from conduction band with huge electron capture cross-sections and the total concentration of about $6 \cdot 10^{15}$ cm^3. These traps are attributed to stacking faults. We have discovered sharp carrier lifetime reduction above 10^{17} cm^{-3} hole concentration, which cannot be explained by Auger recombination and is

attributed to diffusion enhancement that increases holes access to electrons across the layer barrier. The existence of such behavior implies that generated excess holes and electrons are spatially separated at low excitations.

6H-SiC. The favourable conditions for radiative emission can be obtained for co-doped 6H-SiC with high B concentration (> 10^{18} cm^{-3}) smaller than the N concentration. PL measurements at high-injection levels have shown that the emission spectrum is composed of two distinct broad bands. The low energy band (~1.95 eV) is related to the phonon-assisted N-to-dB DAP radiation. The high energy band (~2.15 eV) is attributed to the phonon-assisted free-electron radiation recombination from CB-to-dB trap.

Efficient radiative emission has been observed in samples with high reemission time (>1μs) from dB level. Multiple trapping of electrons to N traps stimulates radiative emission to dB levels occupied by holes. Therefore the long (μs to ms) carrier reemission times are needed to prolong hole stay in dB level for efficient DAP luminescence.

Moreover, in B-N co-doped 6H-SiC the diffusion coefficient, even at high injection level, remains small. However, at injection level approaching the concentration of acceptor level (boron), the diffusion coefficient starts increasing promoting the access for carriers to recombination centres, which results in decrease of carrier recombination time. Therefore high B concentration is needed to reduce diffusion (most probably due to induced space-charge field) limiting carrier recombination through nonradiative centres, which in turn increase radiative recombination probability.

4H-SiC. We have compared the interface quality of thin 4H-SiC epilayers grown by the same epitaxial process but passivated with two different oxides: common choice SiO_2 and promising alternative Al_2O_3. We have presented a simple model for graphical evaluation of surface recombination velocity (SRV) using carrier lifetime dependence on epilayer thickness. The highest SRV is observed in the *n*-type epilayer with native SiO_2. In epilayers passivated with high quality SiO_2 and Al_2O_3, the carrier lifetime and SRV are similar. However, after nuclear scattering damage at the interface the

Al_2O_3/SiC interface shows less degradation in comparison to the SiO_2/SiC interface. This makes Al_2O_3 oxide a good candidate for application in radiation rich environment.

3C-SiC. In free standing 3C-SiC grown on undulant Si substrate, defect concentration is drastically reduced, however, strained regions on surfaces have been observed near both surfaces. Lifetime measurements on the cross section of the epilayer have shown higher lifetime in the middle region of the sample (~40 μm of width), while carrier lifetime reduction has been observed towards residual stress regions. Therefore, for device fabrication using such 3C-SiC wafer the active regions are required to be outside of strained regions.

Future outlook

In $TlGaSe_2$, $TlInS_2$ and other layered thallium compounds the intrinsic PL at low temperature should be stronger and more pronounced than at room temperature, therefore, low temperature PL measurements with the confocal spectroscopy certainly would enrich the knowledge of the band structure. Absorption spectra anisotropy at low temperature suggests that similar shift of PL should be observed. Moreover, mapping of PL within subsurface regions could reveal actual conditions for the enhanced absorption. These phenomena can be related to excess carrier separation on different layer plains. Understanding the charge separation phenomenon is clearly needed for the development of various sensing devices using layered semiconductors.

B doping in fluorescing co-doped 6H-SiC remains the main problem for improving DAP luminescence. Investigation of co-doped samples possessing different intrinsic defects (C vacancies, Si interstitials) could resolve an open question for B redistribution between shallow and deep B states in order to enhance DAP emission efficiency.

Series of samples with different epilayer thicknesses of 4H-SiC grown by the same process and passivated by the same technique would give more accurate carrier lifetime trend to establish SRV. Thick epilayer is needed to establish the bulk lifetime thus eliminating one variable.

Investigation of 3C-SiC layer grown on undulant Si substrate could be enriched by examining the same sample crosscut of the epilayer at various steps: 1) with the substrate (as grown), 2) after substrate removal (free standing 3C-SiC), 3) after removal of stressed bottom part in the free standing 3C and 4) after removal of stressed top part of this epilayer. This would reveal if unstrained defectless layer can be obtained and at which step the best quality can be reached.

References

[1] A. M. Panich, *Electronic properties and phase transitions in low-dimensional semiconductors*, J. Phys.: Condens. Matter. **20**, 293202 (2008).

[2] D. J. Knuteson, N. B. Singh, D. Kahler, B. Wagner, A. Berghmans, S. McLaughlin, and K. Schwartz, *Properties of layered crystals for radiation detectors: $TlGaSe_2$*, Hard X-Ray, Gamma-Ray, and Neutron Detector Physics XI, Aug. 2009.

[3] W. Henkel, H.D. Hochheimer, C. Carlone, A. Werner, S. Ves, and H. Schnering, *High-pressure Raman study of the ternary chalcogenides $TlGaS_2$, $TlGaSe_2$, $TlInS_2$, and $TlInSe_2$*, Phys. Rev. B **26**, 3211 (1982).

[4] K. A. Yee and Th. A. Albright, *Bonding and structure of gallium thallium selenide ($GaTlSe_2$)*, J. Amer. Chem. Soc. **113**, 6474 (1991).

[5] G. E. Delgado, A. J. Mora, F. V. Pérez, and J. González, *Growth and crystal structure of the layered compound $TlGaSe_2$*, Cryst. Res. Technol. **42,** 663 (2007).

[6] M. Y. Seyidov and R. A. Suleymanov, *Negative thermal expansion due to negative area compressibility in $TlGaSe_2$ semiconductor with layered crystalline structure*, J. Appl. Phys., **108**, 063540 (2010).

[7] Von D. Müller and H. Hahn, *Untersuchungen über ternäre Chalkogenide. XXIV. Zur Struktur des $TlGaSe_2$*, Z. Anorg. Allg. Chem. **438**, 258 (1978).

[8] V. Grivickas, V. Bikbajevas, and P. Grivickas, *Indirect absorption edge of $TlGaSe_2$ crystals*, Phys. Status Solidi. B **243**, R31 (2006).

[9] S. Johnsen, Z. Liu, J. A. Peters, J.-H. Song, S. C. Peter, C. D. Malliakas, N. K. Cho, H. Jin, A. J. Freeman, B. W. Wessels, and M. G. Kanatzidis, *Thallium Chalcogenide-Based Wide-Band-Gap Semiconductors: $TlGaSe_2$ for Radiation Detectors*, Chem. Mat., **23**, 3120 (2011).

[10] S. G. Abdullaeva and N. T. Mamedov, *Band structure of $TlGaSe_2$ ternary layered crystals*, Phys. Status Solidi B, **133**, 171 (1986).

[11] G. Orudzhev, Y. Shim, K. Wakita, N. Mamedov, S. Jafarova, and F. Hashimzade, *Linearized Augmented Plane Wave Band Structure Calculations and Dielectric Function of Layered $TlGaSe_2$*, Jpn. J. Appl. Phys., **47**, 8182 (2008).

[12] S. Kashida, Y. Yanadori, Y. Otaki, Y. Seki, and A. M. Panich, *Electronic structure of ternary thallium chalcogenide compounds*, Phys. Status Solidi A, **203**, 2666 (2006).

[13] M. P. Hanias, A. N. Anagnostopoulos, K. Kambas, and J. Spyridelis, *Electrical and optical properties of as-grown $TlInS_2$, $TlGaSe_2$ and $TlGaS_2$ single crystals*, Mater. Res. Bull. **27,** 25 (1992).

[14] D. F. McMorrow, R. A. Cowley, P. D. Hatton, and J. Banys, *The structure of the paraelectric and incommensurate phases of $TlGaSe_2$*, J. Phys.: Condens. Matter, **2**, 3699 (1990).

[15] K. Maschke and H. Overhof, *Influence of stacking disorder on the dc conductivity of layered semiconductors*, Phys. Rev. B, **15**, 2058 (1977).

[16] G. D. Guseinov, G. B. Abdullayev, S. M. Bidzinova, F. M. Seidov, M. Z. Ismailov, and A. M. Pashayev, *On new analogs of TlSe-type semiconductor compounds*, Phys. Lett. A, **33**, 421(1970).

[17] V. Grivickas, V. Bikbajevas, Mi. I. Tarasik, and A.K. Fedotov, *Investigation of structure and carrier recombination in $TlGaSe_2$ layered crystals*, Lithuanian J. Phys., **46**, 67 (2006).

[18] J. A. Kalomiros N. Kalkan, M. Hanias, A.N. Anagnostopoulos, and K. Kambas, *Optical and photoelectric properties of $TlGaSe_2$ layered crystals*, Solid State Commun. **96**, 601 (1995).

[19] B. GÜrbulak, S. Duman, and A. Ateş, *The Urbach tails and optical absorption in layered semiconductor $TlGaSe_2$ and $TlGaS_2$ single crystals*, Czech J. Phys., **55**,93 (2005).

[20] N. M. Gasanly, *Coexistence of Indirect and Direct Optical Transitions, Refractive, Index and Oscillator Parameters in $TlGaS_2$, $TlGaSe_2$, and $TlInS_2$ Layered Single Crystals*, J. Korean Phys. Soc. 57, 164 (2010).

[21] O. Z. Alekperov, *Layered character of dielectric function in $TlGaSe_2$ at phase transition from exciton spectroscopy*, J. Phys. Chem. Solids, **64**, 1707 (2003).

[22] R. M. Sardarly, O. A. Samedov, I. S. Sadykhov, E. I. Mardukhaeva, and T. A. Gabibov, *Ferroelectricity and polytypism in $TlGaSe_2$ Crystals*, Solid State Commun., **77**, 453 (1991).

[23] N. A. Borovoĭ, Y. P. Gololobov, G. L. Isaenko, and N. B. Stepanishchev, *Influence of polytypism on structural phase transformations in $TlGaSe_2$ crystals,* Phys. Solid State, **51**, 2367 (2009).

[24] S. G. Abdullaev A, G. L. Belenkii, M. O. Godzhaev, and N. T. Mamedov, *Excitons in $TlGaSe_2$*, Phys. Status Solidi B, **103**, K61 (1981).

[25] Y. Shim, W. Okada, K. Wakita and N. Mamedov, *Refractive indices of layered semiconductor ferroelectrics $TlInS_2$, $TlGaS_2$, and $TlGaSe_2$ from ellipsometric measurements limited to only layer-plane surfaces*, J. Appl. Phys. **102**, 083537 (2007).

[26] G. D. Guseinov, V. A. Aliev, and E. F. Bagirzade, *Recombination levels in non-stoichiometrie $TlGaSe_2$*, Phys. Status Solidi A, **94**, 653 (1986).

[27] I. M. Ashraf, M. M. Abdel-Rahman, and A. M. Badr, *Photoconductivity of $TlGaSe_2$ layered single crystals*, J. Phys. D: Appl. Phys., **36**, 109 (2002).

[28] N. S. Yuksek, H. Kavas, N. M. Gasanly, and H. Ozkan, *Trapping center parameters of $TlGaSe_2$ layered crystals*, Physica B, **344**, 249 (2004).

[29] N. M. Gasanly, A. Serpengüzel, A. Aydınlı, and S. M. A. Baten, *Low-temperature visible photoluminescence spectra of $TlGaSe_2$ layered crystal*, J. Lumines. **86**, 39 (2000).

[30] F. A. Mikailov, B. Z. Rameev, S. Kazan, F. Yildiz, T. G. Mammadov, and B. Aktas, *EPR spectra of Fe^{3+} centers in layered $TlGaSe_2$ single crystal*, Sol. St. Commun. **133**, 389 (2005).

[31] J. Banys, A. Brilingas, and J. Grigas, *Pinning effect on microwave dielectric properties and soft mode in $TlInS_2$ and $TlGaSe_2$ ferroelectrics*, Phase Trans., **20**, 211 (1990).

[32] M. Acikgoz, S. Kazan, F. A. Mikailov, T. G. Mammadov, and B. Aktaş, *Structural phase transitions in Fe^{3+} -doped ferroelectric $TlGaSe_2$ crystal*, Solid State Commun., **145**, 539 (2008).

[33] F. A. Mikailov, B. Z. Rameev, S. Kazan, F. Yıldız, and B. Aktaş, *Electron paramagnetic resonance investigation of Fe^{3+} doped $TlInS_2$ single crystal*, Sol. St. Commun. **135**, 114 (2005).

[34] N. Z. Gasanov, E. M. Kerimova, A. I. Gasanov, and Y. G. Asadov, *Optical properties and crystal lattice parameters of $TlGa_{1-x}Fe_xSe_2$ solid solutions,* Low Temp. Phys. **33**, 86 (2007).

[35] A. A. Volkov, Y. G. Goncharov, G. V. Kozlov, S. P. Lebedev, A. M. Prokhorov, R. A. Aliev, and K. P. Allahverdiev Sov.—JETP Lett. 37 615 (1983) (Engl. Transl.)

[36] H. D. Hochheimer, E. Gmelin, W. Bauhofer, C. von Schnering-Schwarz, H. G. von Schnering, J. Ihringer, and W. Appel, *Study of the ferroelectric phase transition of $TlGaSe_2$ by dielectric, calorimetric, infrared and X-ray diffraction measurements*, Z. Phys. B – Condens. Mat., **73**, 257 (1988).

[37] K. R. Allakhverdiev, T. G. Mammadov, R. A. Suleymanov, and N. Z. Gasanov, *Deformation effects in electronic spectra of the layered semiconductors $TlGaS_2$, $TlGaSe_2$ and $TlInS_2$*, J. Phys.: Condens. Matter. **15**, 1291 (2003).

[38] K. R. Allakhverdiev, M. A. Aldzanov, T. G. mamedov, and E. Yu. Salaev, *Anomalous behaviour of the Urbach edge and phase transitions in $TlGaSe_2$*, Sol. St. Commun. **58**, 295 (1986).

[39] M. Y. Seyidov, R. A. Suleymanov, E. Yakar, N. A. Abdullayev, and T. G. Mammadov, *Effect of electric field on negative linear expansion of ferroelectric-semiconductor $TlGaSe_2$*, J. Appl. Phys. **106**, 063529 (2009).

[40] V. Aliyev, S. Babayev, T. Mammadov, M.-H. Y. Seyidov, and R. Suleymanov, *Memory effect in ferroelectric-semiconductor with incommensurate phase $TlGaSe_2$*, Solid State Commun., **128**, 25, (2003).

[41] M. Yu. Seyidov, R. A. Suleymanov, and E. Yakar, *Thermal expansion and memory effect in the ferroelectric-semiconductor $TlGaSe_2$,* J. Appl. Phys. **106**, 023532 (2009).

[42] M. Y. Seyidov, R. A. Suleymanov, E. Yakar, Y. Şahin, and M. Açikgöz, *Memory effect and new polarized state in the incommensurate phase of $TlGaSe_2$ ferroelectric – semiconductor*, J. Appl. Phys., **110**, 013529 (2011).

[43] M. Y. Seyidov, R. A. Suleymanov, and Y. Şale, *Unusual Urbach tail in $TlGaSe_2$ ferroelectric-semiconductor with incommensurate phase*, J. Appl. Phys. **112**, 103106 (2012).

[44] G. I. Abutalybov, I. K. I. K. Nejmanzade, B. S. Rasbirin, E. J. Salajev, and A. N. Staruchin, Sov. Phys. Semicond. **20**, 1063 (1986).

[45] A. J. Aoyagi, Y. Maryama, S. Onari, K. R. Allakhverdiev, and E. Bairamova, *Photoluminescence of $TlInS_2$ at Low Temperatures*, Jpn. J. Appl. Phys. **32**, no. S3, 754 (1993).

[46] A. N. Georgobiani and A. M. Evloev, *Photoluminescence spectra of $TlGaSe_2$ semiconductor structures*, Bull. Lebedev Phys. Inst., **36**, 293 (2009).

[47] K. Wakita, A. Suzuki, U. Miyamoto, D. Huseynova, YG. Shim, N. Mamedov, O. Alekperov, A. Najafov, and T. Mammadov, *Confocal laser spectroscopy of $TlInS_2$, $TlGaSe_2$ and $TlGaS_2$ semiconductors-ferroelectrics,* Abstract O2-1, ICTMC-17 (Baku 2010).

[48] http://www.ioffe.ru/SVA/NSM/Semicond/SiC/

[49] A. Belabbes, C. Panse, J. Furthmüller, and F. Bechstedt, *Electronic bands of III-V semiconductor polytypes and their alignment,* Phys. Rev. B, **86**, (2012).

[50] A. Dargys and J. Kundrotas, *Handbook on the physical properties of Ge, Si, GaAs and InP*, (Science and Encyclopedia Publishers, Vilnius, 1994).

[51] S. Kamiyama, T. Maeda, Y. Nakamura, M. Iwaya, H. Amano, I. Akasaki, H. Kinoshita, T. Furusho, M. Yoshimoto, T. Kimoto, J. Suda,

A. Henry, I. G. Ivanov, J. P. Bergman, B. Monemar, T. Onuma, and S. F. Chichibu, *Extremely high quantum efficiency of donor-acceptor-pair emission in N-and-B-doped 6H-SiC,* J. Appl. Phys. **99**, 093108 (2006).

[52] S. Kamiyama, M. Iwaya, T. Takeuchi, I. Akasaki, M. Syväjärvi, and R. Yakimova, *Fluorescent SiC and its application to white light-emitting diodes*, J. Semicond. **32**, 013004 (2011).

[53] S. Kamiyama, M. Iwaya, T. Takeuchi, I. Akasaki, R. Yakimova, and M. Syväjärvi, *White light-emitting diode based on fluorescent SiC*, Thin Solid Films, **522**, 23, (2012).

[54] H. Ou, Y. Ou, A. Argyraki, S. Schimmel, M. Kaiser, P. Wellmann, M. K. Linnarsson, V. Jokubavicius, J. Sun, R. Liljedahl, and M. Syväjärvi, *Advances in wide bandgap SiC for optoelectronics*, Eur. Phys. J. B, **87** (2014).

[55] A. Gali, *Ab initio study of nitrogen and boron substitutional impurities in single-wall SiC nanotubes,* Phys. Rev. B, **73,** 245415 (2006).

[56] A. Gali, T. Hornos, P. Deák, N. T. Son, E. Janzén, and W. J. Choyke, *Activation of shallow boron acceptor in C/B coimplanted silicon carbide: A theoretical study*, Appl. Phys. Lett., **86**, 102108 (2005).

[57] G. Tamulaitis, I. Yilmaz, M. S. Shur, T. Anderson, and R. Gaska, *Carrier lifetime in conductive and vanadium-doped 6H-SiC substrates*, Appl. Phys. Lett., **84**, 335 (2004).

[58] A. Galeckas, J. Linnros, M. Frischholz, and V. Grivickas, *Optical Characterization of Excess Carrier Lifetime and Surface Recombination in 4H/6H-SiC*, Appl. Phys. Lett., **79**, 365 (2001).

[59] H.-S. Lee, M. Domeij, C.-M. Zetterling, M. Östling, F. Allerstam, and E. O. Sveinbjörnsson, *Surface passivation oxide effects on the current gain of 4H-SiC bipolar junction transistors*, Appl. Phys. Lett., **92**, 082113 (2008).

[60] R. Singh, *Reliability and performance limitations in SiC power devices*, Microelectron. Reliab., **46**, 713, (2006).

[61] Y. Zhang, B. Zhang, Z. Li, X. Deng, and X. Liu, *The effect of the surface recombination on current gain for 4H-SiC BJT*, IEEE (EDSSC), 491 (2009).

[62] M. Wolborski, M. Bakowski, A. Ortiz, V. Pore, A. Schöner, M. Ritala, M. Leskelä, and A. Hallén, *Characterisation of the Al_2O_3 films deposited by ultrasonic spray pyrolysis and atomic layer deposition methods for passivation of 4H–SiC devices*, Microelectron. Reliab., **46**, 743 (2006).

[63] A. Schöner, M. Krieger, G. Pensl, M. Abe, and H. Nagasawa, *Fabrication and Characterization of 3C-SiC-Based MOSFETs*, Chem. Vapor. Depos., **12**, 523 (2006).

[64] G. Manolis, *Optical and electrical properties of highly excited 3C-SiC crystals and heterostructures,* Doctoral thesis, Vilnius University, Vilnius, Lithuania (2013).

[65] Y. Sun, S. Izumi, S. Sakai, K. Yagi, and H. Nagasawa, *Saddle-shape warpage of thick 3C-SiC wafer: Effect of nonuniform intrinsic stress and stacking faults*, Phys. Status Solidi B, **249**, 555 (2012).

[66] P. Grivickas, *Optical Studies of Carrier Transport and Fundamental Absorption in 4H-SiC,* Doctoral thesis, Royal Institute of Technology, Stockholm, Sweden (2004).

[67] J. Linnros, *Carrier lifetime measurements using free carrier absorption transients. I. Principle and injection dependence*, J. Appl. Phys., **84**, 275 (1998).

[68] J. Linnros, *Carrier lifetime measurements using free carrier absorption transients. II. Lifetime mapping and effects of surface recombination*, J. Appl. Phys., **84**, 284 (1998).

[69] W. Shockley and W. T. Read, *Statistics of the Recombinations of Holes and Electrons,* Phys. Rev., **87**, 835 (1952).

[70] V. Grivickas, D. Noreika, and J. A. Tellefsen, *Surface and Auger Recombiantions in Silicon Wafers of High Carrier Density,* Lith. J. Phys. **29**, 48 (1989).

[71] J. W. Sun, I. G. Ivanov, R. Liljedahl, R. Yakimova, and M. Syväjärvi, *Considerably long carrier lifetimes in high-quality 3C-SiC(111)*, Appl. Phys. Lett., **100**, 252101 (2012).

[72] T. Kimoto, T. Hiyoshi, T. Hayashi, and J. Suda, *Impacts of recombination at the surface and in the substrate on carrier lifetimes of n-type 4H–SiC epilayers*, J. Appl. Phys., **108**, 083721 (2010).

[73] A. B. Sproul, *Dimensionless Solution Of The Equation Describing The Effect Of Surface Recombination On Carrier Decay In Semiconductors,* J. Appl. Phys., **76**, 2851 (1994).

[74] K. L. Luke and L. J. Cheng, *Analysis of the Interaction of a Laser Pulse With a Silicon Wafer: Determination of Bulk Lifetime and Surface Recombination Velocity*, J. Appl. Phys., **61**, 2282 (1987).

[75] C. Klingshirn, *Semiconductor Optics*, second ed., (Springer-Verlag, Berlin, 2005).

[76] A. R. Goni, A. Cantarero, K. Syassen, and M. Cardona, *High-pressure low-temperature study of the exciton absorption in GaAs*," High Pressure Res., **3**, 81 (1990).

[77] N. C. Fernelius, *Properties of gallium selenide single crystal*, Progr. Crystal Growth and Charact. Mat., **28**, 275 (1994).

[78] D. Thomas, J. Hopfield, and W. Augustyniak, *Kinetics of Radiative Recombination at Randomly Distributed Donors and Acceptors*, Phys. Rev., **140**, A202 (1965).

[79] P. Ruello and V. E. Gusev, *Physical mechanisms of coherent acoustic phonons generation by ultrafast laser action*, Ultrasonics, **56**, 21 (2015).

[80] M. W. Sigrist, *Laser generation of acoustic wave in liquids and gases*, J. Appl. Phys. **60**, R83 (1986).

[81] K. Song, H. Cha, J. Lee, and I. A. Veselovskii, *Application of optical parametric oscillators to photoacoustic studies in semiconductors*, Appl. Phys. B **61**, 547 (1995).

[82] C.A. Tam, *Applications of photoacoustic techniques*, Rev. Mod. Phys., **58**, 381 (1986).

[83] C. Thomsen, H. T. Grahn, H. J. Maris, and J. Tauc, *Surface generation and detection of phonons by picosecond light pulses*, Phys. Rev. B, **34**, 4129 (1986).

[84] E. S. K. Young, A. V. Akimov, R. P. Campion, A. J. Kent, and V. Gusev, *Picosecond strain pulses generated by a supersonically expanding electron-hole plasma in GaAs*, Phys. Rev. B, **86** (2012).

[85] B. Sullivan and A. C. Tam, *Profile of laser‐produced acoustic pulse in a liquid*, J. Acoust. Soc. Am. **75**, 437 (1984).

[86] V. Grivickas and J. Linnros, *Carrier Lifetime: Free Carrier Absorption, Photoconductivity, and Photoluminescence* in *Characterization of Materials* Second Ed. 3 volums, E.N. Kaufmann, ed. **1**, 658-692 (2012).

[87] V. Grivickas, A. Galeckas, P. Grivickas, J. Linnros, and V. Bikbajevas, *Excess Free Carrier Optical Excitation Spectroscopy in Indirect Semiconductors,* Mat. Science (Medžiagotyra), **7**, 203 (2001).

[88] A. Galeckas, J. Linnros, M. Frischholz, K. Rottner, N. Nordell, S. Karlsson, and V. Grivickas, *Investigation of surface recombination and carrier lifetime in 4H/6H-SiC*, Mat. Sci. Eng. B, **61–62**, 239 (1999).

[89] P. Grivickas, J. Linnros, and V. Grivickas, *Carrier Diffusion Characterization in Epitaxial 4H–SiC*, J. Mater. Res. **16,** 524 (2001).

[90] V. Grivickas, *Absorptive Fourier Transient Grating Spectroscopy in Indirect Semiconductors and Quantum Structures*, Mat. Sci. Forum, **297–298**, 287 (1999).

[91] J. Linnros and V. Grivickas, *Carrier-diffusion measurements in silicon with a Fourier-transient-grating method,* Phys. Rev. B, **50**, 16943 (1994).

[92] V. Grivickas, V. Bikbajevas, V. Gavryushin, and J. Linnros, *Strong photoacoustic pulses generated in* $TlGaSe_2$ *layered crystals,* J. Phys.: Conf. Ser. **100**, 042007 (2008).

[93] P. Grivickas, V. Grivickas, and J. Linnros, *Excitonic Absorption above the Mott Transition in Si*, Phys. Rev. Lett., **91**, 246491 (2003).

[94] M. Y. Seyidov, Y. Sahin, M. H. Aslan, and R. A. Suleymanov, *Mechanisms of current flow in p-$TlGaSe_2$ single crystals*, Semicond. Sci. Tech. **21**, 1633 (2006).

[95] A. F. Qasrawi and N. M. Gasanly, *Electrical conductivity and Hall mobility in p-type $TlGaSe_2$ crystals*, Mater. Res. Bull., **39**, 1351 (2004).

[96] A. F. Qasrawi and N. M. Gasanly, *Hall effect, space-charge limited current and photoconductivity measurements on $TlGaSe_2$ layered crystals*, Semicon. Sci. Technol., **19**, 505 (2004).

[97] B. Weinstein, R. Zallen, M. Slade, and A. deLozanne, *Photoelastic trends for amorphous and crystalline solids of differing network dimensionality*, Phys. Rev. B, **24**, 4652 (1981).

[98] F. J. Manjon, Y. van der Vijver, A. Segura, and V. Muñoz, *Pressure dependence of the refractive index in InSe*, Semicond. Sci. Tech., **15**, 806 (2000).

[99] S. Adachi, GaAs and Related Materials (Bulk Semiconductors and Superlattice Properties) (World Scientific, Singapore, 1994).

[100] Yu. V. Ilisavskii, V. M. Sternin, R. A. Suleimanov, F. M. Salaev, and M. Yu. Seidov, Sov. Phys. – Solid State, **33**, 57-60 (1991).

[101] Y. Shim, Y. Nishimoto, W. Okada, K. Wakita, and N. Mamedov, *Temperature-dependent spectro-ellipsometric studies of optical transitions near absorption edge of $TlInS_2$*, Phys. Status Solidi C, **5**, 1121 (2008).

[102] J. I. Pankove, *Optical Processes in Semiconductors,* (Dover Publ., New York, 1971 p 93.

[103] B. Gurbulak, *The Effect of Fe on the Absorption Spectra in $TlGaS_2$, $TlGa_{0.99}Fe_{0.01}S_2$ and $TlGa_{0.98}Fe_{0.02}S_2$ Layer Single Crystals,* Phys. Status Solidi A, **154**, 349 (2001).

[104] F. M. Hashimzade, D. A. Huseinova, G. S. Orudzhev, M. A. Nizametdinova, A. M. Ulubey, and K. R. Allakhverdiev, *Lattice dynamics of layered ferroelectric semiconductor compound $TlGaSe_2$*, Mater. Res. Bull., **45**, 1438(2010).

[105] M. Acikgoz, S. Kazan, F. A. Mikailov, E. Kerimova, and B. Aktas, *Low temperature EPR spectra of* Fe^{3+} *centers in ternary layered* $TlGaS_2$ *crystal*, Cryst. Res. Technol., **43**, 863 (2008).

[106] V. Bikbajevas, V. Grivickas, A. V. Mudryj, A. V. Ivanyukovic, M.I. Odrinskij, M. I. Tarasyk, A. K. Fedotov, and A. M. Janchenko, *Electrophysical properties of* $TlGaSe_2$ *layered crystals, NEET–5,* Zakopane, Poland, June 12-15, p. 62 (2007) (in Russian).

[107] M. Syväjarvi and R. Yakimova, *Sublimation epitaxial growth of hexagonal and cubic SiC,* Comprehensive Semiconductor Science and Technology, ed. by Bhattacharya P, Fornari R and Kamimura H pp. 202–231, 2011.

[108] J. W. Sun, S. Kamiyama, V. Jokubavicius, H. Peyre, R. Yakimova, S. Juillaguet, and M. Syväjärvi, *Fluorescent silicon carbide as an ultraviolet-to-visible light converter by control of donor to acceptor recombinations*, J. Phys. D: Appl. Phys., **45**, 235107 (2012).

[109] P. Ščajev, K. Jarašiūnas, A. Kadys, J. Storasta, P. L. Abramov, S. P. Lebedev, A. A. Lebedev, G. Ferro, and P. Siffert, *Impact of nonintentional Al impurity to carrier lifetime and diffusion in sublimation grown 3C heterostructures*, **1292**, 107 (2010).

[110] M. Ichimura, *Temperature dependence of a slow component of excess carrier decay curves*, Solid-State Electron., **50,** 1761 (2006).

[111] A. A. Lebedev, *Deep level centers in silicon carbide: A review,* Semiconductors, **33**, 107 (1999).

[112] A. V. Duijn-Arnold, T. Ikoma, O. Poluektov, P. Baranov, E. Mokhov, and J. Schmidt, *Electronic structure of the deep boron acceptor in boron-doped 6H-SiC*, Phys. Rev. B, **57**, 1607 (1998).

[113] P. Ščajev, A. Usikov, V. Soukhoveev, R. Aleksiejūnas, and K. Jarašiūnas, *Diffusion-limited nonradiative recombination at extended defects in hydride vapor phase epitaxy GaN layers*, Appl. Phys. Lett. **98**, 202105 (2011).

[114] J. W. Sun, V. Jokubavicius, R. Liljedahl, R. Yakimova, S. Juillaguet, J. Camassel, S. Kamiyama, and M. Syväjärvi, *Room temperature luminescence properties of fluorescent SiC as white light emitting diode medium*, Thin Solid Films, **522,** 33 (2012).

[115] P. Grivickas, A. Galeckas, J. Linnros, M. Syväjärvi, R. Yakimova, V. Grivickas, and J. A. Tellefsen, *Carrier lifetime investigation in 4H–SiC grown by CVD and sublimation epitaxy*, Mater. Sci. Semicond. Process. **4**, 191 (2001).

[116] A. Galeckas, P. Grivickas, V. Grivickas, V. Bikbajevas, and J. Linnros, *Temperature Dependence of the Absorption Coefficient in 4H- and 6H-Silicon Carbide at 355 nm Laser Pumping Wavelength,* Phys. Status Solidi A, **191**, 613 (2002).

[117] V. Grivickas, A. Galeckas, P. Grivickas, and J. Linnros, *Determination of the Polarization Dependence of the Free-Carrier-Absorption in 4H-SiC at High-Level,* Mat. Sci. Forum **338 – 243,** 555 (2000).

[118] A. Galeckas, V. Grivickas, J. Linnros, H. Bleichner, and J. Hallin, *Free Carrier Absorption and Lifetime Mapping in 4H SiC,* J. Appl. Phys. **81,** 3522 (1997).

[119] A. Galeckas, J. Linnros, V. Grivickas, U. Lindefelt, and C. Hallin, *Auger recombination in 4H-SiC: Unusual temperature behavior*, Appl. Phys. Lett., **71**,3269 (1997).

[120] P. B.Klein, R. Myers-Ward, K.K. Lew, B.L. VanMil, C. R. Eddy, D.K. Gaskill, A. Shrivastava, and T.S. Sudarshan, *Recombination Processes Controlling the Carrier Lifetime in n−4H–SiC Epilayers With Low* $Z_{1/2}$ *Concentrations*, J. Appl. Phys., **108**, 033713 (2010).

[121] P. Ščajev, V. Gudelis, K. Jarašiūnas, and P. B. Klein, *Fast and Slow Carrier Recombination Transients in Highly Excited 4H– and 3C–SiC crystals at Room Temperature*, J. Appl. Phys., **108**, 023705(1-9) (2010).

[122] T. Miyazawa, M. Ito, and H. Tsuchida, *Evaluation of Long Carrier Lifetimes in Very Thick 4H-SiC Epilayers*, Mat. Sci. Forum **679–680**, 197 (2011).

[123] T. Yamada and K. M. Itoh, *Optical and Electrical Characterization of Free-Standing 3C-SiC Films Grown on Undulant 6in Si Substrates*, Mat. Sci. Forum, **389–393**, 675 (2002).

[124] H. Philipp, *Intrinsic Optical Absorption in Single-Crystal Silicon Carbide*, Phys. Rev., **111**, 440 (1958).

[125] M.L. Belle, N.K. Prokof'eva and M. B. Reifman Sov. Phys. Semicond. **1**, 315 (1967).

[126] W. J. Choyke, Z. C. Feng, and J. A. Powell, *Low-temperature photoluminescence studies of chemical-vapor-deposition-grown 3C-SiC on Si*, J. Appl. Phys., **64**, 3163 (1988).

[127] A. Solangi and M. I. Chaudhry, *Absorption coefficient of β–SiC grown by chemical vapor deposition*, J. Mater. Res., **7**, 539 (1992).

[128] W. Choyke, D. Hamilton, and L. Patrick, *Optical Properties of Cubic SiC: Luminescence of Nitrogen-Exciton Complexes, and Interband Absorption*, Phys. Rev., **133**, A1163 (1964).

[129] S. G. Bishop and J. A. Freitas, *Photoluminescence characterization of cubic SiC grown by chemical vapor deposition on Si substrates*, J. Cryst. Growth, **106**, 38 (1990).

[130] M. Kato, A. Yoshida, M. Ichimura, and H. Nagasawa, *Excess carrier lifetime and strain distributions in a 3C-SiC wafer grown on an undulant Si substrate*, Phys. Status Solidi A, **210**, 1719 (2013).